TECHNICAL REPORT

SCS Instrument Review Report

September 2022

Robert Carley, Benjamin van Kuiken, Loïc Le Guyader, Giuseppe Mercurio, and Andreas Scherz on behalf of the SCS group at European XFEL

European X-Ray Free-Electron Laser Facility GmbH

Holzkoppel 4

22869 Schenefeld

Germany

Contents

Versions

To make the Instrument Review Report publicly available some unpublished material in the science and capabilities chapter has been removed.

Full Version

Release date: August 2022
Review date: September 2022

Public Version

- chapter 2.1.3 "Spin-crossover complexes and cooperativity" has been removed.
- chapter 2.4.3 "Photochemical dynamics of transition metal complexes in solution probed by time-resolved RIXS" has been removed.

Release date: February 2023

Acknowledgment

1　Introduction

The Spectroscopy and Coherent Scattering (SCS) Instrument provides time-resolved X-ray spectroscopy tools to investigate the electronic structure of complex materials and reveal material dynamics on nanometer length scales using soft x-rays.

The SCS Instrument started user operation in December 2018 with an early user science program in the form of open user community proposals. Initial studies were concerned with the interaction of intense X-ray pulses with matter until the pulse-resolved DSSC detector and an optical laser for time-resolved studies became available in May 2019 that are the primary target of the SCS Instrument (88% of user proposals require an optical laser). During the first three years of operation the focus was on solid state systems, in particular laser-driven electron and spin dynamics of magnetic systems were investigated, providing fundamental insights relevant for future spintronics and magnetic storage applications. With the integration of the Heisenberg Resonant Inelastic X-ray Scattering (hRIXS) spectrometer and additional sample environments during the last year, all contributed by the hRIXS User Consortium (UC), the current emphasis has moved to a broader range of complex materials including molecular systems, and the Instrument has reached the full scientific scope and methodologies as envisioned in the design phase. Nevertheless, the instrumental capabilities will be continuously extended, with a range of additional instrumentation in planning, including a dedicated THz delivery and developments in sample environments and methodologies.

The SCS Instrument has an international user community and includes scientist from diverse areas of ultrafast magnetism, quantum and strongly correlated materials as well as water science and ultrafast chemistry. The basic research performed by users at SCS has led to articles in Nature materials and Science Advances that relates well to nanotechnologies and material applications addressing societal challenges.

The SCS Instrument provides two experiment stations, FFT and XRD, for solid state sample environments, facilitating forward- and back-scattering geometries for thin films, complex samples and single crystals, respectively. A third experiment station, CHEM, was contributed by the hRIXS UC and allows for studying molecular reactions in chemistry and biology, as well as photocatalysis in solution from liquid jets. The main classes of experiments comprise

1　time-resolved X-ray Absorption Spectroscopy (tr-XAS) in transmission geometry

2　time-resolved Small Angle X-ray Scattering (tr-SAXS) from thin films and

nanostructures

3 Coherent Diffraction Imaging and (sub)-microsecond X-ray photon correlation spectroscopy

4 Time-resolved Resonant Inelastic X-ray Scattering (tr-RIXS) from thin films and crystals as well as samples in liquid phase.

5 time-resolved X-ray Diffraction (tr-XRD) of electronic superstructures and lattices in crystals.

The SCS spectroscopy methodologies seamlessly incorporate the FEL operation to optimizing energy and time resolution and performing energy-resolved XAS via undulator gapscan. New concepts based on diffraction optics enable XAS with high signal-to-noise ratios to probe small transient electronic states of matter by XAS with unprecedented sensitivity. So far the XAS studies are not spin-resolved due to the lack of suitable circular polarizers over an extended photon energy range. With the commissioning and operation of the Apple X afterburner in SASE3 in the near future, full polarization control will become available. This will unleash XAS and XMCD studies of complex materials dynamics on femtosecond time scales.

With the recent user-assisted commissioning of the high-resolution RIXS spectrometer, including solid and liquid-jet sample environments at the beginning of 2022, all methods have been successfully realized at the SCS Instrument. The ability to perform high-resolution RIXS at a high-repetition rate XFEL makes the SCS Instrument a world-wide unique place for studying low energy excitations in material science and physics and reaction pathways in chemistry and biology. The first call for RIXS proposals received 29 proposals on top of the ones around the forward-scattering experiment station FFT.

It has been demonstrated that the set of time-resolved X-ray experiments at the SCS Instrument can be scaled from sub-100 kHz to MHz repetition rates depending on the sample delivery and pulse energy of the optical laser at a given wavelength, benefitting of the high repetition rate of the European XFEL.

This document reports on the scientific outcome from the first three years of operation. To provide the full scope of instrumentation capabilities, it further includes recent preliminary results from the user-assisted commissioning of the RIXS spectrometer and CHEM station. In terms of instrument operation, beam stability, special operation modes, the use of detectors, and on- and offline data analysis are further described. Supported by the in-house R&D programs further short and mid-term instrumentation upgrades are listed at the end of this report. These include tunable THz sources, novel timing diagnostics, as well as new x-ray methodologies and experiment station upgrades.

hRIXS user consortium

The Heisenberg-RIXS user consortium was formed to realize a unique scientific opportunity in combining RIXS and the high repetition rate of European XFEL. The scientific aim is to enable, within the fundamental limits of the temporal and energy resolutions, the study of low energy excitations in strongly correlated systems out of equilibrium, the exploration of phase transitions and transient phases as well as revealing energy landscapes and pathways in chemical dynamics of molecules.

The hRIXS project received funding through the Helmholtz Association as part of "Helmholtz International users consortia" and co-funding by the ERC-Advanced Grant "Excited state Dynamics with Anti-Stokes X-ray Raman scattering (EDAX)" at Potsdam University. The detector development was ensured by The Finnish Academy of Science in a FIRI Grant. Personnel for the optical design of the hRIXS spectrometer at Politecnico Milano was contributed within the POLARIXS grant of the PIK initiative by the Italian Ministry of University and Research (MIUR).

A working group was formed in 2014 between the partners of DESY, Potsdam University, Politecnico Milano and European XFEL which lead to the design of the hRIXS spectrometer, and two sample environments for liquid phases and solids, where the solid state sample environment (XRD experiment stations) is contributed by the SCS Instrument of European XFEL.

With the first user operation during the writing of this report, the SCS Instrument has successfully reached its full scientific and instrumental scope, including new scientific user communities.

Charge to the Committee

The six currently operating instruments were opened to user operation between summer 2017 and summer 2019, and will be reviewed in the period March 2022 – September 2023. All six instruments are teeming with scientific ambition. Each was planned to fulfil a variety of scientific needs and experimental requirements for a broad number of user communities, due to the global constraint of only having six instruments at the startup phase of the facility. The present instruments were intended to explore a large and diverse space of scientific areas that, by necessity, led to complex and demanding setups to make effective use of beamtime. The experience of about four years of operation shows that we are now ready to define more specialized setups and instruments that would allow for efficient studies in specific scientific and application areas.

The main goals of the Instrument Reviews are:

1 Assess past performance of the instrument. Receive constructive feedback from
   a leaders in XFEL science and instrumentation to keep the instruments at a world-leading level
   b the science community - even beyond XFEL science – to provide broader perspectives.
2 Receive advice on important future science directions. Your recommendation will be precious aid in steering the scientific vision of the instrument for the next decade, and will contribute to develop a foundation (and justification) for the strategic elements under consideration for the facility.

Your report shall detail responses to the questions below and, in addition, must include a summary of recommendations.

- Please summarize your recommendations in up to 10 short statements.
- Please include specific recommendations given the perspective of future facility development plans.

1 Research by Users and by Staff
   - Which experiments/results would you rank to be outstanding?
   - How do you judge the quality of the major part of the experiments done?
   - Has the suite of experiments performed to date efficiently exploited the unique capabilities of this EuXFEL instrument?
   - Does the instrument cover the most outstanding scientific topics in the respective area of soft X-ray FEL science?

- Should we concentrate activities and resources on specific scientific fields (differently to the present distribution of experiments)? If so, which?
- Are there potential users or communities which have not yet been active?

2 Future scientific directions

- Do the short- and long-term research directions of the instrument address the key needs of users and the broader community?
- Are there outstanding areas that may require more emphasis or effort?

3 Technical status of the Instrument

- Could you evaluate the technical status of the instrument?
- How do you judge technical developments initiated by the Staff? Where do you see needs for improvement or additional development?
- Do you see areas where more effort or even further development by Expert (e.g. laser, optics, detectors, data, sample environment) groups is needed to improve quality, efficiency or productivity?
- Please provide your evaluation of the instrument in the context of (international) competitors, both in terms of scope and performance.

4 Future technical developments

- Where do you see long term needs for technical/capability developments?
- Would you recommend major refurbishment? If so, on which time scale?
- Are there areas where you would recommend a more detailed evaluation by experts in instrumentation?
- Do you see potential for development of common proposals with other X-ray facilities and/or different investigation techniques (n, e, otherwise)?

2 Science and capability highlights

The SCS Instrument was designed to flexibly accommodate a wide range of techniques in the soft- to tender X-ray range aimed at condensed matter samples. Elastic interactions include X-ray absorption spectroscopy (XAS), small-angle X-ray scattering (SAXS) and X-ray diffraction (XRD), and coherent diffractive imaging (CDI). Inelastic scattering can be utilized by the resonant inelastic X-ray scattering (RIXS) spectrometer. These approaches are all augmented by their non-linear counterparts, making use of the high pulse energy of the EuXFEL, and advanced techniques, such as two-colour X-ray delivery and sub-femtosecond X-ray pulse.

This section highlights results from User- and in-house experiments to demonstrate the broad capabilities of the SCS Instrument, and outlines some future directions.

2.1 Femtosecond X-ray Absorption Spectroscopy

X-ray Absorption Spectroscopy is one of the most widely used techniques at synchrotrons around the world to study the local structure and oxidation states of atoms in solids and molecules, on surfaces or in liquids.[3] Its implementation at FELs opens the possibility of performing high-resolution spectroscopy like at synchrotron but on the femtosecond timescale, to monitor for example out-of-equilibrium changes during an ultrafast phase transition or the emergence of hidden metastable phase of matter that are otherwise inaccessible.

One of the main challenges in measuring femtosecond XAS in the soft X-ray regime is the sensitivity required to observe changes in the spectra which are usually small while using monochromatized SASE pulses with very high shot-to-shot intensity fluctuations. For this, two different setups have been implemented and commissioned at SCS. One is based on the Transmission Intensity Monitor (TIM) in combination with the SCS XGM, and was used for one User Experiment (UP2384 Thielmann). The particularity of the TIM setup is that XAS can be recorded in parallel to scattering, which means that, in practice, all scattering experiments also make use of the TIM setup to record the sample XAS. The second setup is based on a beam splitting off axis zone plate (BOZ) and was used so far for 10 User experiments (UP2170 Beye, UP2161 and UP2589 Eschenlhor, UP2712 Scherz, UP2619 Le Guyader, UP2780 Ovchinikov, UP2497 (and continuation UP3216) Cho, UP2609 Menushenkov, UP2784

Van Kuiken and UP2783 Wende). With one exception, all these experiments have been successful and should lead to publications.

The SCS Instrument was conceived at an early stage to implement femtosecond XAS. For this reason, an X-ray Gas Monitor (XGM) [46; 69; 28] was fitted in the the SCS hutch, to record the incoming monochromatic X-ray intensity, so called Io. In addition, a Transmission Intensity Monitor (TIM) is placed at the end of the experimental hutch to record the transmitted intensity in such a way that it can be used with any end-station to investigate widely different sample systems. The TIM is composed of an insertable YAG or CVD screen, from which the fluorescence is collected with multiple micro-channel plates (MCP) and the signal traces are recorded with fast digitizers. With this scheme, a signal over noise ratio (SNR) of about 20 can be achieved with 20 nJ per pulse of X-rays. One key advantage offered by the TIM setup is the possibility to collect XAS in parallel with scattering collected with the DSSC detector.

2.1.1   Ultrafast control of magneto-crystalline anisotropy

This TIM setup was used, for example, to study the transient XAS of $4f$ orbitals in rare earths [73] as shown in Fig. 2.1a). In rare earth, the magnetic moment is mostly carried by the localized $4f$ shell. This localization has two immediate consequences. Firstly, the magnetic order is established indirectly by Ruderman-Kittel-Kasuya-Yosida (RKKY) exchange via $5d$ and $6s$ electrons and secondly, large orbital moments are possible in addition to spin moments. This leads to high magneto-crystalline anisotropy (MCA) which is at the heart of strong permanent magnet.[36] Can we control the exchange interaction or MCA in rare-earth via femtosecond optical excitation of the conduction electron ? In Fig. 2.1b), the excited and unexcited XAS for metallic Tb at the M_5 edge probing the $4f$ shell are shown. The few percent transient changes shown in Fig. 2.1c) is clearly resolved and above the noise level of the experiments offered by the setup. Surprisingly, this transient change cannot be described by considering changes within the $4f$ multiplet alone but requires inclusion of changes in the $4f$ occupation number such as $4f^7$ and $4f^9$ states. Associated with these $4f$ states are very different contribution to the MCA which opens the possibility to control it on the ultrafast time scale as shown in Fig. 2.1d). This change in $4f$ occupation number is rather surprising as it requires energies of 2–3 eV, which in thermal equilibrium would destroy the sample. On ultrafast time scale when the system is brought far out of equilibrium, the situation changes and Thielemann-Kühn & al. results show that a significant $5d - 4f$ electron transfer occur, paving the way for novel device applications employing this ultrafast control of the MCA.
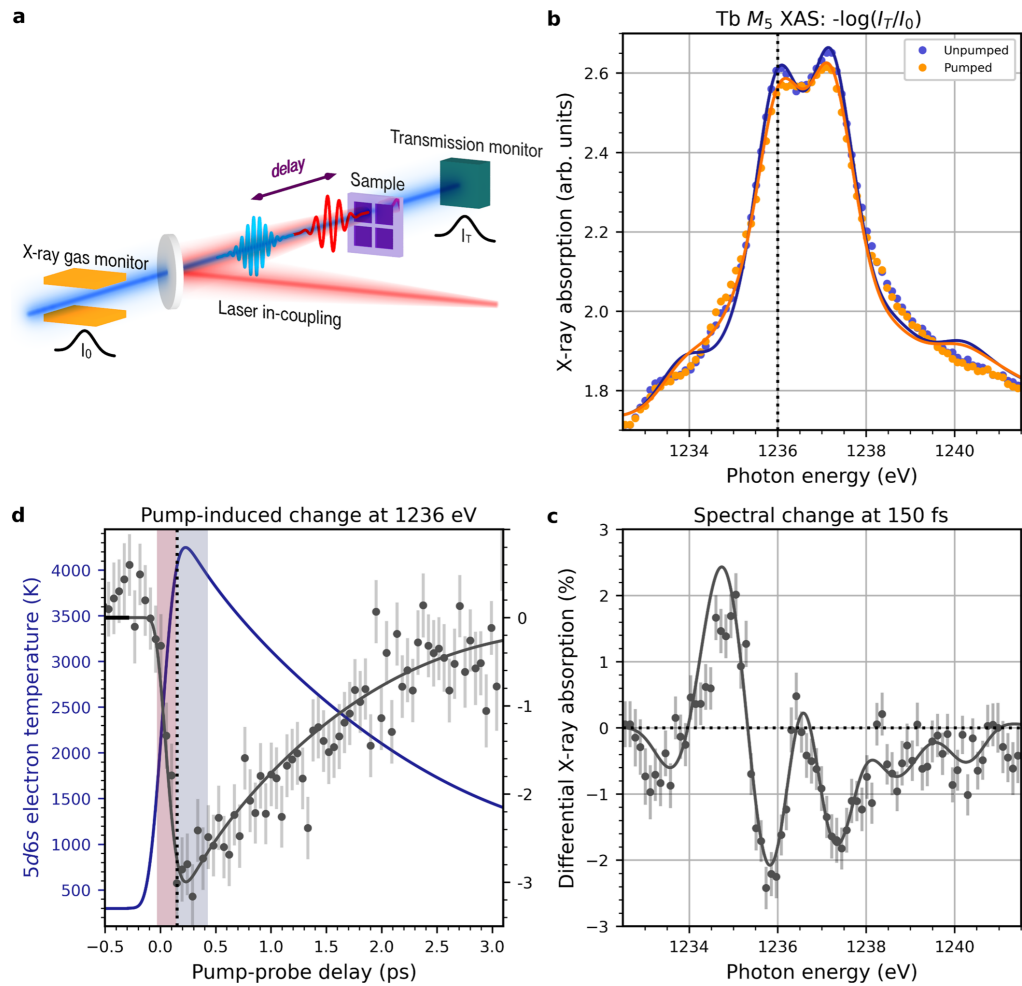
Figure 2.1: Pump-induced changes in the Tb M$_5$ multiplet. a) Sketch of the X-ray absorption experiment. Following excitation with 1.55 eV photons transient X-ray absorption –log(I$_T$/I$_0$) is probed at the Tb M$_5$ edge in transmission geometry with 350 meV energy and 65 fs time resolution. The X-ray gas monitor is used to measure the incident intensity I$_0$, the transmission intensity monitor to determine the sample transmission I$_T$. b) XA spectrum of the Tb $3d_{5/2}$ to $4f$ transition (M$_5$ edge) 150 fs after optical excitation (orange dots) in comparison to the XA spectrum for the unpumped sample (blue dots). c) Differential X-ray absorption. i.e. the relative change of the XA signal between pumped and unpumped sample. Solid lines in b) and c) are fits to the data based on calculations of XA spectra of the $^7F_6$ ground-state (blue), with admixtures of $4f^7$ (3 % $^8S_{7/2}$), $4f^8$ (20 % $^7F_5$) and $4f^9$ (4 % $^6H_{15/2}$) excited state multiplets (orange) and their difference (black). d) Differential XA signal (black data points) as a function of pump-probe delay measured at a photon energy of 1236 eV. The black solid line is an estimate of the transient XA signal based on the Fermi distribution $f(T_e)$ of excited electrons. The electron temperature T_e (blue solid line) has been calculated by the two-temperature model. Adapted from [73]

2.1.2 Beam splitting off axis zone plate setup
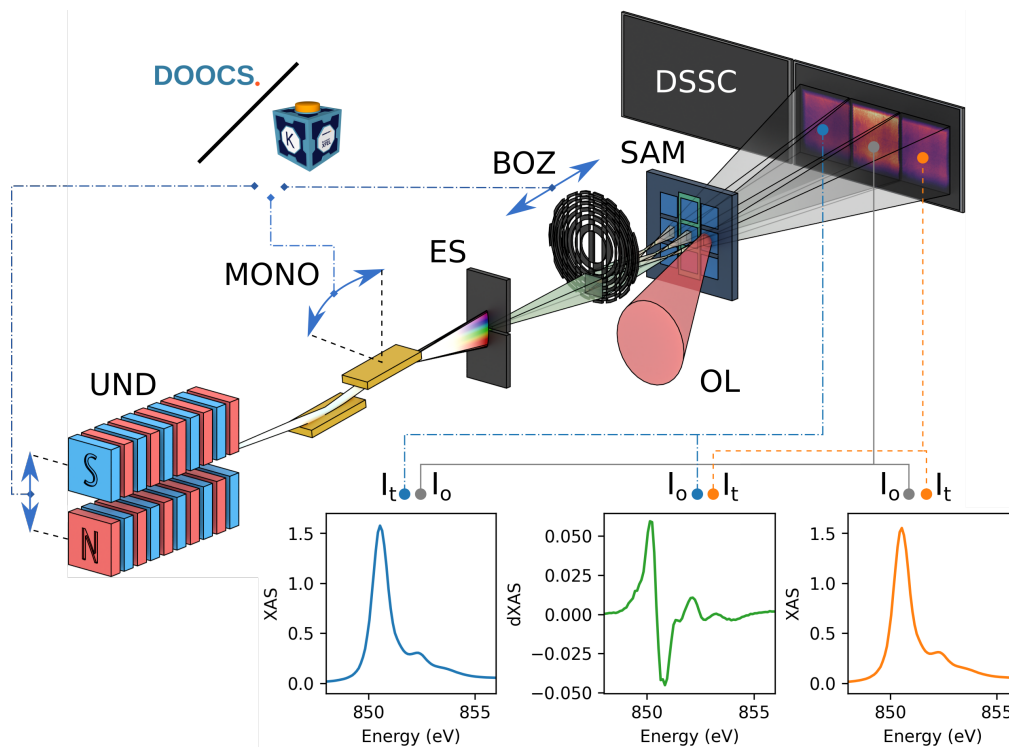
Figure 2.2: SASE FEL pulses are produce in the SASE3 undulators (UND). A variable line spacing plane grating (MONO) is placed 130 m downstream and disperses the SASE pulses on the exit slit (ES) placed 100 m further downstream. The monochromatic x-rays then propagate 30 m further and are split in three beams of equal intensity and focused down in front of the sample by a beam splitting off-axis zone plate (BOZ). The sample (SAM) consists of three X-ray transparent membranes that are aligned on these 3 beams. The X-ray spot size on the membrane is typically 50 um. The middle membrane is usually used as a reference and is either a clear aperture or bare membrane while the other membrane contains the film of interest, here a NiO film. The 3 beams further propagates and expand onto one module of the DSSC detector placed 5.4m downstream. The resulting XAS spectra at the Ni L_3 and L_2 edges are shown for the unexcited sample the excited sample as well as the change in XAS between excited and unexcited sample. During an energy scan, the DOOCS and Karabo control systems ensure that the gap size of the 120 m long undulator follows the monochromator photon energy. Similarly, the zone plate position is adjusted by typically few millimeters to keep the zone plate focus fixed in space. Adapted from [29].

Few nJ of monochromatic soft X-rays per pulse are easily delivered by FELs and contains few 10^7 photons. In the photon shot noise limit, a single shot signal over noise ratio (SNR) in the few thousands is thus in principle achievable which would far exceed the sensitivity offered by the XGM and TIM scheme at SCS. In addition, a better use of every photon in the beam also comes with the added benefit of a better

use of radiation sensitive sample such as photosensitive molecules.

For these purposes, we adapted a scheme that was used at LCLS and reached the photon shot noise limit.[62] Essentially, the idea is to use a low noise CCD detector to measure both the incoming intensity and the transmitted intensity directly. This is achieved by using a diffractive optics to create copies of the incoming beam, with the sample placed in one of these copies. In the improved implementation used at the SCS Instrument and shown in Fig. 2.2, a transmission grating produces three beams of equal intensity (0th, +1st and -1st diffraction order). The grating structure is combined with an off-axis zone plate structure to focused these three beams down and separate them spatially from the other zone plate diffraction order. These beams propagate further downstream and expand in large area onto a single continuous sensor of the DSSC detector in three well separated region of interest. The high sensitivity of this measurement scheme is assured by having a low noise CCD detector and illuminating many pixels to achieve high signal over noise ratio. The method sensitivity is then mainly limited by the number of photons detected. Two identical samples and a reference substrate are placed in each of these beam slightly after the zone plate focus as shown in Fig. 2.2. Different spectra can then be directly computed from the intensity measurement of these three beams. Comparing the unpumped sample and reference beam gives the unpumped XAS spectra that would be measured at synchrotron. From the pumped sample and reference beam, the excited sample XAS can be measured. Finally, from the pumped and unpumped beam, the XAS change itself can be recorded directly.

To record a XAS spectrum, the monochromator is scanned continuously back and forth between two energy end point with the help of a middle layer device developed by the control group and X-ray optics group. The undulator set energy follows the monochromator readback energy with a proportional–integral–derivative loop and communication system developed by control, X-ray optics group and undulator group. To demonstrate the capabilities of this scheme, two community proposals were dedicated for its commissioning. The first one, and also the very first experiment conducted at SCS, was lead by Martin Beye to study non-linear XAS by taking advantage of another feature of the scheme which is the the high X-ray fluence that can be reached with the sample placed at the zone plate focus while all other parts of the setup stay well in the linear regime with large beams and low X-ray intensity.

The second community proposal, lead by Andrea Eschenlohr, performed first pump-probe XAS experiments with the PP laser in Ni and NiO samples. In Fig. 2.2 the NiO XAS and transient XAS spectra around the Ni L_3 edge are shown.

The use of the DSSC detector allows recording up to 800 shots per trains but so far in

experiment on solid system it is limited to 20 X-ray pulses per train due to the limited heat dissipation in solid samples that have been investigated so far at SCS. The sensitivity of the scheme allows single shot measurement at 10 Hz thanks to the Fast Sample Scanner System developed by Carsten Deiter (SE). A formal contract was established with the help of the EuXFEL administration between the European XFEL and the Paul Scherrer Institute with the group of Christian David for the production of diffractive optics which makes this scheme available to all SCS users.

To reach the shot noise limit, certain data correction steps are necessary and significant efforts have been devoted to work them out.[29] The first correction is a flat field normalization that compensate inhomogeneous diffraction efficiency in the fabricated diffractive optics. This is determined by recording data without any sample in the beam and ensures that the measured sample transmission is unity in this case. The second correction is a single non-linear correction function that is applied to every pixels of the DSSC and ensures that the measure transmission is independent of the measured Io. The determination of these 2 corrections has been implemented in a python code and corresponding jupyter notebooks made available to the Users. Moreover, the online analysis tools used during User beamtime implement as well both corrections to give the Users the best live view possible of their data as they are recorded.

2.2   Small-Angle X-ray Scattering: Ultrafast magnetization dynamics on the nanoscale

Small angle x-ray scattering (SAXS), whereby x-rays impinging on a sample elastically exchange momentum with the sample and are deflected from their original trajectory by a small angle, derives from the charge and magnetic inhomogeneity of the sample. In magnetic materials this inhomogeneity often takes the form of regular domain patterns, and at resonance the SAXS intensity can be used to monitor the magnetic state, such as the formation or loss of magnetic order.

A total of 8 User experiments and one in-house beam time have exploited femtosecond time-resolved SAXS. The first SAXS experiment, UP2197 (Pfau), was an open community (i.e. commissioning) proposal looking at x-ray induced transparency using the fastCCD detector, which was then replaced by the significantly better DSSC. UP2212 (Jal) was a open community proposal to investigate multi-pulse, helicity dependent switching in CoTb thin films. UP2225 (Carley) and UP2565 (Scherz) studied the laser-driven AFM-to-FM phase transition of FeRh, the latter combined with TR-XAS. Results from these two experiments formed the backbone of the PhD thesis of Naman Agarwal [1]. UP2313 (Pronin) studied the magnetisation dynamics of ultrathin Co films. UP2280 (Dürr) was concerned with the coupling between nano-magnetic, charge and lattice degrees of freedom in FePt nanoparticles. Büttner et al. (UP2252) used SAXS to investigate laser-driven skyrmion formation, as described in more detail below. Also described further below, Turenne et al. [74] (UP2599) made use of the sensitivity of non-resonant SAXS to the charge scattering to identify spin soliton dynamics in FePt nanoparticles. Silva (UP2719) used SAXS to investigate the role of the ground state magnetic domain pattern on the magnetization dynamics in CoFe/Ni mulitlayer samples. Most recently, Philippi-Kobs and coworkers (UP2800) examined the magnetization dynamics of DyCO films at low temperatures.

2.2.1   Picosecond nucleation of magnetic skyrmions mediated by a fluctuation phase

Phase transitions of topological states are largely unexplored and driving these transitions at fast time scales is particularly challenging because it requires massive reorientation of charge and spin degrees of freedom. An experiment led by Büttner, Pfau and coworkers at SCS (UP2252) discovered that a topological phase, consisting of many magnetic skyrmions, nucleates in less than 300 ps and is mediated by a transient topological fluctuation state [10]. These results are in excellent agreement with atomistic spin dynamics simulations, which leads to a detailed microscopic understanding of all-optical topological switching.

Preliminary synchrotron-based X-ray holography experiments on multilayers of Pt/CoFeB/MgO identified uniform domain states at saturation or stripe domains below saturation (Fig. 2.3a). It was found that, in presence of an external out-of-plane magnetic field and above a certain fluence threshold, a single infrared laser pulse led to the appearance of the skyrmionic phase. The dynamics of skyrmion nucleation was studied by pulse-resolved small-angle X-ray scattering (SAXS) at the European XFEL. Each FEL train consisted of three pulses (60 µs apart from each other), as shown in Fig. 2.3b. The first pulse probed the initial uniform magnetic state (Fig. 2.3c), generated by applying a saturation magnetic field. The second pulse probed the nucleation dynamics triggered by a infrared laser pulse impinging on the sample at a fixed delay before the FEL pulse (Fig. 2.3d). Finally, the third pulse probed the final state, consisting of many magnetic skyrmions (Fig. 2.3e). The cycle field saturation - pump - probe was then repeated at different pump-probe delays.

A quantitative analysis of X-ray scattering data revealed that 300 ps after the laser pulse the integrated intensity reached 80% of the final state intensity. In addition, from the scattering peak position and the decay at its high q shoulder, the correlation length and an estimate of the nuclei size was extracted as a function of the pump-probe delay. Atomistic simulations show an initially diffuse scattering distribution which becomes more intense and concentrated at low q as time
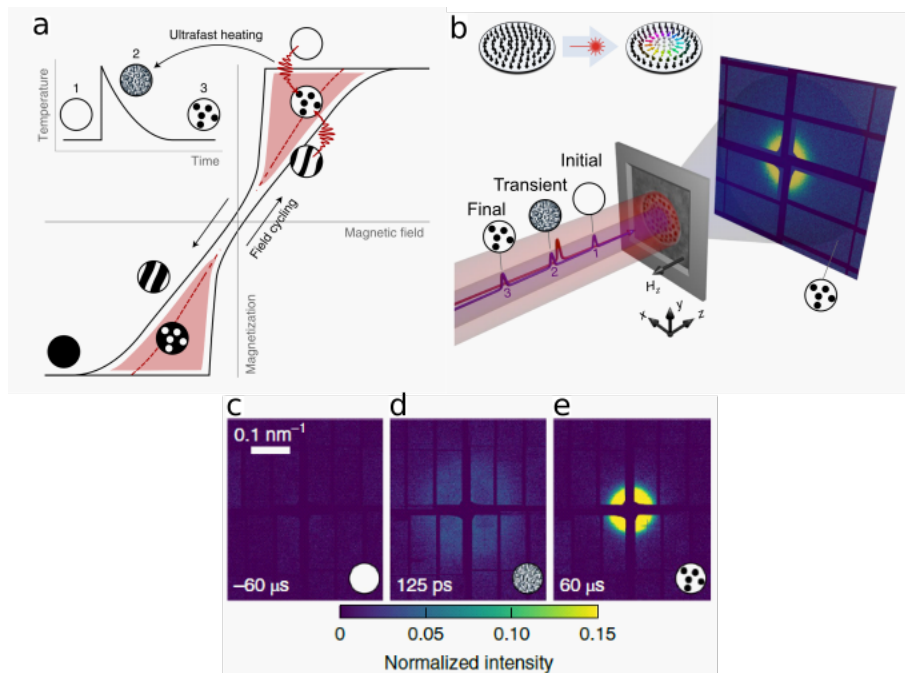

Figure 2.3: a: schematic phase diagram based on X-ray holography results as a function of applied external magnetic field. b: sketch of experimental setup and skyrmion nucleation. Exemplary images of initial (c), transient (d) and final (e) state.

progresses, in excellent agreement with experimental data. In order to achieve the final skyrmionic phase, two conditions are required. First, the topological fluctuation phase should support short-range spin order, as demonstrated by the diffuse scattering. Second, a magnetic field leads to one preferred skyrmion polarity over the other, as demonstrated by the lack of skyrmion nucleation in absence of magnetic field. A deeper insight in the dynamics of skyrmion nucleation is an important step to understand ultrafast topological phenomena and may ultimately disclose the fundamental speed limit of topological phase transitions.

2.2.2 Studying Spin-lattice coupling dynamics in magnetic materials driven by femtosecond laser pulses with tender X-rays

Turenne and co-workers [74] (UP2599) used SAXS to monitor spin wave dynamics following laser excitation of FePt nanoparticles. Example shows the potential of the SCS Instrument in the so-called tender X-ray region between ?? keV and 3 keV.

The FePt nanoparticles form flat cylinders of around 8 nm height and 16 nm diamter, and are embedded in a matrix of amorphous carbon. Their extremely high magnetocrystalline anisotropy has made them the standard for magnetic storage media. For the current study, the commensurately short exchange length allows magnetic structures (i.e. domains, solitons, skyrmions, and so on) to exist within the nanoparticles, which would otherwise be too small.

The experiment was conducted using a monochromatic X-ray beam at 2500 eV combined with the FFT endstation and DSSC detector, as shown schematically in Figure 2.4A. An 800 nm, 50 fs optical laser pulse focused to 50 mJ cm^{-2} quenched the out of plane magnetization of the nanoparticles, initiating a rich phonon and spin wave dynamics.

Heat accumulation in the sample meant that the experiment was performed with a single optical laser pump pulse per 10 Hz train. The X-ray pulse pattern was more complex, with one pulse 70 µs before laser excitation to probe the ground state of the system, followed by the pump-probe pulses. This scheme allowed superior normalization and confirmed that the sample had returned to its initial state during each 10 Hz burst. While this might appear to be along way from using the high repetition rate of the EuXFEL, in fact the ability to measure the sample before and after laser excitation *within the same burst* made measurable the small variations in scattering intensity seen in this study.
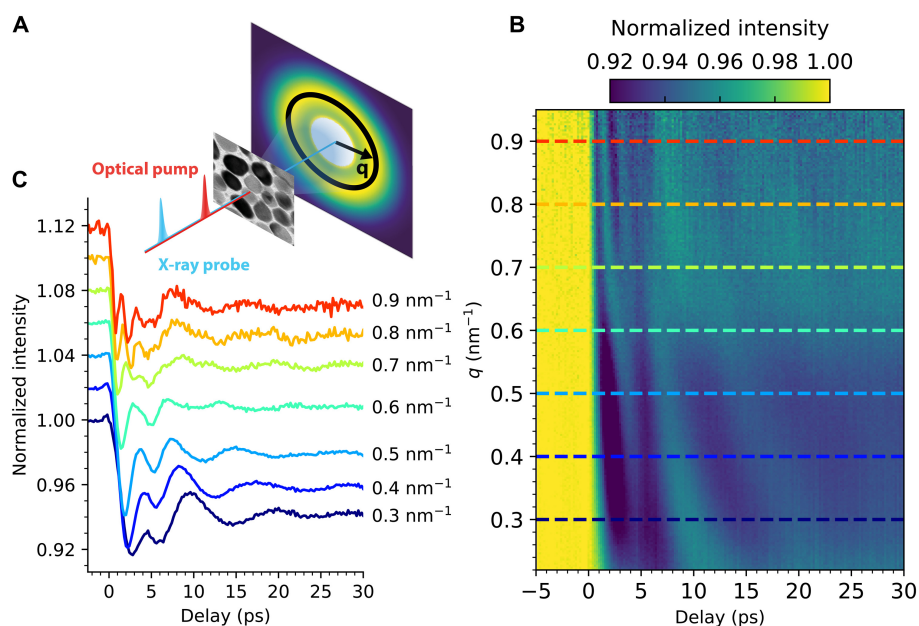
Figure 2.4: Non-resonant time-resolved SAXS of FePt nanoparticles measured at 2500 eV. **A** shows the experiment, scattered data and azimuthal integration. **B** shows the scattered intensity as a function of time and transferred momentum, q. **C** shows lineouts from **B** of scattering intensity dynamics at fixed q, as marked by the dashed horizontal lines in **A**.

Raw DSSC images were binned for time delay and normalized for X-ray intensity for a given pump fluence. Figure 2.4B shows a map of the scattered intensity as a function of time and transferred momentum, q, following azimuthal integration.

The resulting non-resonant SAXS signal is sensitive only to variation of the charge scattering and thus measures the phonon dynamics of the system. These reflect also the spin wave dynamics due to the strong magneto-elastic coupling of FePt. This connection allowed the authors, in combination with micromagnetics simulations, to identify the self assembly and evolution spin wave solitons in the FePt nanaoparticles triggered by the magnetic quench of the pump laser pulse. The soliton is pinned to the outer edge of the nanopartical and exhibits two oscillatory modes. Precession of the in-plane moments of the domain wall between spin up and spin down regions has a characteristic frequecny of 50 GHz. Breathing of the domain wall occurs at 100 GHz and has a low-frequency component at 20 GHz arising from coupling to the in-plane precession.

2.3   X-ray holography at megahertz rates

The intra-train megahertz repetition rate of European XFEL provides unique opportunities for coherent diffraction imaging to greatly enhance the photon statistics and attainable spatial resolution within a typical experiment time but also reveals challenges with fixed solid targets. Hence high-repetition X-ray FELs promise to record movies of magnetization dynamics on nanometer length scales on much faster time scales than possible in corresponding experiments at synchrotrons. This potentially allows for studying laser-driven magnetization reversal, skyrmion nucleation or magnetic soliton dynamics as shown in the previous sections in more detail beyond atomistic magnetization simulations.

While in serial femtosecond X-ray crystallography many copies of the samples can be injected into the beam at megahertz repetition rates, it remains a challenge to recover or to replenish a solid sample between x-ray pulses. To address the feasibility of coherent diffraction imaging (CDI) at high repetition rates, user community proposals in the early phase of the SCS Instrument operation have been carried out exploiting X-ray holographic imaging based on the so-called HERALDO technique [80]. The detailed results have been summarized in a preprint (accepted for publication while this report was written) [31] including the detector calibration and data processing of the high-repetition rate DSSC detector, as well as the discussion of beam parameters and repetition rate to carry out time-resolved holographic imaging of magnetic nanostructures in the most optimum way. A static reconstruction of a magnetic domain pattern is given in Figure 2.5.
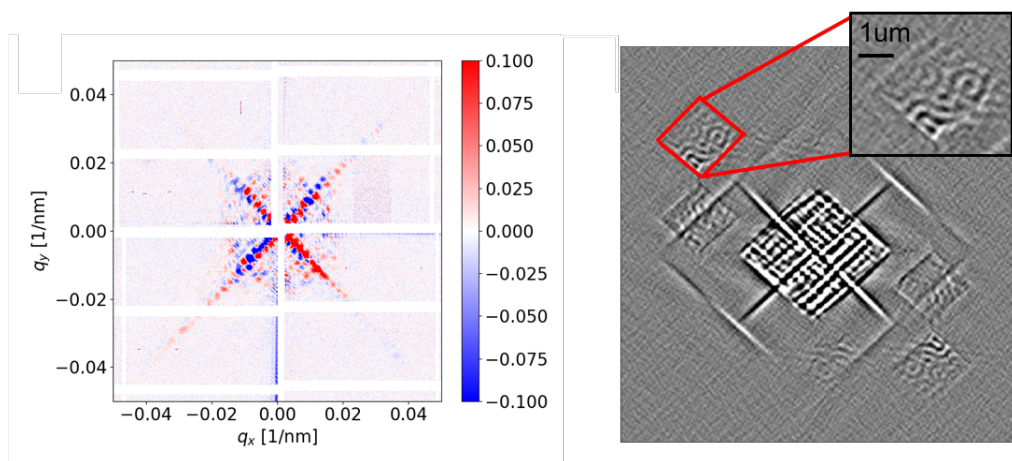
Figure 2.5: (left) X-ray hologram of a magnetic CoFeB thin film multilayer recorded at the Fe L3 edge with an intra-train repetition rate of 2.25 MHz. The intensity is given in linear scale. (right) Reconstruction of the magnetic domain state using the HERALDO method

Time-resolved holographic imaging of magnetic nanostructures still faces a number of challenges. These can be related to beam quality of the incident x-ray beam and the detection of the diffracted X-ray beam. To achieve magnetic contrast in CDI, the holographic mask is illuminated with circular polarized X-rays leading to magnetic scattering between differently-oriented magnetic structures in the sample via X-ray Magnetic Circular Dichroism (XMCD). Currently SASE3 only offers linear horizontal polarization until the Apple X afterburner will be commissioned in the near term. A stand-in solution is the use of magnetic thin film polarizers (containing 3d magnets Fe, Co and Ni) upstream of the experiments, generating up to 40-50 % circular polarized x-ray in vicinity of the absorption edge at the expense of X-ray transmission which is of the order of a few percent. This needs compensation by tighter focusing on the sample of the size of the holographic mask leading to wavefront curvatures and heterogeneous illuminations while at the same time the magnetic contrast is lowered. Performing CDI at MHz repetition rates requires countermeasures to the high thermal load on the upstream beam optics to maintain beam stability and pointing downstream on the sample. The use of the intermediate horizontal focus to generate a new stable source point upstream was imperative for conserving speckle contrast in the accumulated hologram and for successful image reconstructions.

The attainable resolution of CDI is limited by the current version of the DSSC detector, see Section 3.5.1 on page 62 which does not have single-photon sensitivity below 1 keV. The use of the HERALDO holographic technique is particular suited to mitigate distortions from the missing hologram information in the vertical and horizontal gaps of the DSSC detector due to the high-pass filter property of the applied linear differential operators in the image reconstruction [31]. Finally, the conversion of the hexagonal pixel lattice to Cartesian coordinates requires data interpolation to form a full size diffraction pattern before the image reconstruction. This requires high quality conversion filters to reduce the additional and systematic noise sources in the image reconstructions, see Section 3.5.1 on page 62.

2.4 Time-resolved RIXS spectroscopy

Resonant inelastic X-ray scattering (RIXS) is a photon-in photon-out spectroscopy that probes the low-lying excitations in material systems. RIXS can be used to measure vibrational, spin and electronic excitations with site-selectivity. With the goal of developing a dedicated instrument for pump-probe RIXS spectroscopy, the Heisenberg RIXS (hRIXS) spectrometer has been developed collaboratively between XFEL and the hRIXS user consortium.The design of the spectrometer takes into account the tradeoff between time and energy resolution dictated by the uncertainty principle. The goal of the hRIXS spectrometer is to provide a flexible system that can operate either at the highest energy resolution that is provided by the high-resolution SASE3 monochromator grating (HRG) or the high time resolution given by the high-throughput (low-resolution) monochromator grating. X-ray commissioning of the spectrometer began in Spring of 2021, and the first time-resolved RIXS experiments were performed during a set of user-assisted commissioning (UAC) experiments carried out in February and March of 2022. The UAC program focused on the implementation of the pump-probe scheme on solids (UP2769), the commissioning of the liquid jet system (UP2776), and the realization of optical pump-RIXS probe experiments on solution samples (UP2866).

2.4.1 RIXS studies of correlated materials

In UP2769, the laser-induced dynamics in correlated materials were investigated. For these measurements, the HRG was used in both the spectrometer and monochromator was used to resolve spin excitations in the samples. As benchmark for the HRG performance we show in Figure 2.6 two Cu L_3 RIXS spectra of a ~48 nm thick La_2CuO_4 film grown on $LaSrAlO_4$. The measured combined resolution of 93 meV FWHM was obtained with ~8 μm × 200 μm focus on the sample. The sample was at room temperature, with an intra-train repetition rate of 113 kHz and an attenuation x-ray beam of 30% of the maximum flux. In these conditions the sample did not show evident alteration due to radiation damage, as it could be judged from the RIXS spectral shape. The count rate is comparable to that of equivalent spectra measured at synchrotron beamlines [9; 7]. The repetition rate is compatible with ~100 kHz pump laser repetition rate, and can be increased by a factor of 10. The limiting factor would be the pump laser repetition rate and the sample damaging when increasing the average power irradiated through both the xFEL and the pump laser. The two spectra correspond to two scattering geometries, with the same scattering angle $2\theta = 125°$ and horizontal linear polarization of the XFEL beam, i.e, lying in the scattering plane (π polarization). For $\theta \simeq 74°$, the *dd* excitation peaks are more intense and the spin excitations have single magnon and bi-magnon contributions at comparable intensity.
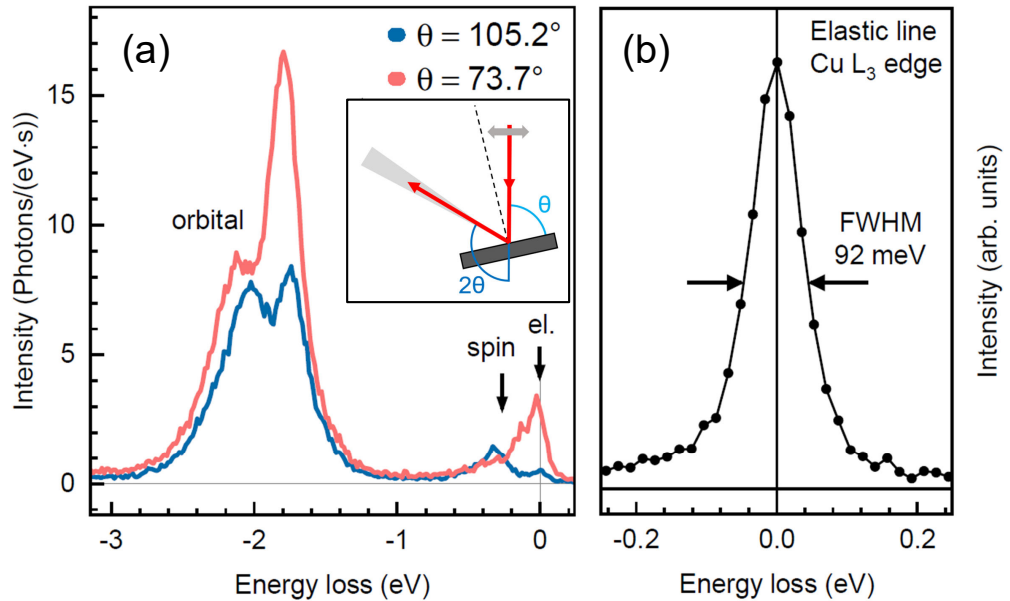
Figure 2.6: (a) Cu L-edge 2p3d RIXS of La_2CuO_4 measured at two incident angles. (b) Elastic scattering giving a combined resolving power ($E/\Delta E$) of ~10,000.

For $\theta \simeq 105°$ the single magnon is better resolved, since its energy is larger at larger momentum ($q_{\parallel}$ = 0.35 rlu) and its scattering cross section is bigger than that of the bi-magnon.

These spectra show that RIXS measured on a prototypical strongly correlated material and excited with ultra-short and intense XFEL pulses preserves its shape and can be interpreted in the same way as those measured at synchrotrons. The present energy resolution is already sufficient to study crystal field and spin excitations in cuprates and in other 3d transition metal oxides. However, the combined resolving power is limited by the beamline monochromator at the moment. When the high resolution grating will be installed, the combined band width will drop to ~ 45 meV at the Cu L_3 edge and comparatively even better at lower energies, where the edges of Ni, Co, Fe, Mn, Cr, V and Ti can be found. This means that not only orbital, charge-transfer and spin excitations, but also phonons and charge excitations [59; 2] can be studied in a pump-probe fashion exploiting high resolution RIXS at SCS. The time-resolved data collected on La_2CuO_4 is in the process of being analyzed.

2.4.2   High-Resolution RIXS of Liquids

The chemistry configuration for liquid jet samples makes use of both the high resolution of hRIXS spectrometer and the high brilliance provided by the MHz
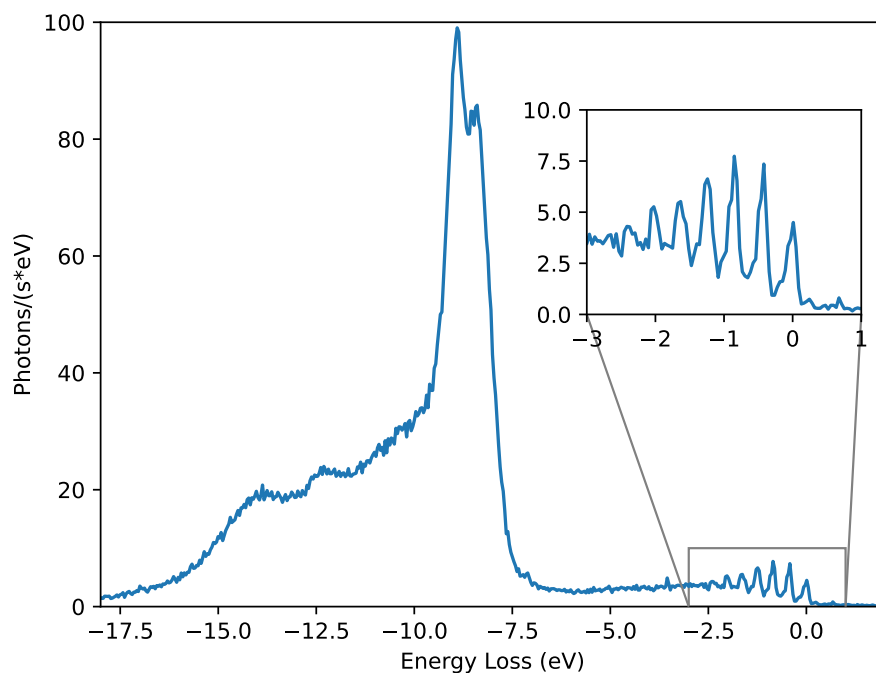
Figure 2.7: O K-edge RIXS spectrum of liquid water measured with an incident energy of 535 eV using the hRIXS spectrometer at SCS. The intermediate resolution configuration is used with a resolving power ($E/\Delta E$) of ~6,000 to observe the vibrational progression shown in the inset.

operation of XFEL. High-resolution spectra of solution samples are necessary to measure ground state vibronic progressions that can be used to characterize potential energy surfaces and probe intermolecular interactions.[55; 56] In UP2776, the O K-edge RIXS of neat liquids including water and ethanol was used establish and characterize liquid jet operation.

The high-resolution measurement of liquids is highlighted by the O K-edge RIXS of liquid water. The The spectrum of liquid water measured at 535 eV corresponding to the maximum of the O K-edge pre-edge feature is show in Figure 2.7. The spectrum was measured using a 1.1 MHz repetition rate with 400 X-ray pulses in each train. This spectrum was measured with the 1000 l/mm spectrometer and the 150 l/mm grating in the monochromator. The resulting spectrum was constructed from 20 minutes of acquisition. The combined energy resolution was measured to 87 meV based on the FWHM of the elastic line measured on a polished CoO sample at 530 eV. For these measurements the X-ray spot size was $< 10\,\mu$m in the vertical direction and $\sim 50\,\mu$m in the horizontal with the liquid jet defining the . The spectrum was collected using 1.1 MHz repetition rate of the FEL with the jet flow volume

of 2 ml/min. The spectrum exhibits the electronic excitations previously reported between 8 and 18 eV energy loss. The inset shows a closeup of the vibrational progression.

2.5   Two-color x-ray pump-probe: Nonlinear X-ray science

The high brilliance of the EuXFEL pulses, coupled to the tightly focusing KB mirrors of the SCS Instrument, opens up new capabilities to study intense x-ray – matter interactions. In this regime (x-ray intensity in the range $10^{14} - 10^{18}$ W cm^{-2}), the massive deposition of energy of an x-ray pulse to matter via photoionization/photoexcitation, and the subsequent Auger decay and electronic collisions give rise to a multitude of nonlinear effects, including superfluorescence [48; 41], stimulated x-ray Raman scattering [76; 37], x-ray induced transparency [51] or disappearance of magnetic scattering [77]. A solid target is then turned into warm dense matter (WDM), an exotic state far from equilibrium of particular relevance for astrophysics, planetary science and inertial confinement fusion. While tremendous experimental and theoretical efforts took place, especially in the last decade, to characterize and better understand the dynamics of such systems, many open questions remain: what is the origin of the disappearance of magnetic scattering? Is stimulated emission possible at all in the presence of large, dephasing electronic collisions? How fast is the electronic system equilibration, when a significant part is hot due to Auger decay? What is the timescale for electron-lattice thermalization?

On the experimental side, achieving good control of the parameters at hand is challenging:

1. At the above mentioned intensities, a solid target is destroyed after single shot interaction, thus needs to be replenished.
2. Single shot capability is required: proper triggering / synchronization of FEL pulse with sample scanner and detectors.
3. The knowledge of the applied fluence is critical, therefore careful measurements including diffraction gratings [63; 50] can help assess the peak value and also the pulse intensity spatial distribution on the sample.
4. Strategies to maximize dynamic range while preventing damage of detectors are necessary.

At SCS, 3 beamtimes dedicated to nonlinear X-ray science (Beye et al. UP 2170 (2018), Pfau et al. UP 2197 (2019), Mercadier et al UP 2593 (2021)) and one to laser-induced WDM (Cho 2021/2022 UP 2437/3216) have been performed since the start of operation. With an emphasis on UP 2593, we illustrate the capabilities of the instrument and address the 4 points mentioned above.

The original goal of experiment UP 2593 was to observe stimulated emission of the L$_\alpha$ transition in copper. To this aim, the XFEL pump beam irradiates a thin copper film above the L3 edge energy at 948 eV, to create holes in the 2p shell and, therefore,
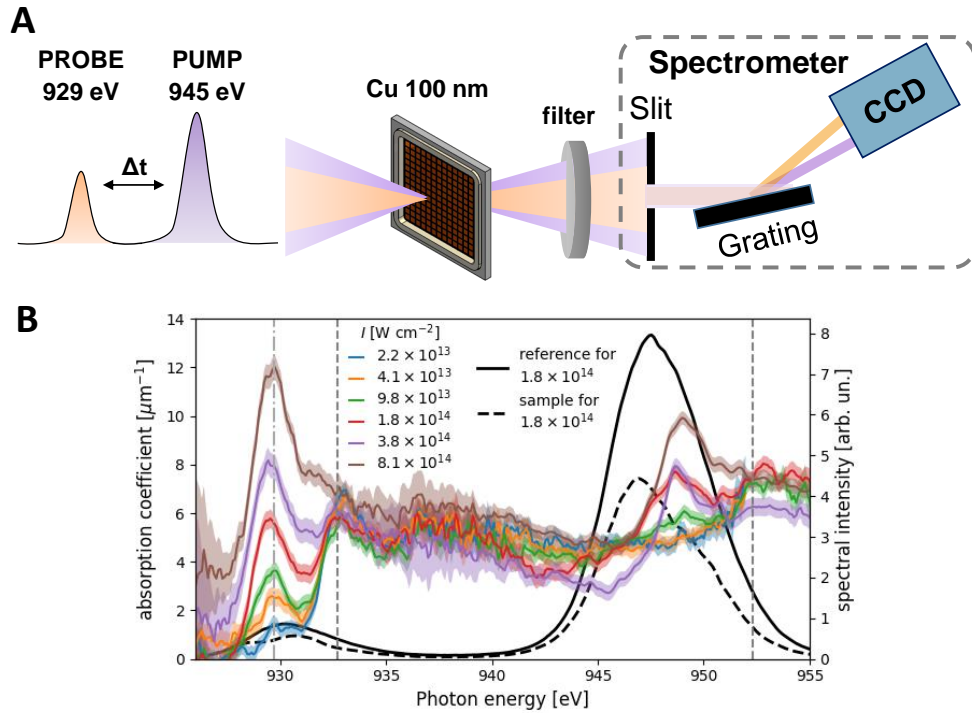
Figure 2.8: A: Schematic view of two-color experiment in copper (UP 2593). B: XAS of copper for varying intensities of the pump beam (centered at 948 eV), without delay between the two colors. The black lines are examples of spectra obtained with and without sample at $I = 1.8 \times 10^{14}$ W cm^{-2}.

a transient population inversion between 3d and 2p electrons that can lead to amplification of radiation. X-ray atomic lasers in this photon energy range are difficult to obtain because of several factors: i)Fast Auger decay rates (1 fs) quickly refill the 2p hole created by photoionization. ii) Fluorescence rates are typically a factor of 100 lower than Auger decay rates, thus stemming the stimulated emission requires high photoionization rate to outcompete the non-radiative decay. iii) In solids, the short absorption length (100 nm) of the pump combined with the relatively large focus achievable ($\sim$ 3 μm) forbids the favorable elongated geometry in the direction of the beam propagation. iv) Electron impact ionization and other collisional processes can significantly alter the electronic configuration of the 3d shell, thus perturbing the population inversion.

Points i) and ii) can be addressed by tightly focusing the ultrashort XFEL beam to maximizes the photoionization rates, thus increasing the duration of the population inversion. Point iii) can be addressed by using a seed pulse, centered on the L$_\alpha$ transition, that will give directionality to the amplification process. With such high intensity on target, warm dense matter is created within the duration of the pulse

and the number of highly energetic electrons is large, so that electron collisions and electron impact ionization processes (point iv) are unavoidable. The aim was therefore to understand if, under these conditions, seeded stimulated L_α emission can be observed, and to study the pump intensity dependence and the effect of the film thickness on the signal.

During the experiment, the **two-color special mode of operation** of the machine was successfully employed: it allows the generation of two SASE pulses with arbitrary photon energy (reachable within the range given by the electron energy) and includes a variable time delay between 0 and 1000 fs using a magnetic chicane. The optical chicane for scanning to negative delays is not yet available, but foreseen. With this scheme, a copper thin film was irradiated with a strong pump beam centered at 948 eV, above the L_3 edge to deplete the 2p shell, and a weak seed (or probe) beam, centered on the L_α transition (929 eV). The seed beam was generated by the upstream cells of the undulator while the pump beam was using the downstream cells. The beam sizes and focii positions were characterized both by knife-edge scans and the grating technique prior to the beamtime, as described in Section 3.1.6. Because of the different source points of each color, the focii position were shifted by ~ 12 mm. It was possible to switch on/off the pump beam without affecting the seed beam, and to control the relative intensity ratio between the two colors. The maximum pulse energy in this mode was close to 2 mJ per pulse in the pump beam, which, after beamline transmission correction, gave about 600 μJ per pulse on target, for a smallest focus size of 3.5 μm.

A **user-provided spectrometer** was installed in forward direction to analyze the transmitted beams. With sufficient time ahead of the experiment, the spectrometer was integrated into the SCS Instrument. It was attached to the FFT chamber and supported by a modified version of a movable platform originally designed for the FCCD detector. The integration of the spectrometer motors and detector (Andor Newton CCD camera) into Karabo was successful.

A schematic view of the setup is shown in Fig. 2.8A. The two colors beam impinged on a Cu target supported by a 15 μm deep Ni mesh. To **maximize the dynamic range of detection** and prevent damage of the detector, the transmitted beams were attenuated by Al filters of selectable thickness (3.5, 5 and 10 μm) before entering the user spectrometer. In addition, the use of a beam block close to the CCD chip of the detector allowed to selectively block the intense pump beam radiation. To achieve **single shot irradiation**, the XFEL delivered one pulse per train and the sample was mounted on the Fast Solid Sample Scanner (FSSS) which was rastered to ensure a fresh irradiation site at 10 Hz. Details of sample rastering and synchronization between the FEL, the sample scanner and the detector can be found in Section 3.4.1.

This setup allowed to perform XAS on XFEL-pumped Cu at the L_3 and L_2 edges, as shown in Fig. 2.8B. Averaged spectra with and without sample were collected to measure the absorption as a function of pump intensity and pump-probe delay. The XAS spectra reveal drastic alterations of the electronic structure, well within the 15 fs pulse duration. In such a highly collisionnal plasma, the initial population inversion of the 2p shell cannot be sustained long enough to lead to an amplification, which is the reason why no L_α stimulated emission was measured. Instead, reverse saturable absorption (RSA) was observed: the depletion of the 3d shell due to electron collisions opens up an absorption channel from the 2p to the 3d shell, which occurs both at the L_3 (around 929 eV) and the L_2 (around 948 eV) edges. The excited state becomes more absorbing than the ground state (RSA). The experiment was also conducted with a single color SASE beam at both the L_2 and L_3 edges. In this case, the pulses are used to simultaneously create warm dense matter and characterize its transient state via XAS. The findings of this study are reported in [49].

Finally, the two-colors operation mode, combined with a forward geometry spectrometer, allows the investigation of XFEL-created WDM in an unprecedented way. It is now possible to follow the electron dynamics induced by a strong XFEL pulse via XAS with femtosecond accuracy. Such experimental data will be crucial to improve the general understanding and benchmark theoretical models. Future developments are foreseen: it should be possible to scan the probe photon energy to extend the measurement range, currently limited to the SASE bandwidth. Also, this scheme is not limited to the study of solids but can be combined with the CHEM chamber to investigate liquid jets. With liquid jets, the high repetition rate of EuXFEL can be fully exploited to speed up data collection. Finally, the pulse duration could be shortened. In a recent facility development campaign, a spectrum containing a single, broad SASE spike (thus suggesting 100s attosecond duration) was generated and even tested in two-color mode. How do the XAS spectra evolve with shorter pulse duration? Are collisions fast enough to give rise to RSA or can a sustainable population inversion be established, thus leading to stimulated emission?

3 Instrumentation in operation

The linear accelerator of European XFEL distributes electron bunches to all SASEs within a train of 600 µs at 10Hz repetition rate (Figure 3.1). An electron switch devides the electron pulse train and delivers it to SASE2 FEL in the north branch and to SASE1 and SASE3 FEL in the south branch. The hard X-ray SASE1 and the soft X-ray SASE3 share the same electron beam transport. This couples in particular the operation conditions between the SASE1 and SASE3 beamlines and subsequently between the instruments. To mitigate coupling between experiments a so-called "fresh bunch" technique is introduced. Using a combination of fast kicker in front of SASE1 and and a quadrupole kicker in SASE3, the lasing of SASE3 electron bunches in SASE1 undulators and vice versa is suppressed [45]. Since the SASE1 background radiation from SASE1 bunches in SASE3 can corrupt data at SASE3 experiments when slow detectors are used, the suppression has to be sufficient enough. In addition fixed sample targets are exposed to the SASE1 background radiation which can cause sample heating or even sample damage under focused beam conditions in a single shot as encountered in SCS early user experiments. Depending of the ratio of the number of bunches in SASE1 and SASE3 and depending on the SASE3 photon energy, the background radiation from SASE1 pulses in SASE3 undulators can be effectively reduced by two orders of magnitude.
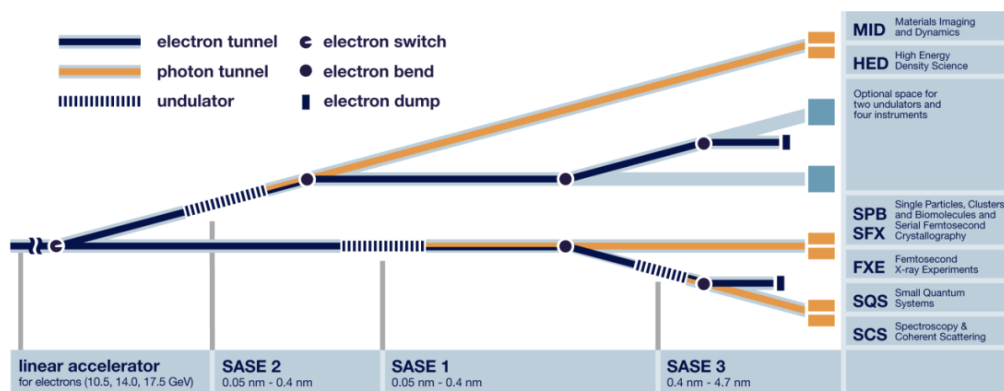
Figure 3.1: Layout of European XFEL facility.

3.1   X-ray beam delivery

Flexible operations modes have been established between SASE1 and SASE3
which are illustrated in Figure 3.2. An even distribution of pulses between SASEs
gives a 150 µs window per instrument. The electron pulse pattern between SASE1
and SASE3 can then be either in 10 Hz mode, in so-called "interleaved" mode or in
5 Hz mode. Compared to 10 Hz operation mode, the 5 Hz mode divides the SASE1
and SASE3 bunches in trains which allows, in combination with a train picker (e.g.
installed at SCS), for blocking SASE1 background reaching the SASE3 experiment.
The data rate remains the same between the experiments. This scheme can be
extended to variable train-to-train patterns at other repetition rates as shown in Fig.
3.14.

In interleaved operation SASE1 and SASE3 electron bunches alternate in the train
over the shared time window. The interleaved mode thus extends the pulse train
up to 400 µs doubling the data rate beneficial for experiments at lower repetition
rates. The mode requires a pulse resolved detection scheme insusceptible to the
SASE1 background radiation. The interleaved mode became the standard operation
mode between SCS Instrument and SASE1 instruments where the machine runs at
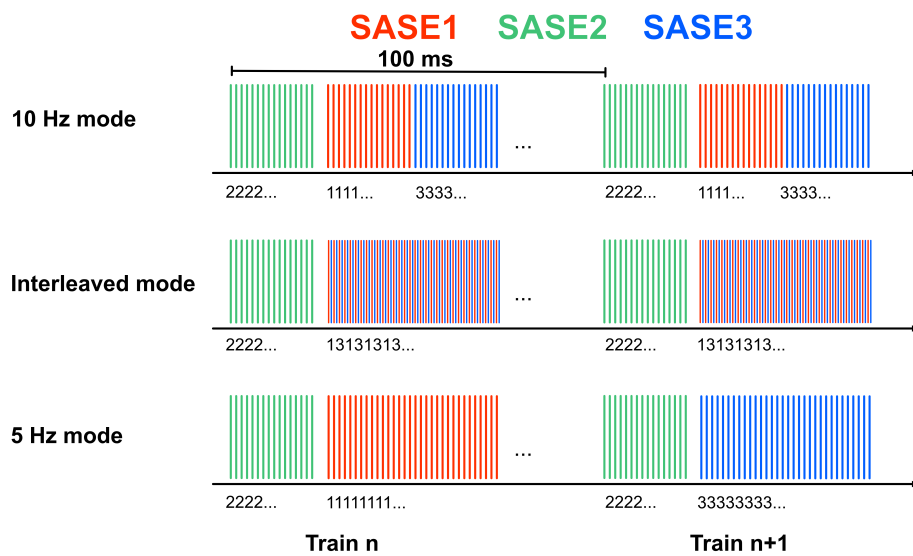
Figure 3.2: **Pulse distribution modes**. Pulse train is divided between SA2 (south branch) and
SA1/SA3 (north branch). Possible pulse patterns for the north branch between SA1 and SA3:
(top) individual SA1 and SA3 rf-windows , (middle) individual SA1 and SA3 trains and (bottom)
SA1/SA3 interleaved mode

2.25 MHz delivering SASE pulses at 1.13 MHz to each experiment. The repetition rate can individually be reduced to avoid sample heating in laser-driven material dynamics of fixed targets.

3.1.1   Electron energy operation modes

The FEL operation at different electron energies of 16.3 GeV, 14 GeV, 11.5 GeV and 8.5 GeV extends the photon energy range. Figure 3.3 shows the attainable photon energies for the different working points of the FEL. Resonant core spectroscopy is of key importance for complex material studies at the SCS Instrument where the vast majority of experiments demand studies at the 3d transition metal (TM) L edges, carbon, nitrogen and oxygen K edges as well lanthanides M edges. They all reside in the soft x-ray energy range from 250 eV to 1500 eV. At 16.3 GeV the photon energy range includes only the Cu edge of the 3d TM series and extends into the tender x-ray range. At 14 GeV studies of the Fe, Co and Ni L edges become possible. The Ti L edges and oxygen K edge can be reached at 11.5 GeV. Operating the facility at 8.5 GeV includes the carbon and nitrogen K edge. In terms of user requested photon energy requirements, science program and instrument capabilities the 11.5 GeV and 14 GeV will cover most of the requirements, while 16.5 GeV greatly limits the science program and user operation.
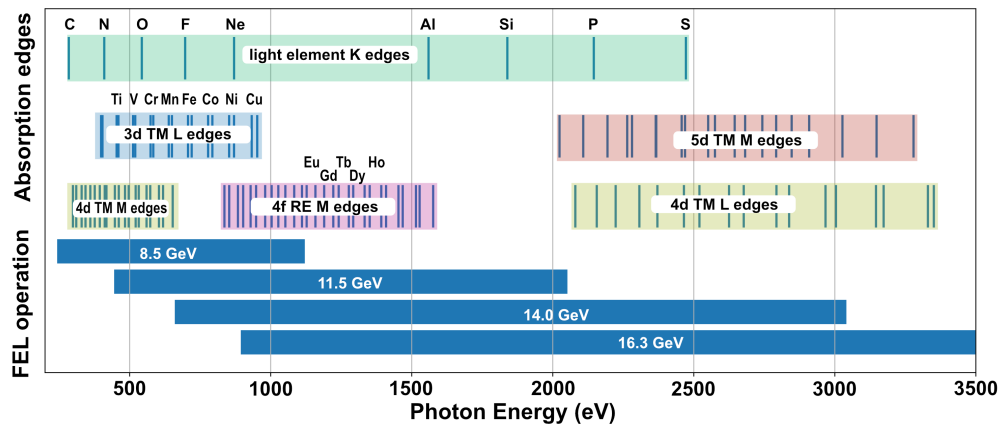
Figure 3.3: FEL operation modes and SASE3 attainable photon energy ranges to perform resonant X-ray spectroscopies at SCS. The photon energy range is defined by the SASE3 undulator period of 68 mm and a *k* parameter range between 4.0 to 9.0 where a SASE3 undulator gap of 11 mm corresponds to *k* = 8.8

3.1.2 SCS beam transport

The X-ray beam transport is shown in Figure 3.4. Distances of the X-ray optical elements are listed in the table Table 3.1. The horizontal beam offset mirrors (M1 and M2), the soft X-ray monochromator (M3a,b, G1, G2, M4) and the SCS distribution Mirror (M5) are located in the tunnel Figure 3.4a.

The horizontal offset mirrors M1 and M2, a combination of flat and adaptive optics, allow for removing spontaneous radiation and offer the option of an intermediate horizontal focus. The incident angle of both x-ray optics, θ_1 and θ_2, can be adjusted between 9 mrad to 20 mrad. The mirror clear aperture can therefore be optimized to the source divergence which is important at lower photon energies where the
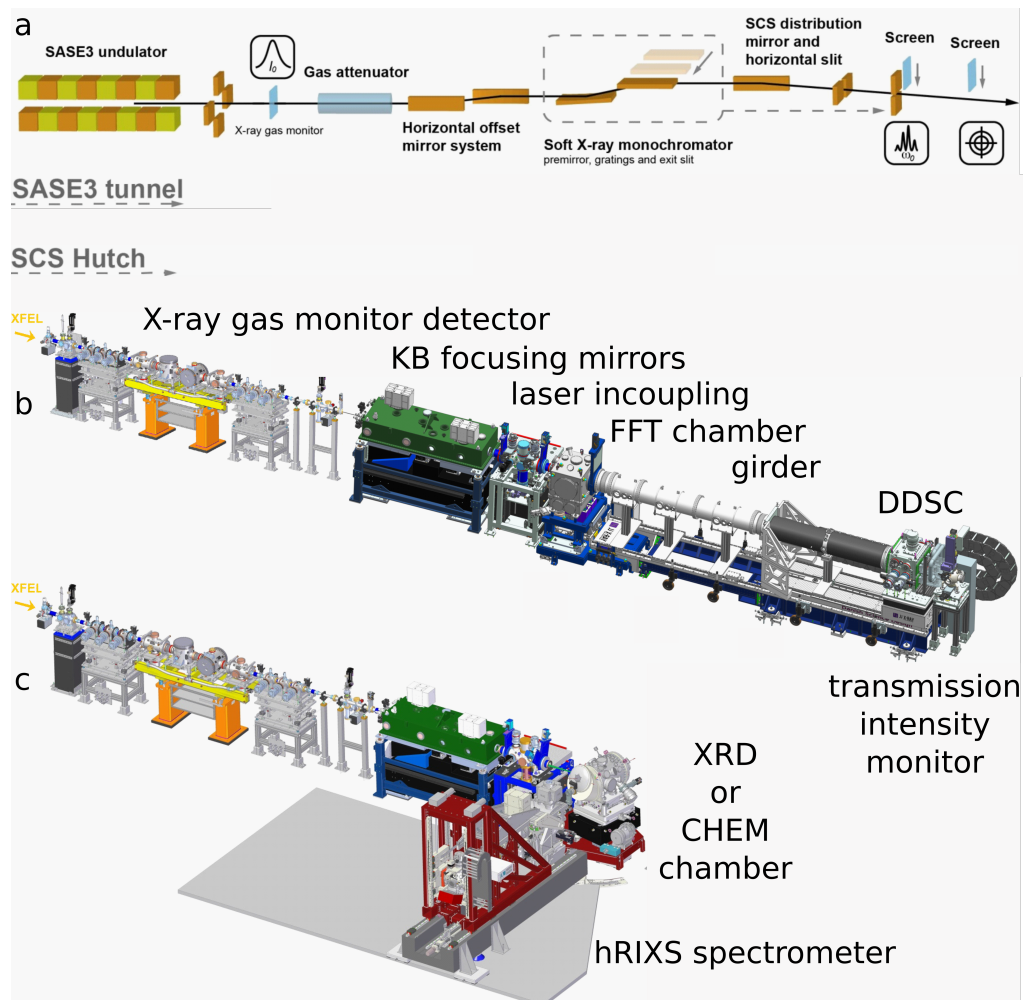
Figure 3.4: a: schematic layout of SASE3 beamline. SCS Instrument layout for experiments in foward scattering geometry (b) using FFT chamner and DSSC (or PiMTE3), and back scattering geometry (c) using XRD or CHEM chambers together with hRIXS spectrometer.

Table 3.1: X-ray optical component list of the SASE3/SCS beamline and their distances to the SASE3 source point.

Optical element	Type	Plane	Distance [m]
SRC	Source	–	0.0
M1	Offset	Hor	281.0
M2	Offset, adaptive	Hor	283.9
VSLIT	Mono aperture	Ver	298.5
M3a	Mono pre-mirror	Ver	299.4
M3b	Mono pre-mirror	Ver	300.4
G1	VLS 50 l/mm	Ver	301.0
G2	VLS 150 l/mm	Ver	301.0
M4	Flat mirror	Ver	301.0
M5	Distribution	Hor	339.0
IFH	Intermediate Focus	Hor	374.0
EX	Mono exit slit	Ver	400.0
M7	Bent KB	Hor	426.7
M8a	Deflecting	Ver	427.4
M8b	Bent KB	Ver	428.0
SAM	Sample	–	430.0
XBD	beam dump	–	437.8

source divergence is larger. In addition, higher harmonics of the source can be effectively suppressed at larger incident angles. The typical working point for SCS is $\theta_{1,2} = 20$ mrad providing a high transmission of B_4C-coated X-ray optics up to 1500 eV and an effective suppression of the higher harmonics above 750 eV. For the higher photon energies a working point of $\theta_{1,2} = 9$ mrad is used covering a high beamline transmission range from 1.0 keV to 3.0 keV.

As a branch line the beam offset generated by the horizontal offset mirrors is compensated by the SCS M5 distribution mirror. In this way the horizontal beam pointing in the SCS beam line is not changed. In the standard beam configuration an intermediate horizontal focus (IHF) is generated which forms the source point of the horizontal KB mirror in the SCS hutch. In addition horizontal slits can be closed down at the IHF increasing the intensity jitter as a trade-off for spatial stability of the source
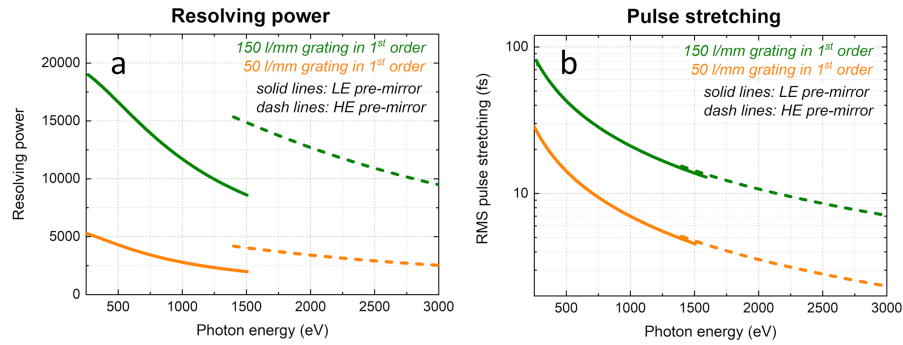
Figure 3.5: Resolving power (a) and pulse stretching by the monochromator (b).

point.

All working points are tabulated in the control system and updated during instrument start after a shutdown period. Switching beam configuration is readily possible from high-level beamline controls and takes up to 30 min limited by the motor speed of mirror translations. Manual tuning assures proper beam pointing.

3.1.3 Monochromatic beam operation

The majority of experiments performed at the SCS Instrument utilize monochromatized beam. The SASE3 beamline is equipped with the grating monochromator which can be used to reduce the bandwidth and improve the longitudinal coherence of the SASE beam. The results from the commissioning of the soft X-ray monochromator including the design constraints are detailed in [25]. The monochromator consists of a focusing elliptical pre-mirror and a plane VLS (variable line spacing) grating. Two premirrors, a low-energy (LE) premirror and a high-energy (HE) premirror cover the energy range from 250 eV to 3000 eV. A baseline grating with 50 lines/mm was chosen as the lowest line density that can be manufactured. The low line density minimizes pulse elongation by the grating. Minimizing the time-bandwidth product, i.e. making the best compromise between temporal and photon energy resolution, is specific to FEL sources. It imposes very tight demands on the quality of optical elements because the ultimate goal is to reduce all aberrations below the resolution limit of an ideal grating. The design foresees a 500 mm-long grating allowing more than 4σ transmission of the Gaussian-like beam profile over most of the operation range of SASE3. However, limitations in production capabilities, in particular in terms of VLS accuracy, lead to a 120 mm-long grating with 50 lines/mm which was installed at the start of operation. This grating provides a moderate resolving power of about 2000 - 5000 along with

pulse stretching of a few femtoseconds to a few tens of femtoseconds RMS (Fig. 3.5). For experiments demanding higher temporal resolution, it is possible to reduce the number of illuminated grooves by closing the aperture located prior to the grating. This reduces pulse elongation at expense of photon energy resolution.

To achieve higher photon energy resolution, a feature indispensable for hRIXS experiments, a 120 mm-long grating with 150 lines/mm has been added to the monochromator. This grating increases the resolution to >10000 at expense of larger pulse elongation than the 50 lines/mm grating (Fig. 3.5). The new grating was installed for the start of hRIXS commissioning in the beginning of 2021. The resolving power reaching 10000 has been confirmed by hRIXS experiments.

3.1.4   Gap scan

The monochromator operates in two modes: either with fixed photon energy, or scanning over the photon energy. To minimise variation in x-ray intensity at the sample while scanning, the undulator gap is synchronised to the monochromator. To record a XAS spectrum (see Section 2.1 on page 15), the monochromator is scanned continuously back and forth between two energy end point with the help of a middle layer device developed by the control group and X-ray optics group. The undulator set energy follows the monochromator energy position value with a proportional–integral–derivative loop and communication system developed by control, X-ray optics group and undulator group. The routine can perform scans over more than 100 eV which is fully sufficient to cover for example the $L_{3,2}$ edges of 3d transition metals. For larger changes in photon energy the SASE performance goes down and tuning may be required. The grating pitch motor speed is reduced such that change in photon energy within a train is smaller than the energy resolution of the monochromator.

3.1.5   Gas attenuator

The intensity of the X-ray beam is adjusted using a gas attenuator [13]. Especially for delicate samples, attenuations down to a factor 1000 can be necessary. The attenuation is done by leaking nitrogen gas into a section of the beamline. From the known absorption properties of X-rays in nitrogen, the gas pressure to attain the desired attenuation is calculated. Mass flow controllers are then set to roughly reach this gas pressure in the absorption cell.

3.1.6 X-ray focusing

The diversity of the experimental techniques offered at SCS calls for a high flexibility in setting the X-ray beam size at the sample in order to reach feasibility and optimize the experimental conditions of a given experiment. To achieve this goal the SCS Instrument is equipped with two Kirkpatrick-Baez (KB) mirrors providing independent control of horizontal (HFM) and vertical (VFM) X-ray beam dimension at the sample plane from $\approx 1\,\mu m$ to $500\,\mu m$ [50]. To maintain the beam horizontal after the KB mirrors, a flat vertical deflecting mirror (VDM) is introduced between HFM and VFM. In particular, beam sizes $\leq 10\,\mu m$ are essential to perform CXDI, RIXS and non-linear X-ray spectroscopy, while X-ray spectroscopy and X-ray scattering in the linear fluence regime benefit from larger beams of $10 - 100\,\mu m$. The size of larger unfocused beams is determined by knife edge scans, while curved gratings are employed as real-time tool to characterize µm-focused X-ray beams. A curved grating is a portion of a zone-plate with suitably varying period and orientation, which provides on a 2D detector the far-field diffraction pattern containing magnified images (in each diffraction order) of the X-ray spatial fluence distribution at the grating plane [65; 64]. This approach allows real-time characterization of micrometer-sized X-ray beams and its accuracy has been demonstrated by the comparison with the state-of-the-art ablative imprints [50].

To determine FEL horizontal and vertical focus at interaction point, HFM and VFM were bent while measuring the beam profile using the curved grating setup. The smallest horizontal and vertical foci are respectively $2.48(7)\,\mu m$ and $1.21(3)\,\mu m$, obtained with open horizontal slits and exit slit gap of $21\,\mu m$. These very small focal sizes accompanied by structureless and Gaussian-like beam profiles result from the

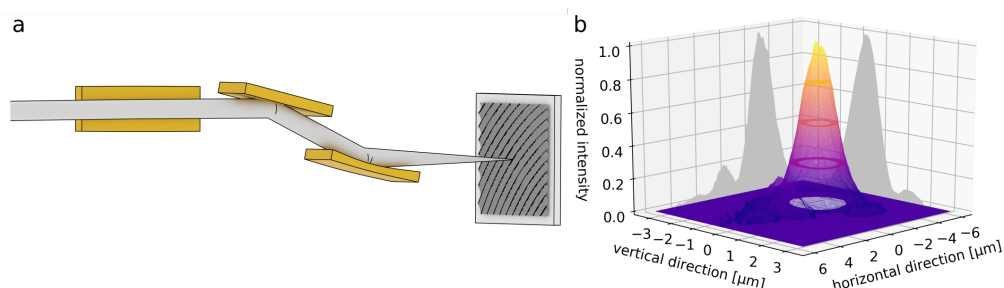**Figure 3.6:** Sketch of curved grating experimental setup (a), with HFM, VDM, VFM and grating (not in scale). b: average of 905 images obtained by curved grating measurements with the beam at horizontal and vertical focus. The maximum intensity is normalized to one. Circular sections indicate the contour area at few specific fluence levels. Projections along horizontal and vertical directions are marked in grey.

high quality of the KB mirrors with rms slope errors approximately 100 nrad. Note that, these results were obtained using the FastCCD detector, running at 10 Hz, therefore beam dimensions represent an upper limit since they refer to the average over the pulse train, and do not account for possible pulse-to-pulse jitter within the pulse train discussed in section 3.3.

When the SCS Instrument is operated in monochromatic mode, the vertical beam size at the sample is determined by the size of the exit slit gap. The gap size corresponding to the best energy resolution is given by the monochromator resolving power. The monochromator grating with 50 l/mm in first diffraction order delivers at 775 eV a resolving power of 3000, hence an energy resolution of 258 meV. Given a dispersion of 2.18 eV/mm at the exit slit plane, for ES gaps smaller than 120 μm, the energy resolution is not further improved. Nevertheless the vertical beam size can be further decreased at expense of the beam intensity at the sample. Similarly, the minimum horizontal beam width of 2.5 μm can be further reduced by decreasing the gap of the horizontal slit, which represent the source object of HFM mirror. A smaller horizontal beam size at the sample could therefore be obtained by reducing the HS slit gap at the expense of the FEL intensity at the sample.

Another equally important property of a KB system is reproducibility. We have shown that a given bending degree of KB mirrors, corresponding to a certain beam dimension at the sample plane, can be reproduced and unambiguously determined by three capacitive displacement sensors, installed at the back of each mirror substrate. These provide a quick, accurate and reproducible procedure to obtain a desired beam dimension.

3.2   Optical beam delivery

The majority of User experiments at SCS require optical laser pulses in addition to the X-ray pulses from the FEL. The two sources are used in a pump-probe configuration to make time-resolved measurements with a time resolution down to a few tens of femtoseconds.

The optical laser (referred to internally at the PP-laser) was developed in-house [52; 53] to match the burst-mode pulse pattern of the FEL while providing a range of pulse energies and durations. Each SASE is equipped with a similar laser.

The laser system comprises an all fiber, chirped pulse amplifier, whose input is a low noise fiber seeder, and whose output is used to produce a white light continuum (WLC) and seed an Yb:YAG Innoslab power amplifier chain, operating at 1030 nm. The frequency-double output from the Yb:YAG amplifier pumps a three-stage non-colinear parametric amplifier (NOPA) which amplifies the WLC at 800 nm. SCS and SQS each have a dedicated NOPA, which share a common seeder and amplifier chain.

The dispersion of the WLC is used to control the 800 nm pulse duration between <15 fs to 300 fs. The 15 fs pulses are generated with a slight negative chirp and are compressed by material dispersion in fused silica to reach the transform limit at the sample. Longer pulses are compressed to the transform limit using a transmission Treacy compressor.

The laser has four working points for repetition rate and pulse energy: 4.5 MHz (63 μJ), 1.1 MHz (260 μJ), 188 kHz (1.5 mJ) and 113 kHz (2.5 mJ).

Both the 800 nm beam from the NOPA and the 1030 nm NOPA pump beam can be delivered to the Instruments via a separate laser hutch. To date SCS has made use of only the 800 nm beam. It is either used directly or undergoes frequency conversion. In both cases it passes over a mechanical delay line before being routed to User experiments. Frequency conversion is done by second- or third harmonic generation (SHG and THG) in beta barium borate (BBO) cyrstals, or using a commercial OPA (Topas-prime from Light Conversion). The OPA is can output from the UV (250 nm) to mid-IR (15 μm) and is configured to operate at 113 kHz or 1.1 MHz with 30 fs to 50 fs, 800 nm pulse input.

Delivery of the optical laser beams to experimental endstations can be done either via a dedicated beamline component (Laser IN-coupling, LIN) just upstream of the endstation, or directly into the endstation. LIN in-coupling gives a non-collinear angle

between the FEL- and optical beams of about 1°, but it is relatively far away from the sample, which increases the focal spot size. The LIN cannot be used with the BOZ because they block the path. Coupling into the endstation increases the non-collinear angle but allows shorter focal lengths and therefore smaller foci. In either case, an in-vacuum mirror mount is used to steer the beam onto the sample and overlap it with the X-ray beam.

To date focusing of the optical beam has been done with a lens in air. The lens is mounted on a linear translator so that the spot size on the sample can be easily changed. Off-axis parabolic focusing is foreseen in the FFT and XRD endstations, particularly for mid-IR and THz radiation.

3.3 Spatial and temporal beam stability

3.3.1 FEL pointing stability

Dedicated studies of horizontal and vertical train-to-train positional jitter were performed by means of the curved grating setup with KB mirrors set to provide horizontal and vertical focus [50]. The histograms of the horizontal and vertical beam positions are reported in Figure 3.7a and b, respectively. Both distributions follow a Gaussian statistics with FWHM 3.4 μm and 0.4 μm, respectively. The larger horizontal positional jitter is assigned to the jitter of the source and/or to mirror vibrations. Additional measurements performed with the pulse-resolved detector DSSC (ref) provided a FWHM pulse-to-pulse horizontal jitter of 1.2 μm within a pulse train. The latter is assigned to source pointing jitter, since mirror angular vibrations at frequencies ≥ 100 kHz can be neglected [68]. A reduction of the train-to-train horizontal pointing jitter can be achieved by smaller HS gap size, leading to a more confined intermediate source point.

In general, the positional jitter along the vertical direction is expected to be smaller than in the horizontal because of the following reason. At the ES the beam is energy-dispersed along the vertical direction, therefore pointing instabilities of the beam upstream will translate mostly into intensity rather than positional jitter, and will lead to worse energy resolution. This makes beam width and position at the sample plane less sensitive to vertical FEL pointing jitter.
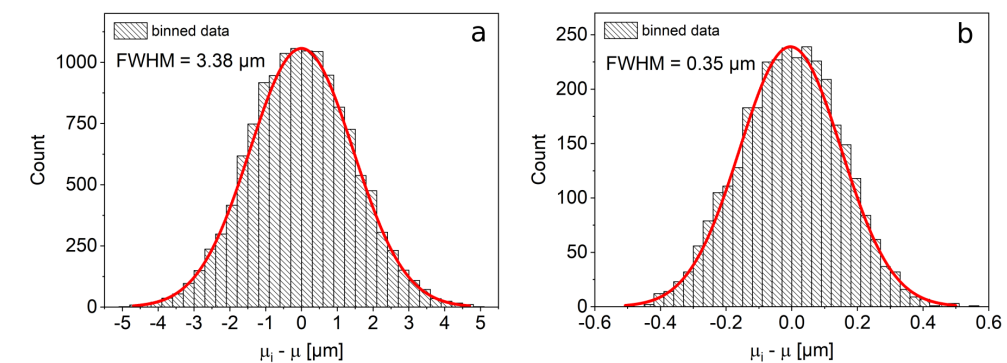

Figure 3.7: Horizontal (a) and vertical (b) positional jitter of FEL beam with the focus of HFM and VFM at the first interaction point. FWHM values refer to the Gaussian fit of the binned data.

3.3.2 Spatial overlap between FEL and PP laser

Spatial overlap between the FEL beam and the OL beam is achieved by first monitoring each beam on a piece of pyrolytic boron nitride (pBN) or Ce-doped yttrium aluminium garned (Ce:YAG) screen at the sample position. Then, the PP laser beam is steered by the motorized in-vacuum mirror. Since there is a non-negligible angle between the FEL and PP laser, there are a few precautions to take when achieving spatial overlap, especially when the size of the beams are smaller than ~ 50 μm: i) the plane of the monitoring screen must match that of the sample. This is accomplished by appropriate design of the sample holder on one hand, and by adjusting the Z position of the sample, using a far distance microscope with small depth of field on the other hand. ii) the spatial jitter of the OL, which is dominating compared to that of the FEL, must be reasonably low to achieve homogeneous pumping.

While passive limiting solutions are implemented, such as limiting the air flow via an enclosure of the beam path from the ILH to the in-coupling window of the experimental chamber, spatial jitter and drifts are inevitable, to a certain extent. The temporal structure of the 10 Hz burst mode makes active feedback based on position monitoring difficult to implement. Hence, the focused beam position on sample must be monitored, as shown in Fig. 3.8. The focused beam is picked off after the lens by a beam splitter (it can be the reflection from the in-coupling window in case of non-normal incidence) and sent to a camera located at the same distance from the lens as the sample. The camera operates at 10 Hz with a resolution of 4.4 μm, and allows a full characterization of the beam profile, position and intensity. A filter wheel increases the dynamic range of the camera for varying intensity and number of pulses. To resolve intra-train drifts, a position sensitive diode is foreseen.
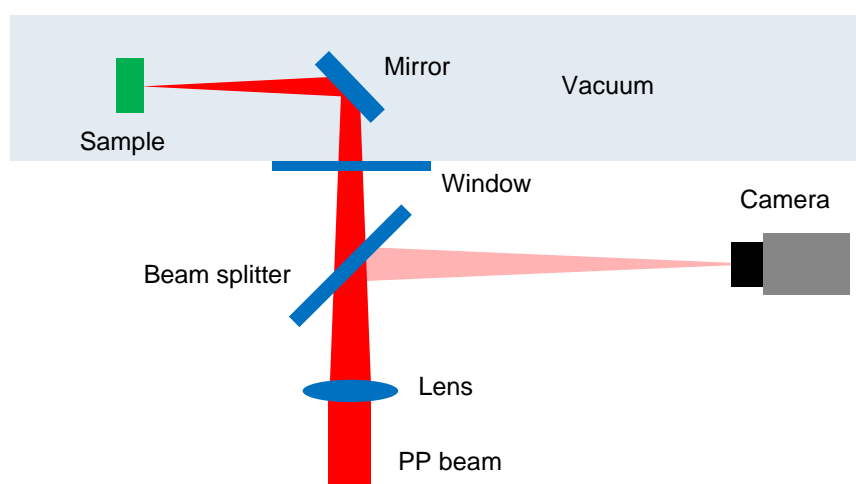

Figure 3.8: Spatial jitter monitoring.

3.3.3   Temporal (longitudinal) stability

To ensure temporal overlap between the XFEL and the PP laser pulses, both must be locked to the optical reference system (LbSync). On the PP laser side, this locking is done as follows: an optical reference is generated and transported from the laser gun to the laser hutches, 3.4 km downstream, via a fiber. The PP laser pulse arrival time is measured against the reference at several steps in the amplification chain. This information is used to feedback on the oscillator cavity length and allows the PP laser to be synchronized to the LbSync reference. There are two types of locking mechanisms, depending on the desired accuracy and timescales: RF-locking enables an RMS jitter of 50 – 100 fs and arbitrary delay up to 18.5 ns. Optical-locking allows a typical RMS jitter of 5 fs, and requires an optical delay line to adjust the delay by typically ±1 ns. On the FEL side, several bunch arrival time monitors (BAM) placed along the tunnel are available for timing diagnostic and feedback. The BAM uses a relative measurement method [61] which compares the timing of each electron bunch against a laser pulse provided by the optical reference system (LbSync). Based on these measurements, fast and slow feedback mechanisms are implemented and can be used upon request for improved longitudinal stability. When these feedback loops are active, the arrival time at 414 m from the injector laser is stabilized to a fixed arbitrary value with inter-train RMS jitter of ~ 6 fs and intra-train RMS jitter below the resolution of the BAM (3 fs) over many hours. Despite this impressive stability, the most downstream BAM (1932 m from the laser gun) measures long-term drifts on the
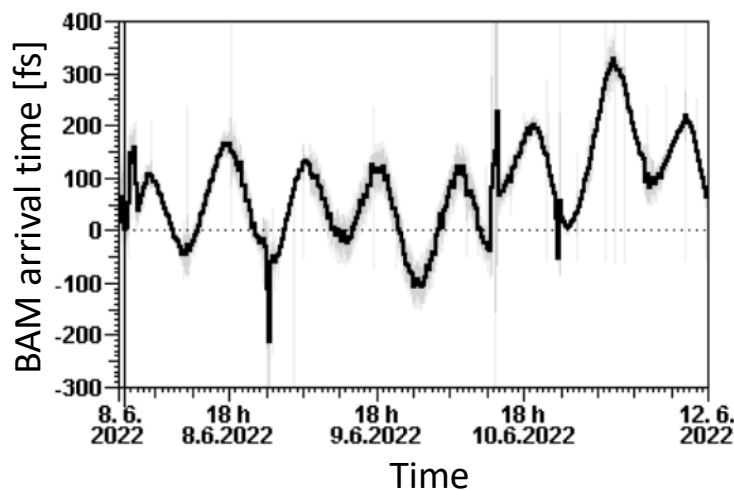

Figure 3.9: BAM 1932S average arrival time measured over 96 hours. The oscillatory behaviour is linked to the oceanic and terrestrial tides that affect the length of the accelerator in a complex manner. The few spikes observed are generally due to issues with the machine (loss of beam, loss of feedback mechanism, ...) and must be closely monitored during an experiment.

order of hundreds of femtoseconds that seem to correlate, in a complex way, with tidal effects (see Fig. 3.9).

Currently, the last BAM measurement with respect to the optical reference is performed 1.5 km away from the interaction point with BAM 1932S, prior to all transport optics to the SCS hutch. The PP laser arrival time is performed ~ 20 m away from the interaction point. While many sources of jitter and drift can play a role during transport of the two beams, we measured in a dedicated experiment the arrival time of the XFEL pulse with respect to that of the PP laser pulse at the interaction point and found that the main source of drift is due to the accelerator. A pulse arrival time monitor (PAM) device based on spectral encoding [23] measured the pulse-resolved arrival time over 3 hours. The results are summarized in Fig. 3.10. In Fig. 3.10 A, the PAM and BAM arrival times linearly correlate with proportionality of 1.17. This coefficient is larger than one, which is consistent with an amplification of the drift observed at BAM 1932S due to movement of the entire accelerator arm. In Fig. 3.10 B, the history of PAM and BAM is shown, with panels C and D showing the corresponding histograms. The two valleys in both plots are due to the short interruptions of data taking around the first and second hours of measurement. The PAM data follows a similar trend as the BAM data and shows a significant spread of arrival time with FWHM of 100 fs. Knowing the proportionality coefficient between
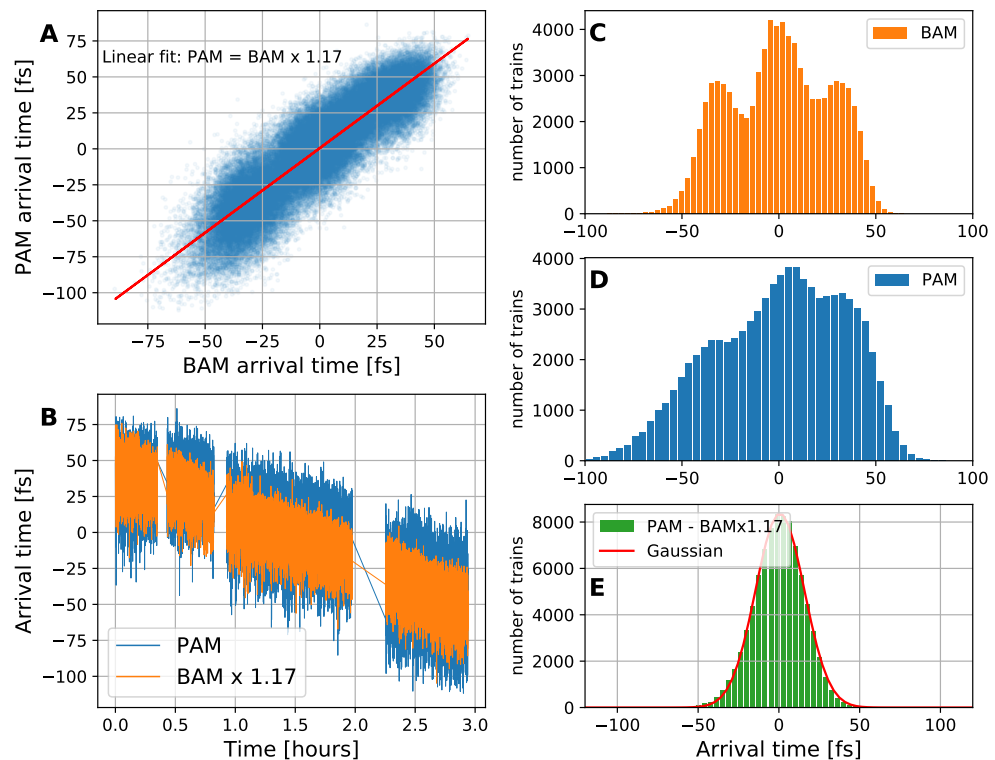
Figure 3.10: PAM vs. BAM analysis.
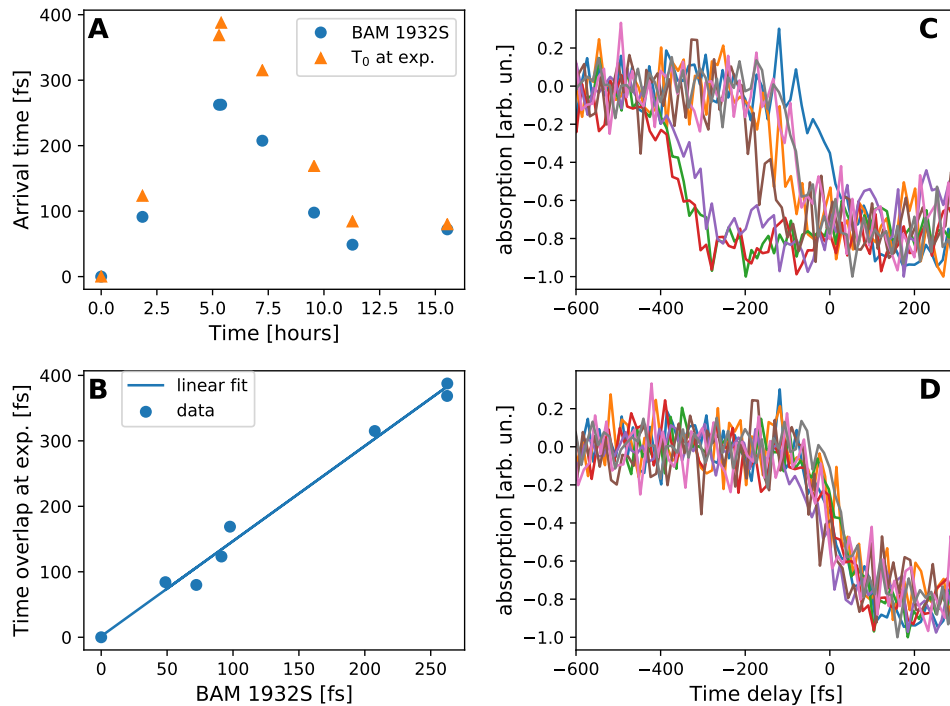
Figure 3.11: Regular check of time overlap during UAC 2769 significantly increased the time resolution. A: BAM arrival time and time overlap from time-resolved XAS measurement measured periodically over 16 hours. B: Correlation between the two signals show a BAM amplification factor of 1.45. C: Uncorrected XAS time traces (from which the points in A are extracted). D: Corrected time traces using the BAM correlation with BAM data.

PAM and BAM, we correct the PAM arrival time by the BAM data in Fig. 3.10 E. The distribution becomes normal with a standard deviation of 15 fs (FWHM of 35 fs). This reduction in the spread of arrival time shows that the accelerator is the main source of drift.

The conclusions and consequences of this analysis on time resolution of a pump-probe experiment at SCS can be summarized as follows:

1 With slow and fast longitudinal stability feedback enabled, the XFEL inter- and intra-train arrival times are extremely stable within 10 min, with RMS jitter < 10 fs.

2 Despite the feedbacks, slow drifts of the accelerator are observed in the tunnel and amplified at the interaction point. The amplification coefficient varies on unknown timescales, and was measured between 1.17 and 1.45 in several time-resolved experiments so far.

3 Without a PAM device close to the interaction point, it is possible to account for the accelerator drifts using the BAM data, assuming the amplification factor

known.

4   Regularly checking time overlap at the experiment, whether by performing a delay scan on the sample of interest or transient reflectivity change on a SiN membrane is currently the best way to increase the temporal resolution of an experiment. In addition, these regular checks enable the determination of the amplification factor, pending the main source of drift remains the accelerator. This is examplified in Fig. 3.11. During UAC 2769, time-resolved fluorescence showed a sharp step function around the time overlap between the 400 nm PP laser beam and the FEL at the Ni L_3 edge and allowed to periodically check for timing drifts. An amplification factor between BAM and the time arrival at the interaction point of 1.45 was found (Fig. 3.11 B). Using this data, the time axis can be corrected and leads to a significantly reduced spread of arrival time determination, from 500 fs to 50 fs (C and D). In between the measured points, where spectra at fixed delays were measured, it is possible to interpolate Fig. 3.11 A to correct for the accelerator drifts.

5   Interruption of beam delivery or timing-related issues are extremely important to monitor since they may perturb the arrival time of the XFEL pulses.

3.4 Experiment stations and sample environments

The SCS Instrument provides fixed target and liquid jet sample environments to users, realized in three different experiment stations and optimized for various x-ray spectrocopy and scattering techniques (see Figure 3.4 on page 38). The Forward-scattering Fixed-Target (FFT) experiment station enables forward scattering scattering techniques (XAS, SAXS, X-ray Holography) and the X-Ray Diffraction (XRD) allows for backscattering geometries (XRD, RIXS, X-ray reflectivity). Both stations have sample holders for fixed targets. The CHEM experiment station provides a liquid jet sample environment for RIXS and XAS studies.

The current practice is a changeover of experiment station once per semester to minimize the technical effort and re-establishing experimental beam conditions under a different sample environment. The changeover takes typically two weeks of downtime where the swap of the experiment station takes 2-3 days, followed by re-cabling and motor and device test. The change of detector systems (hRIXS spexctrometer, DSSC etc.) takes overall less time. The control systems of XRD and CHEM stations follow a new strategy compared to one of FFT station where the cabling (30-50m routing for each individual cable) goes through patch panels to the rack room above the experiment hutch. The recabling of the FFT station is one of the bottlenecks to shorten the changeover times. The new control systems of XRD and CHEM consists of local Beckhoff terminals which are mounted in a box on the experiment station. The cabling is considerably short, does not need to be unplugged for a changeover and only a few cables connect to the system to overall controls of the beamline and Karabo. The experiment stations can also be operated when not in use at the beamline which is useful for off-line preparations, for example the liquid jet systems.

3.4.1 FFT: solid sample environment for forward scattering geometries

The FFT sample environment serves for fixed-targets manipulation for small-angle x-ray scattering, coherent diffraction imaging, as well as x-ray absorption spectroscopy. The most stringent requirement for the fast sample scanner stage (FSSS) shown in Figure 3.12 on the facing page is given by the destructive single-shot experiments where a pristine sample area is positioned in the beam with each X-ray pulse. In particular for coherent diffraction imaging a positioning accuracy below 3 µm is needed in order to center a 5 µm to 10 µm x-ray beam on holography sample masks.
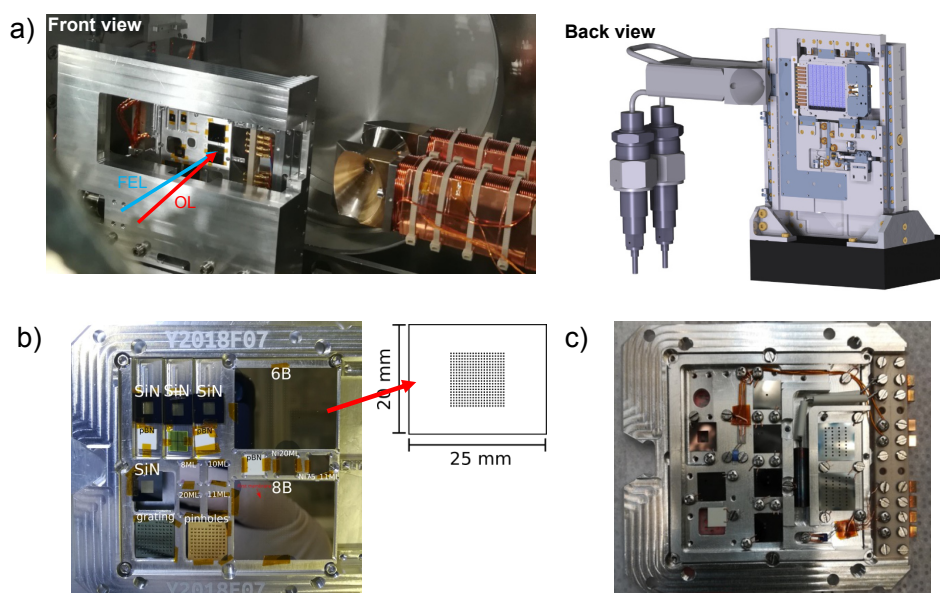
Figure 3.12: Sample environment in FFT. a) Front and back view of the Fast Sample scanner stage (FSSS) with loaded sample frame. The electromagnet is inserted from the side. On the opposite side of the magnet the transfer arm can pick up the sample frames and transfer them to the sample garage. Sample holder examples holding different sizes of membranes arrays b) and diagnostics as well as c) temperature controls via pin-connectors that can be individually arranged for user experiments.

Between 2018 and 2021, developments of the mechanics and the motion control by SEC group and the implementation by EEE group enabled fast sample raster scanning with a speed ranging from 10 µm/s to 60 mm/s with an accuracy of less than 3 µm. Recent single-shot user experiments using high-intensity x-ray or optical laser beams were carried out at 10Hz mode. An example of post-mortem analysis of a Cu film supported by a Ni mesh is shown in Fig. 3.13. The irradiation by two-color FEL (see Section 2.5) was performed while moving the sample horizontally at constant speed. While the spacing between the XFEL shots matches the width of the cells, the relative position was not controlled during this experiment. Hence, sometimes, the pulses were impinging on the mesh (top row). The synchronization of the FSSS with the FEL 10 Hz trigger was successfully implemented for the following beamtime (Cho UP 2437/3216) and enabled a repeatable positioning of the FEL beam with respect to the membrane frame. This allowed a more efficient use of the sample and a proper centering of FEL and optical laser beams, which was necessary for combining the single shot, destructive approach with the XAS-BOZ technique.

For raster scanning of micron-sized holography masks arranged in membranes arrays, the individual sample positions can be located on the sample holder using an optical microscope prior to the experiments. The positions are referenced to four fiducials on
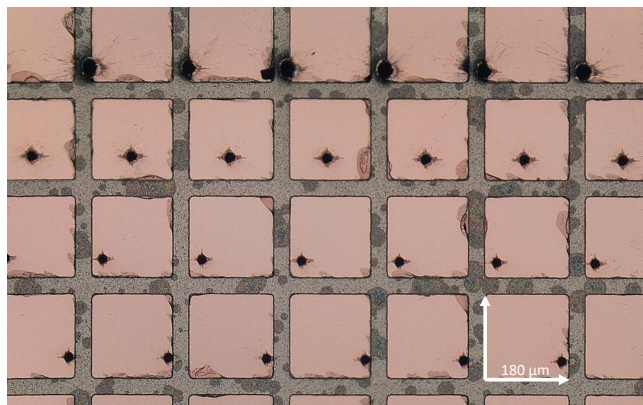
Figure 3.13: Microscope view of XFEL-irradiated 100-nm thick Cu film. The film is supported by a Ni mesh, each individual cell is 180 μm wide.

the sample frame, see Figure 3.15 on page 56. The list of sample positions can be transferred to the user coordinates by locating the four fiducials in the FFT experiment chamber with the X-ray beam. In this way, irregular grid scans with better than 3 μm precision for single-shot CDI are feasible.

The FSSS supports sample frames with a 50mm × 50mm sample area. The sample frames can have different layouts tailored to the type of experiments and user needs. This includes pin-connections for temperature sensors and a sample heater (see Figure 3.12 on the preceding page c)) as well as for connecting an avalanche photodiode to inject subnanosecond electric pulses in wave guides by the femtosecond laser (UP 2858).

The DC electromagnet can be inserted from one side and provides magnetic fields up to 0.35 T with large aperture pole pieces for forward x-ray scattering. Higher fields can be achieved with small apertures pole pieces compatible with BOZ-XAS technique (production is underway). Special magnetic field patterns can be applied and synchronized with the FEL via triggers (see below). The FSSS and the magnet support are mounted on stage translating the sample environment along the x-ray beam direction. This allows for adjusting short sample distances to fixed mounted detectors (DSSC or Pi-MTE3).

Synchronization with the X-ray pulses of multiple devices, e.g. the FSSS, the electromagnet, the train picker, the optical laser shutter, slow read-out detectors (such as the PI-MTE3) can be achieved essentially in two different ways: by conditional triggers or train triggers. Each FEL train is assigned a string of bits, two of which are available to be arbitrarily set in order to define up to four different kind of FEL trains labeled by a corresponding train tag. In this way, depending on the specific
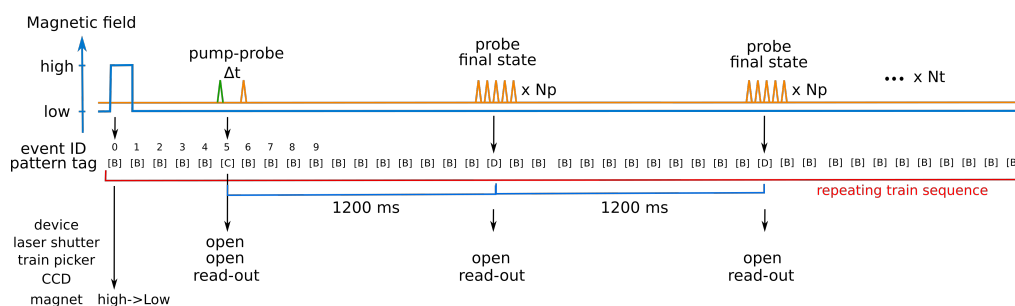
Figure 3.14: Example of multiple devices (shutters, camera, electromagnet) synchronized with different FEL train patterns.

train tag, certain actions, e.g. open/close a shutter, move a motor, start camera acquisition, can be triggered. This so-called conditional trigger approach is robust, but has the disadvantage of providing only four different train tags and, once set up, it cannot be easily changed. On the other hand, the train trigger approach is based on a plc software device which reads the bunch pattern table (containing information on each FEL train) and distributes commands to multiple devices, without any limitations on the number of conditions. It is compatible with a periodic sequence of FEL trains, as well as with a list of specific train numbers. The other advantages of this approach are that it is relatively easy to implement and to modify depending on experimental needs. Fig. 3.14 shows an example of three different train pattern tags and corresponding device states implemented for UP2858. In this case, both conditional triggers and train triggers implementations were successfully tested. At event id 0, the electromagnet was set to a high value to saturate a magnetic sample and then set back to a lower value. FEL train [C] corresponds to the pump-probe event, hence both laser shutter and train picker are open and camera acquisition is triggered. During the readout, train picker and laser shutter remain closed. Next, multiple FEL trains, consisting of many FEL pulses (pattern [D]), are used to probe the final state. This train sequences is then repeated to accumulate statistics.

A sample garage located opposite to the magnet can store up to 8 sample holders which can be transferred to the FSSS without venting the FFT chamber.

A commercial liquid helium flow cryostat (Janis ST-400) can be installed on top of the FFT chamber to facilitate experiments at cryogenic temperatures. The cryostat is mounted on a UHV manipulator with four degrees of motion (linear x, y, z and rotation about the vertical axis). Sample holders can be fabricated at short notice to accommodate User samples, different incidence and scattering geometries and sample heating. Out-of-plane magnetic fields can be applied with the electromagnet. In-plane fields from permanent magnets mounted on the FSSS x/z travel are planned.
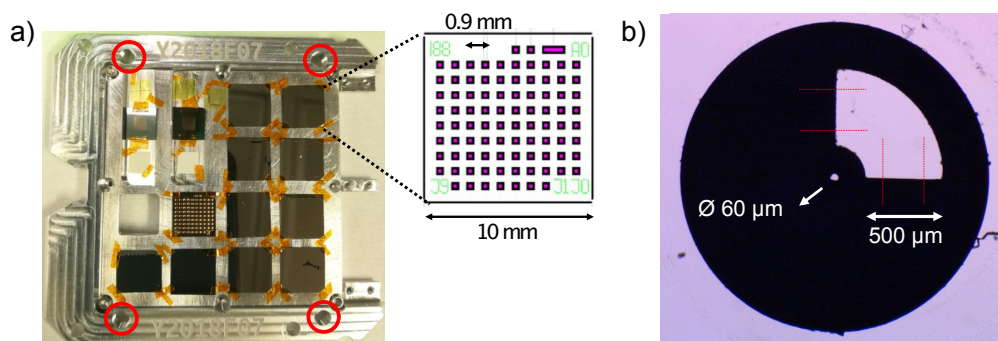
Figure 3.15: Sample fiducials. a) Four sample holder fiducials serve as references (red circles). They define the positions of the individual sample positions on the frame measured under a microscope prior to the experiment. b) Enlarged view of the fiducial. Sample positions in the experiment coordinates on the sample scanner in the FFT experiment station are derived from knife edge scans along the dashed red lines.

First experiments with the setup reached 15K at the sample position with very modest He consumption. A design using a cryostat with the correct length and appropriate shielding should allow lower temperatures. We plan to purchase a closed circuit helium gas cooler to reduce the cost and waste of using He without a recovery line.

Work is also underway to connect the FSSS to an external cryostat aiming at LN_2 temperature using copper braid to conduct heat, as is done in the XRD chamber. The ultimate temperature is unknown at this time, but it will allow for larger samples than can be used on the cryostat and sample exchange under vacuum, while retaining the large travel range of the FSSS.

3.4.2   CHEM: liquid jet sample environment

In this section we present the CHEM chamber at SCS which provides a dedicated vacuum environment for neat liquid and solution phase samples. It is designed to be coupled with the hRIXS spectrometer, and thus, enables ultrafast RIXS spectroscopy to be performed on liquids. The technical drawing of the CHEM is shown in 3.16. A differential pumping section separates the UHV environment of the beamline from the liquid jet environment of the main sample chamber. The main sample chamber contains a standard UHV manipulator with three translational degrees of freedom as well as rotation around the vertical axis. A downstream diagnostic chamber contains photodiodes and fluorescent screens that allow for jet monitoring and knife-edge scans to characterize the X-ray beam and liquid jet. Laser in-coupling is facilitated by a vacuum cross containing a mirror for a co-linear laser–x-ray interaction and a breadboard for mounting optical elements.
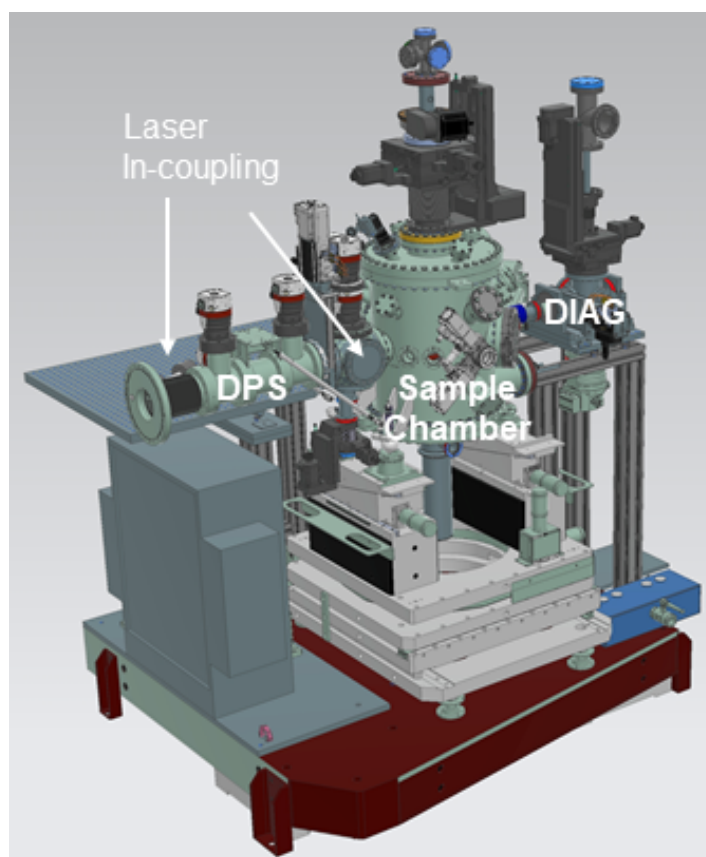
Figure 3.16: Technical drawing showing components of the CHEM chamber.

Holders for various liquid jets may be mounted on this manipulator. The liquid jet holder also provides areas for mounting diagnostic samples for timing measurements, fluorescent screens for optimization of spatial overlap of X-ray and optical beams, and solid reference samples for spectrometer optimization.

Table 3.2: Jet parameters currently available at SCS.

Solvents	Water	Ethanol	Iso-propanol
Nozzle orifice size [μm]	20 – 50		
Flowrate [ml/mm]	0.5 – 5		
Repetition rate [Hz]	from 113 kHz	up to 1.1 MHz	
RIXS scattering angle [°]	35	55	90
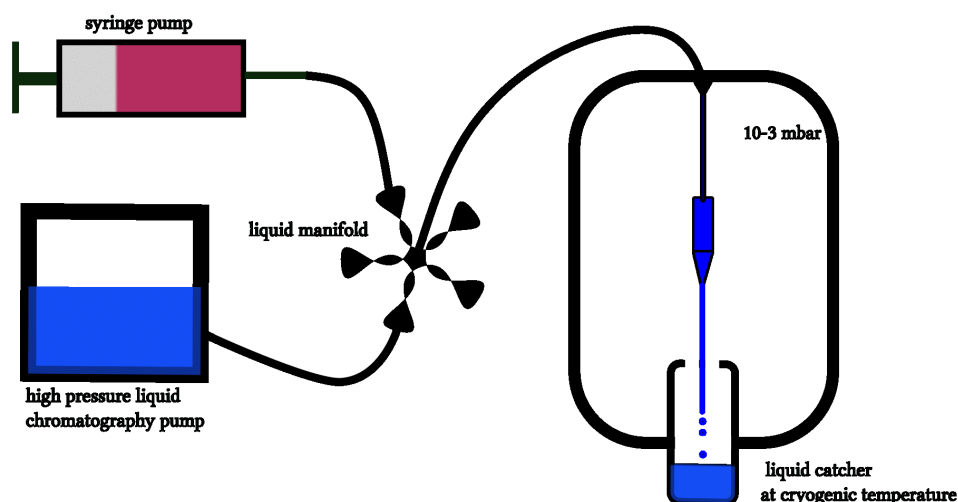
Figure 3.17: Schematic of the current liquid delivery system.

The schematic of standard liquid jet operation is shown in 3.17 and the typical liquid jet operation parameters are given in 3.2. The various liquid samples can be chosen from the switcher and is guided through an internal degaser system of the HPLC (Shimadzu) pump into the interaction point. The CHEM chamber is equipped with two cold traps, one positioned below and another one on the side of the jet. Both cold traps and a HiPace 2300 turbo pump from Pfeiffer ensures a vacuum level of around 10^{-4} - 10^{-3} mbar with a running jet. A three stage differential pumping stage (DPS) with an aperture of around 5 mm for each stage allows to overcome the pressure difference between the experimental chamber and the beamline and maintains the level even in case the turbo pumps fails. The usual liquid jet operation parameters are with a nozzle orifice of around 35 μm, a flow rate of 2.5 ml/min. Considering the laser spot size of around 100 μm, a 500 kHz repetition of renewable sample is feasible. The cold trap below the jet has a volume of about 4l, which allows for a continuous 24 h operation of the jet before it is replaced with an empty one.

Two digital microscopes are installed on the Chem chamber to observe the stability the jet. One provides an overview image of the jet from and its holder. Fluorescence caused by the FEL can be seen on the jet during MHz operation mode as shown in 3.18. The second microscope views a fluorescent screen downstream from the sample where a the shadow of the jet can be used to monitor the jet position relative to the center of the X-ray beam.
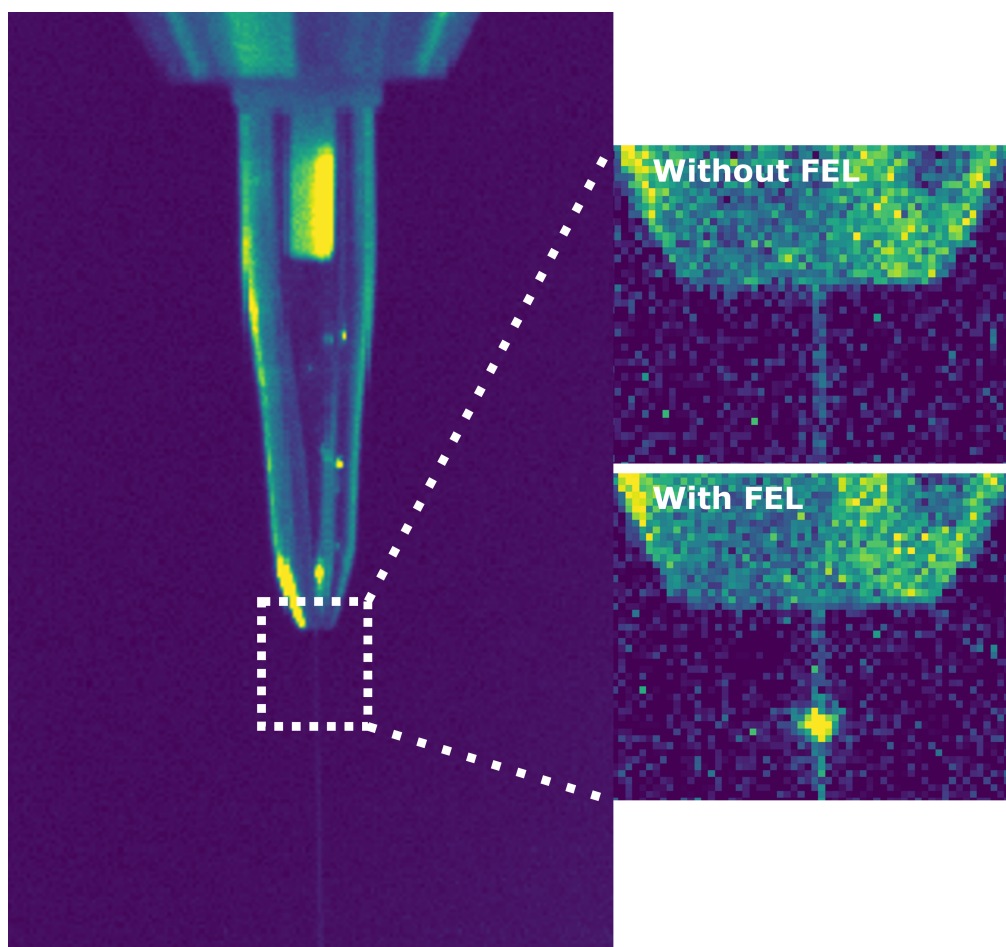
Figure 3.18: The liquid jet during operation in the Chem chamber and zoomed-in view of the jet with and without FEL overlap observed from one of the two digital microscopes. The FEL beam generates optical fluorescence from a 10 mM bio-molecular sample dissolved in ethanol.

3.4.3   XRD: X-ray diffraction and momentum-resolved RIXS

For the solid-sample environment the SCS baseline XRD chamber will be used. The XRD chamber offers ultra-high vacuum (UHV) and cryogenic sample environment for x-ray resonant diffraction studies. It has been designed for compatibility with the hRIXS spectrometer.

Figure 3.19 shows an overview of the XRD chamber. The core-piece of the XRD vessel is the triple-rotating flange (TRF), which is the connecting flange for the hRIXS spectrometer. The TRF consists of three flanges, each one connected to a rotary feedthrough. Through a combined motion of the feedthroughs the connecting flange can move in the horizontal plane by about 90 deg, which allows a continuous variation of the scattering angle. Besides the hRIXS spectrometer, the flange can be also used
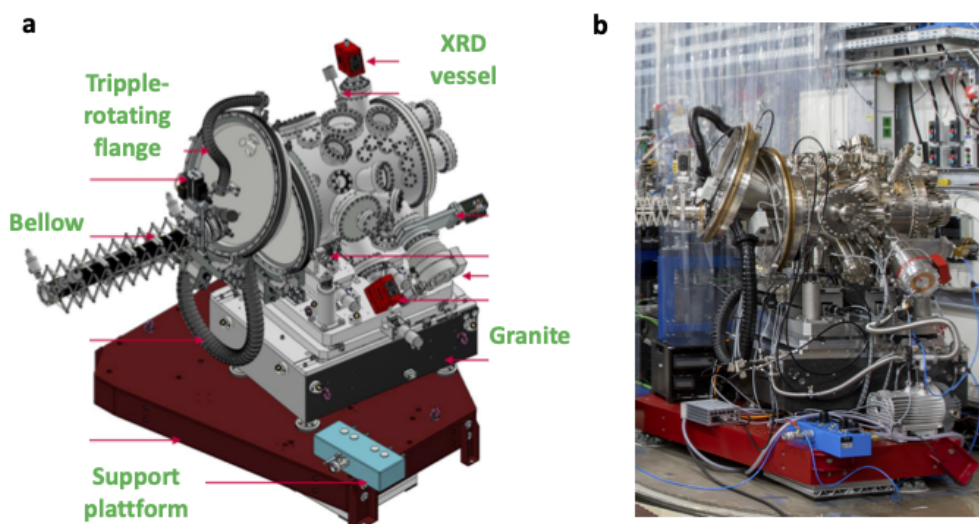
Figure 3.19: XRD experiment station.

to connect a 2D detector. The XRD setup can be moved away from the interaction point using air-cushions placed below the support platform. The vessel and the inner mechanics are supported by a granite, which ensures good thermal and mechanical stability.

The inner mechanics consists of a diffractometer, sample stage and a breadboard (see Figure 3.20). These pieces form one entity supported by the granite block, making the entire structure very stable. The diffractometer provides three degrees of motion, two for the sample stage and one for the detector circle. The sample stage is placed inside the diffractometer, on top of the two sample degrees of rotation and it provides another four degrees of motion for the sample (the three translations and one rotation). Therefore, the diffractometer and the sample stage provide in total 6 degrees of motion for the sample. The movement range is listed in the table below. The sample stage is connected to a cryostat through Cu-braids. The specified temperature range for the sample is between 20 K and room temperature. The detector circle will be used to mount mainly photodiodes and APDs. These detectors will be used to measure X-ray diffraction from the sample, optical laser beam reflected from the sample, as well as diagnostic tools for knife edge scans and temporal overlap of FEL and optical laser. The breadboard can be used to mount additional equipment for experiments at XRD, e.g. MCP for XAS measurements in fluorescence. The breadbord will also host the support for THz laser incoupling mirror for pump-probe experiments.
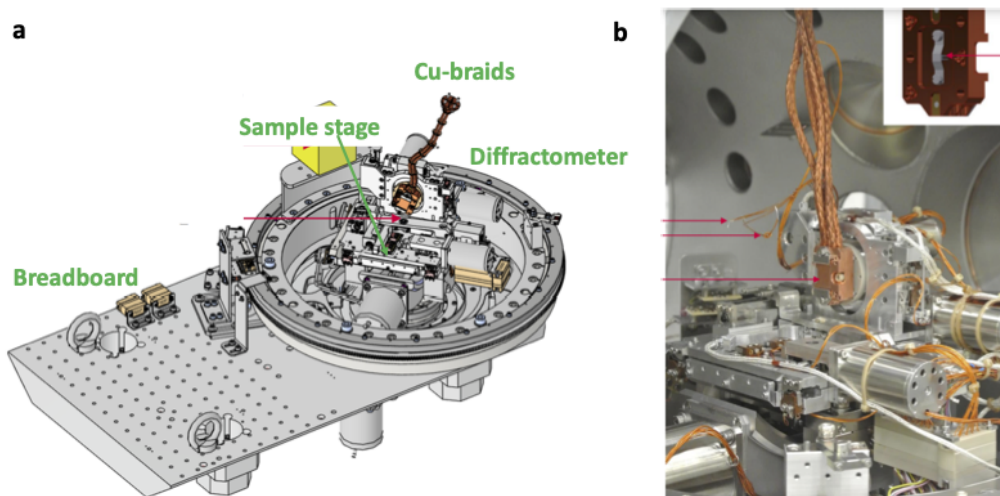
Figure 3.20: XRD inner mechanics.

Table 3.3: Motion ranges for XRD inner mechanics.

Description	Range	Repeatability	Notes
Theta	+/−180 deg	< 0.002 deg	Sample incidence angle
Kappa	+/−30 deg	< 0.002 deg	Sample Tilt
Azimuth	+/−90 deg	< 0.1 deg	Sample rotation around the beam
TX, TY, TZ	+/−5 mm	< 5 μm	Sample translation along X, Y, Z
Two Theta	+/−180 deg	< 0.002 deg	Detector scattering angle

3.5 Detectors in operation

3.5.1 DSSC

The first DSSC (DEPFET Sensor with Signal Compression) 1-megapixel camera (Figure 3.21 on the next page a) became available in February 2019 [58]. After technical integration and commissioning at the SCS Instrument the DSSC was ready for first two experiments in May 2019 which let to the first SCS user publication by Büttner et al. [10]. DSSC is a high-speed, large-area, 2-D imaging detector system optimized for photon science applications in the energy range between 0.25 keV to 6 keV. The DSSC is essential for all time-resolved SAXS, BOZ-XAS and more recently, X-ray photon correlation spectroscopy (XPCS) studies at the SCS Instrument.

The camera is based on direct conversion Si-sensors and is composed of 1024×1024 pixels of hexagonal shape with a side length of 136 μm. 256 ASICs provide full parallel readout, comprising analog filtering, digitization and in-pixel data storage of up to 800 frames. To cope with the demanding X-ray pulse time structure of the European XFEL, the DSSC provides a peak frame rate of 4.5 MHz. This first version of megapixel DSSC camera is equipped with Miniaturized Silicon Drift Detector (MiniSDD) pixel arrays instead of DEPFET. The intrinsic response of the pixels and the linear readout limit the dynamic range but allow one to achieve noise values of about 60 electrons r.m.s. at the highest frame rate. The MiniSDD-equipped DSSC provides single photon sensitivity only for photon energies above 1.0 keV which limits the attainable SNR at low photon yields below 1.0 keV where important absorption resonances for magnetic material are located (Figure 3.3 on page 37). In particular coherent diffraction imaging of magnetic nanostructure dynamics would benefit from a DEPFET upgrade of the DSSC as the current configuration will limit the attainable spatial resolution due to noise at high momentum transfer (Section 2.3 on page 25).[31]

The DSSC detector is divided in 4 quadrants which can be moved in a windmill configuration to enlarge or reduce the size of the central hole. However, this quadrant motion is in practice not used at SCS for the following two reasons. First reason is that the DSSC sensors are only coated by a thin layer of 30 nm aluminum, which is insufficient to block the optical laser light and thus deteriorating the data quality due to laser background. To make the DSSC detector ready for laser-driven experiments at the SCS Instrument, a large Al filter (150 nm) is installed in front of the DSSC to block the visible light from the optical laser, see Figure 3.21 c). The support frame of the Al filter shields permanently part of the detector from photons with the smallest
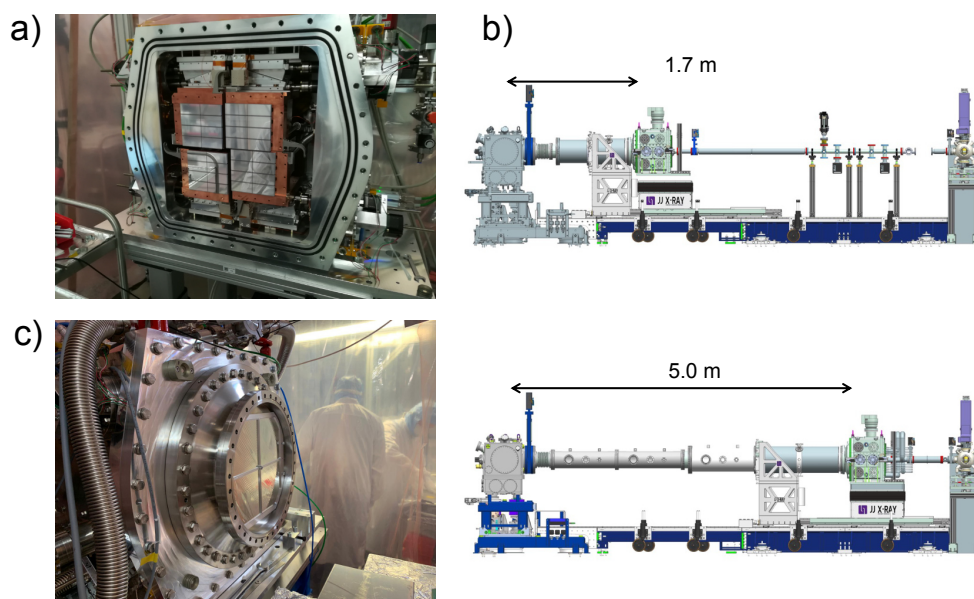
Figure 3.21: a: DSSC quandrants. b: examples of two possible DSSC configurations, with the corresponding sample-detector distance. c: Al filter installed in front of DSSC quandrants.

loss of detector area when the quadrants are closed down to the minimum gap size (default configuration), see Figure 3.22 e). Removal of this filter is both a tedious and a risky operation and is performed rarely when it is absolutely necessary. The second reason is that the quadrants movement is not fully risk-free in terms of collision due to the complex mechanics of the motion system and the use of relative encoders. Therefore the DSSC detector motion system has been only commissioned at the SQS Instrument of the EuXFEL, but not yet at SCS as the advantages do not obviously exceed the risks.

The DSSC detector is mounted on a detector stage which can be moved under vacuum forces over a range of 1.5 m along the beam direction on a carrier. The carrier itself can be positioned at near, mid and far distance to the FFT experiment station. The sample-detector distance can range from 1.2 m to 5.4 m covering a wide range of momentum transfer over the photon energy range of SCS.

In terms of detector operation, safe power-on/-off procedure are implemented. Protection of the detector hardware is given by an interlock system monitoring vacuum or cooling failures, or internal detector issues. This interlock shuts down the detector in case of danger for the hardware and prohibits switching it on if the environment and the infrastructure around the detector are not correctly configured or not ready (low vacuum, cooler not running, temperature too high, etc.).
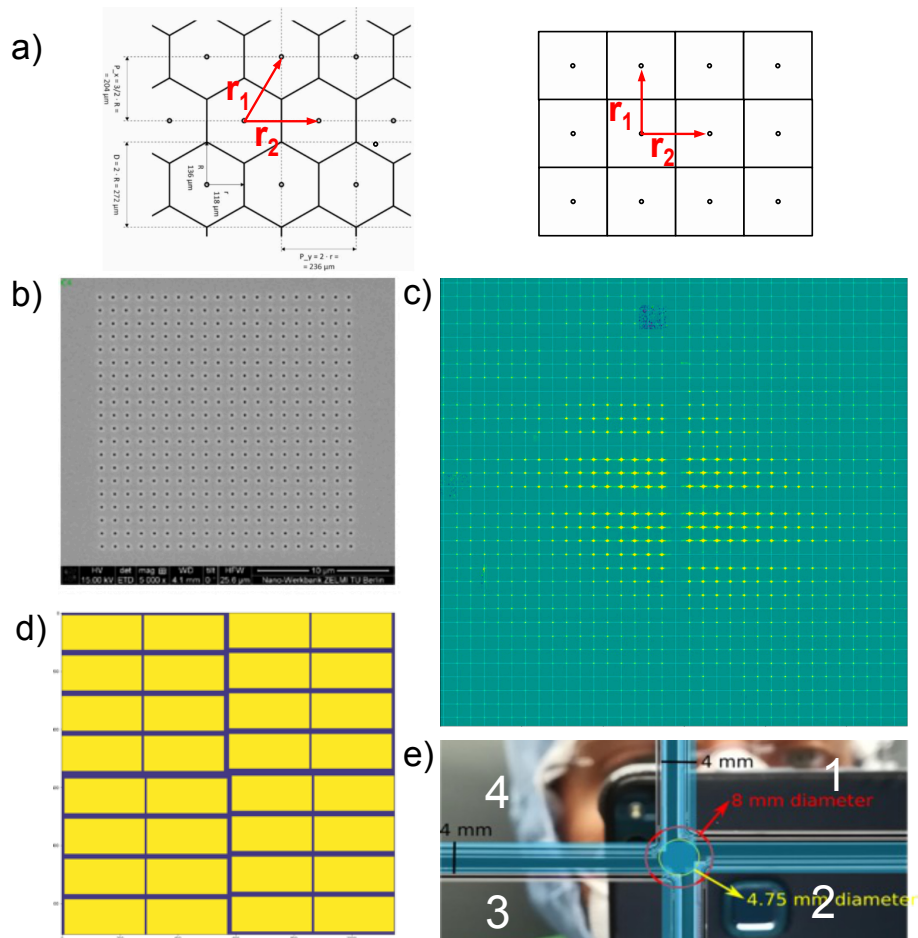
Figure 3.22: a: hexagonal arrangement of DSSC pixels. b: SEM image of a regular array of pinholes. c: corresponding DSSC image resulting from diffraction through the pinholes. d: scheme of windmill configuration of DSSC quadrants. e: picture of DSSC center, with dimensions of minimum central hole and dead areas in between quadrants.

The DSSC detector can record a maximum of 800 frames per train. A veto system allows for selecting the frames to be recorded in the DAQ. The detector usually operates at a frame rate of 4.5 MHz, and the veto system is used to reduce the frame rate down to few tens of kHz as needed by the experiment, see for example Figure 3.23 a). In the past, there have been some issues in properly configuring the veto pattern leading to some loss of beamtime. To improve this situation, a new control device has been developed and implemented to visualize the FEL X-ray pattern, the pump laser pattern and the DSSC recording pattern to make sure they match as expected.

Calibration of the DSSC detector is performed with hard X-rays (requires photon

energies higher than 8 keV) and therefore cannot be performed at the SCS Instrument. Two calibration campaigns took place using a pulsed X-ray source to characterize the detector. From these collected data, a software package was developed allowing for creation of gain configuration files for the detector which are tailored to the use case of the experiment in a matter of minutes. By changing gain configuration, DSSC detector can cover a wide range of photon energies as well as number of collected photons.[58] In principle, the DSSC gain can be configured at the pixel level. The extension to different gain configuration for different pixels is under way (example for scattering experiments: a low gain configuration around the center and high gain configuration at the perimeter of the detector). Further the repetition rate of the detector can be reduced from 4.5 MHz to 2.25 MHz, allowing for 9 bits digitization instead of 8 bits which increases the dynamic range of the detector. The pixel integration time can in addition be extended where preliminary results show a reduction of the pixel noise. Configuring the DSSC for 1.1 MHz operation with even longer integration window is further possible.

The individual DSSC raw data of the 16 ladders (four ladders per quadrant) require their positioning in a composite 2D data array of the full detector. The individual quadrants and ladders are not positioned on the hexagonal grid of the detector pixels. Therefore it makes sense at this point to transfer the position of ladders in Cartesian coordinates to the full detector map, see Figure 3.22 on the facing page. The hexagonal to Cartesian coordinate transformation is performed by three shear operations [12] of the sixteen ladder data arrays before patching them in the composite pixel map. The grid conversion scheme involves fast and reversible 1D fractional delay operators which can be parallelized line by line to apply three successive shear operations on the 2D data array of the ladders. The hexagonal-to-cartesian conversion is currently implemented in the extra-geom python package for the DSSC detector by the data analysis group.[19]

To find the positions of the ladders, an X-ray diffraction pattern from a 20x20x100 nm pinhole array is recorded, see Figure 3.22 on the preceding page. The individual ladders are then fitted to the reciprocal lattice. When the quadrants are moved to change the center hole of the DSSC detector, the positions of the four quadrants have to be updated in the geometry file of the DSSC detector.

The DSSC produced high data quality from the start of user operation at SCS leading to early user publications [10; 74]. Several manuscripts are currently under review and more mansucripts are in preparation. As scientific data of this new kind of detector were acquired and analyzed for the first time, some issues and possible improvements in data collection become apparent. For example, some of the data sent by individual ASICs would fluctuate and flicker after a gain configuration. After
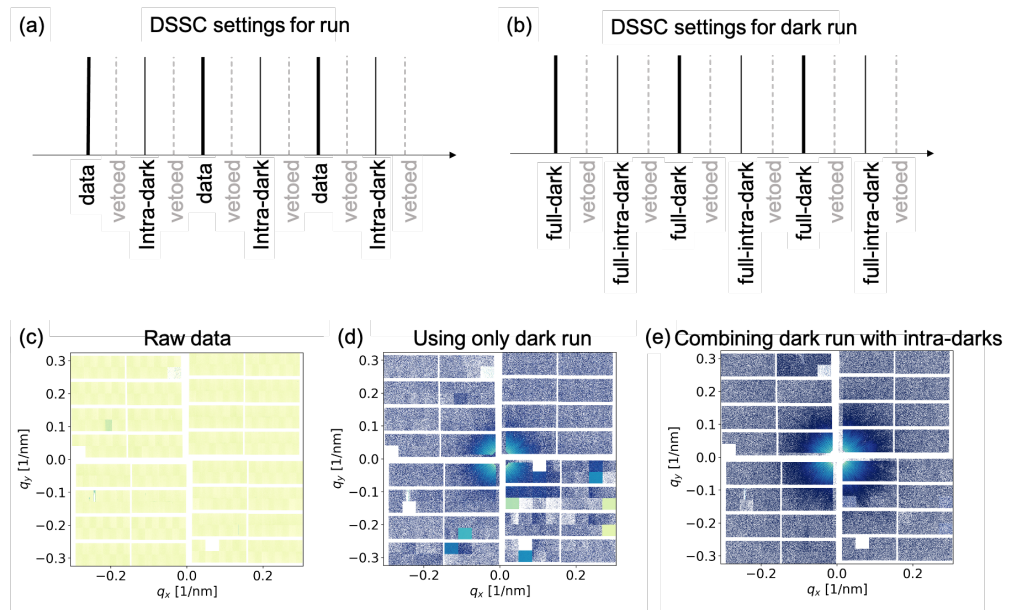
Figure 3.23: Schematic of the DSSC pulse selection settings for data recording (a) data acquisition with alternating XFEL and intra-dark frames and (b), same pattern as (a), separate dark run recorded without x-ray exposures. (c) Raw data collected by the DSSC detector plotted around its mean value. (d) Dark subtraction using only a separate dark run and (e) dark subtraction combining a separate dark run and the intra-dark events. Details are reported in [31]

investigations it was determined that a wrongly configured clock signal was the cause of this issue which was eventually solved by a firmware update. This is a problem that affected some of the early user experiments [31]. In the very low photon count regime, some level instabilities of the sensor basis was reported by Users which could be mitigated by the recording of so-called 'intra-darks', which are dark frames collected between two X-ray illuminated frames of a train as shown in Figure 3.23 and detailed in [31]. This improves the situation without completely solving it. Further attempts at applying additional corrections, such as subtracting the median value of dark pixel for the whole sensor, leads to some improvement while still resulting in data which are much noisier than on stable sensors. Some other effects have been reported such as a larger than expected differential non-linearity, baseline change with intensity per ASICs, and an amount of integral non-linearity of the order of 1 % at most. The latter is within expectation and can be corrected for certain class of experiment such as X-ray absorption spectroscopy, see Section 2.1.2 on page 18 and [29]. To understand and to correct these effects better, it is foreseen to invest resources in the future .

The detector operated flawlessly over the past years. Only recently, it was discovered

that the double wall cooling pipes transporting in-situ the coolant to the individual quadrants, are significantly deformed. The pipes were checked for vacuum and cooling leaks and found tight. At the time of this report, The source of the deformation is unknown and it is unclear if the deformation poses a risk for the detector operation. The DSSC remains unavailable for experiments until investigations are done and safe operation of the DSSC is guaranteed.

3.5.2   hRIXS Spectrometer

There are two optical elements inside the hRIXS spectrometer – the grating and the detector. This is the minimum number of elements required for adjustment of a spherical VLS grating spectrometer. Since the spectrometer had to be easily adjustable (as it is used with different experimental setups and there is little time for optimization), a collecting mirror was not foreseen. In order to align the spectrometer for one photon energy four degrees of freedom are required: the incidence angle on the grating, the entrance arm length, the exit angle and the exit arm length. These are realized by these four motions: grating pitch angle (changing the incidence angle), the horizontal translation of the grating chamber (changing the distance from the grating to the focus), the horizontal translation of the detector chamber and the vertical translation of the detector chamber (both changing the distance between the grating and the detector and the exit angle), see Figure 3.24a. The required movement range for the translation of the two chambers is large, to allow operating the spectrometer over a large photon energy range with one grating. At the same time the stability requirements are very high.

The model of the spectrometer is shown in Figure 3.24b. The bottom part consists of a large mineral casting base, to ensure very good thermal and mechanical stability. The grating chamber has an additional mineral casting support, which also holds the inner mechanics. The detector chamber is held by a lifting unit made out of steal. The spectrometer is placed on air pads, which allows displacing it. When the spectrometer is placed at the interaction point, the rails inside the experimental floor guide rotation of the spectrometer. When not in use, the spectrometer can be detached and placed in a parking position, away from the interaction point. The weight of the spectrometer is approximately 10 t and the dimensions approximately 4.2 m x 2.1 m x 3.1 m (L x W x H). Figure 3.25 shows a photograph of the hRIXS spectrometer, when connected to the interaction point.

There is no need for an entrance slit for the hRIXS spectrometer, due to the small vertical x-ray spot size at SCS Instrument. There is a mask unit, placed in front of the grating, which gives the possibility to narrow down grating illumination. The inner
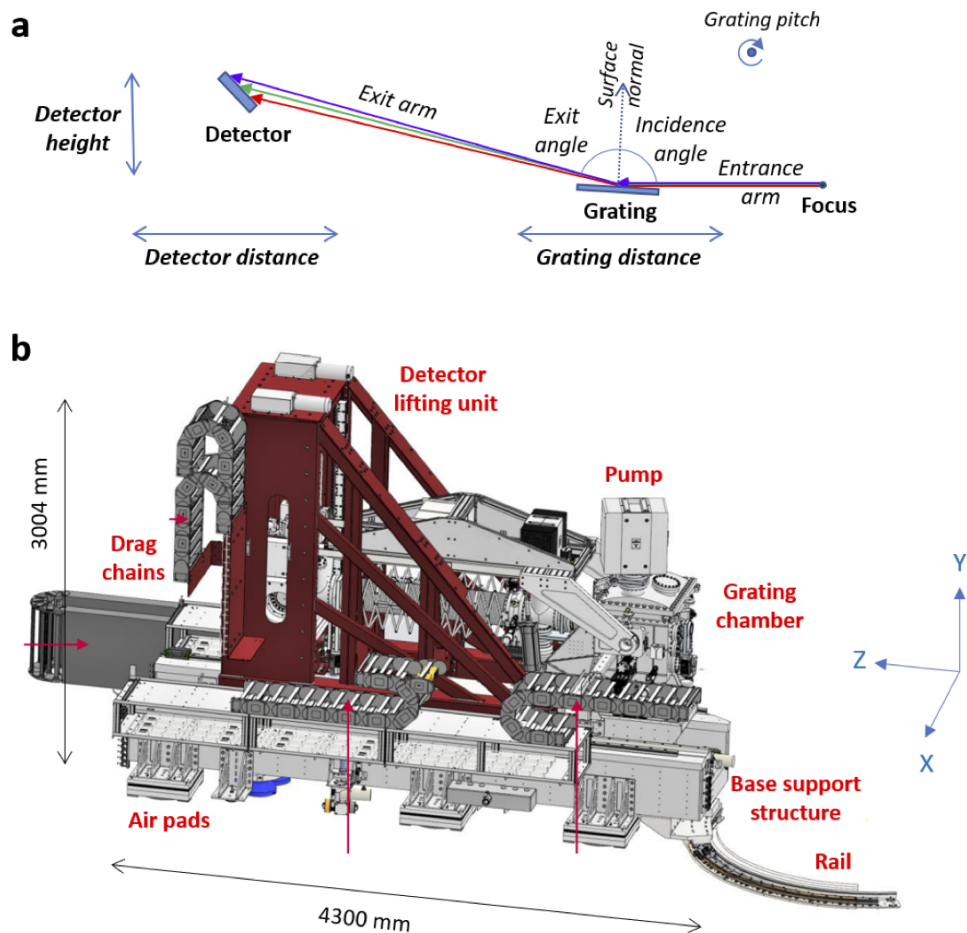
Figure 3.24: hRIXS Layout. **a** Optical layout of hRIXS spectrometer showing the four adjustable degrees of freedom. **b** Technical model of hRIXS spectrometer.

mechanics of the grating chamber provides space for three gratings. Exchange of gratings is realized by a horizontal transverse motion. There are additional degrees of motion for grating alignment. Behind the grating tank there is an aperture unit with four independent aperture blades that can be potentially used to shield stray light falling on the detector. The detector chamber is optimized for holding large detectors. The detector mounting flange has the size of 300 DN and is tilted at 25° to the exit arm. In order to keep the incidence angle fixed at the detector and also to prevent the large bellow between connecting the grating chamber with the detector chamber from breaking, the detector chamber needs to be rotated when changing the detector position.

Detection of RIXS spectra from the spectrometer has been done with multiple detectors. For the initial commissioning, we utilized a liquid nitrogen cooled Princeton Instruments (PI) X-ray CCD detector. Second, we utilized a water-cooled PI-MTE3
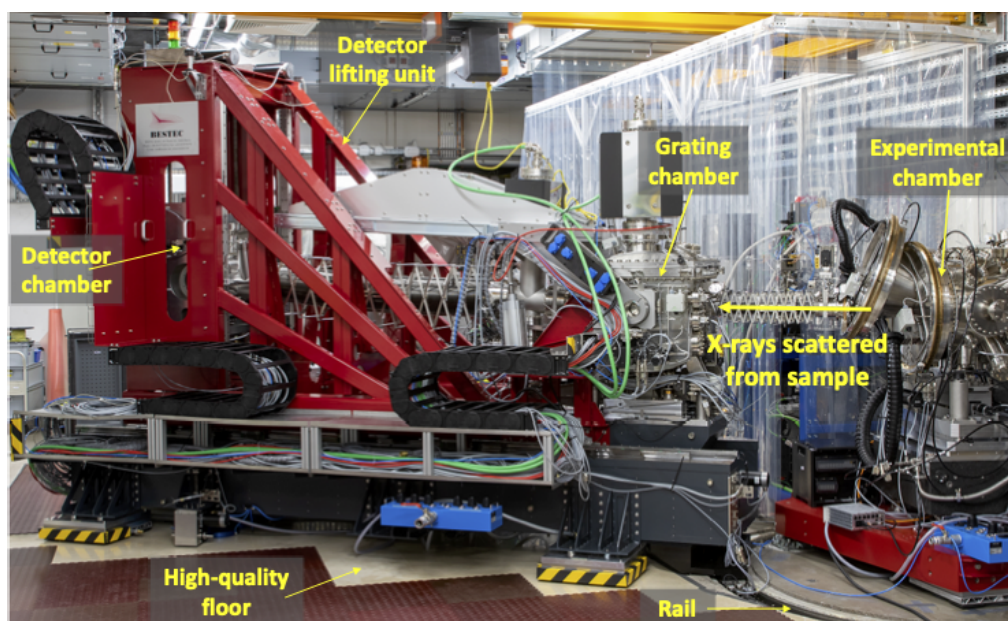
Figure 3.25: hRIXS spectrometer in experiment hutch viewed together with the XRD experimental chamber.

CCD. The major difference about the detector function is the readout times used in our measurements. The LN2 cooled camera used a kHz readout mode with a 40 s readout time. The PI-MTE3 has been utilized MHz readout mode with a 4 s readout time and has advantages for time-resolved measurements.

For all experiments, a 2D camera image is collected. The signal is dispersed in the vertical direction on the camera sensor. The signal then needs to be summed in the horizontal direction to generate individual "RIXS intensity" vs. "emission energy" (or "energy loss") spectra. Image processing takes place in several steps depicted in Figure 3.26. Firstly the image is curvature corrected. This resolves any imperfections in the mounting of the camera and assures that summation of iso-electronic counts. Secondly, all counts are summed along the horizontal direction of the camera.Proper curvature correction is necesarry to generate a sharp elastic scattering feature. A data acquisition "run" is the sum of all detector readouts over a fixed time.

The concepts behind measuring time-resolved spectra from the RIXS spectrometer rely on a realization that available area detectors do not have the time resolution to resolve the individual X-ray pulses generated at XFEL. Therefore we measure photo-excited samples over many trains/pulses and compare the signal to that of samples that have not been photo-excited. This differs from many pump-probe detection schemes using pulse-resolved detection that compare laser off and laser on pulse pairs.
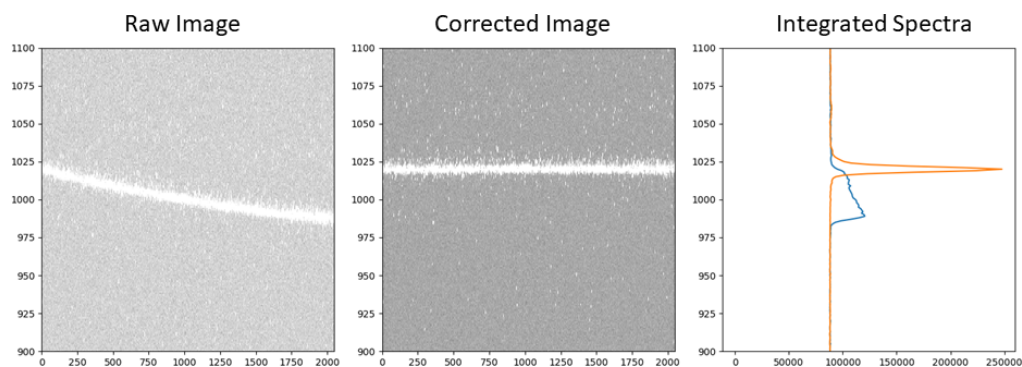
Figure 3.26: Depiction of processing of RIXS data. Raw data (left) is curvature corrected to generate a new image (center). Spectra (right) with (orange curve) and without (blue curve) curvature correction.

During the first X-ray commissioning measurements, all experiments were performed on solid samples in the UHV-mode ($10^{-8}\,mbar$) of the Chem chamber. The LN2 cooled camera was used with either 5 or 10 min acquisition times. The total signal was then For time-resolved measurements were performed with the PI-MTE3 CCD using MHz readout mode. In this case, images were typically acquired for 20 or 30 seconds, and photon-counting combined with centroiding was used to increase the detector resolution. The optical delay line can be moved during camera readout (4 s), which allows the measurement of delay traces for single incident energies. Including both positive and negative delays times provides spectra of pumped and un-pumped states of the system.

3.5.3   Commercial CCD detector

For imaging experiments, Fourier-transform holography is a key technique able to reveal nm-sized objects in real space with magnetic contrast and it is well suited to SCS capabilities, in particular once circularly polarized light will be available. For a proper image reconstruction a low-noise detector with high dynamic range and gap-less sensitive area is required. In addition, to be able to cover different q ranges, the detector should be fully in-vacuum with a tunable distance to the sample. The answer to all these requirements is given by the commercial PI-MTE3 CCD camera provided by Teledyne Princeton Instrments. The sensitive area is 30.7 mm x 30.7 mm with $2048x2048$ 15 µm pixels. With a readout noise of 9 electrons rms and 4 parallel readout ports is possible to record at a repetition rate close to 1 Hz (1 frame every 1.1 s) without binning. This detector configuration was already used for the first recent holography experiment at SCS. The number of frames per second can be increased to 3 if a 3 times larger readout noise can be accepted, while gaining a factor of 2

better readout noise costs 10 times longer acquisition time. The sample-detector distance can be varied in vacuum between 55 mm and 830 mm, providing e.g. at the Co edge a maximum q vector of $1\,nm^{-1}$. This detector has been employed for one user experiment in FFT chamber aiming to perform time-resolved Fourier-transform holography and has been used for all hRIXS experiments. Because of the long readout time, of the order of seconds for the typical use cases at SCS, FEL pulses should be prevented from reaching the detector during readout. This is achieved by the synchronization with the so-called train-picker, i.e. a piezo-motor driven shutter (installed in SASA3 tunnel after the exist slits) which closes during detector readout and opens only for a variable number of FEL trains corresponding to the detector exposure time.

3.5.4   Micro-channel plates

The SCS Instrument makes use of point detectors which must both be sensitive to detect rare events and also possess high time-resolution for pulse-resolved detection. UHV setups make use of micro-channel plate detector (MCP) assemblies for this purpose, and have been employed for a number of applications. An MCP detector functions as an I_0 monitor for MCD experiments that utilize our thin-film polarizer component. They are used as fluorescence detectors in FFT and Chem, and they are the detectors used for the transmission intensity monitor (TIM) used in UP2384 Thielemann-Kühn. The TIM consists of a CVD diamond screen and the fluorescence from the screen is monitored in a pulse-resolved fashion.

To date we have utilized MCP assemblies from Surface Concept (www.surface-concept.com) and Hamamatsu (www.hamamatsu.com). The Surface Concept MCP detectors are flange mounted and use a chevron configuration of two MPC plates. There are four HV connections to control the potentials of various parts of the assembly. The front face of the MCP is set to 0 V, and the back face is ramped to a positive voltage typically between 1,600 and 2,100 V. Charges accelerated through the plate are collected on an anode set to 400 V greater than the potential difference between the front and back faces of the MCP stack. The MCP face is shielded from photo-electrons by a wire mesh that is set to a voltage of -3,000 V. These detectors are used in the TIM. The second MCP assembly from Hamamatsu has only a single negatively-biased HV connection which is applied to the front face of the MCP. Therefore the MCP face itself performs ion-rejection. The potential differences between the front face and the back face of the MCP and the anode are generated by a series of resisters. These MCPs are compact and can be flexibly positioned on breadboards within experimental chambers. They have been utilized as fluorescence detectors in the FFT and CHEM chambers. In both cases the

signals from the MCP are read out via an SMA connection and fed into a fast digitizer.
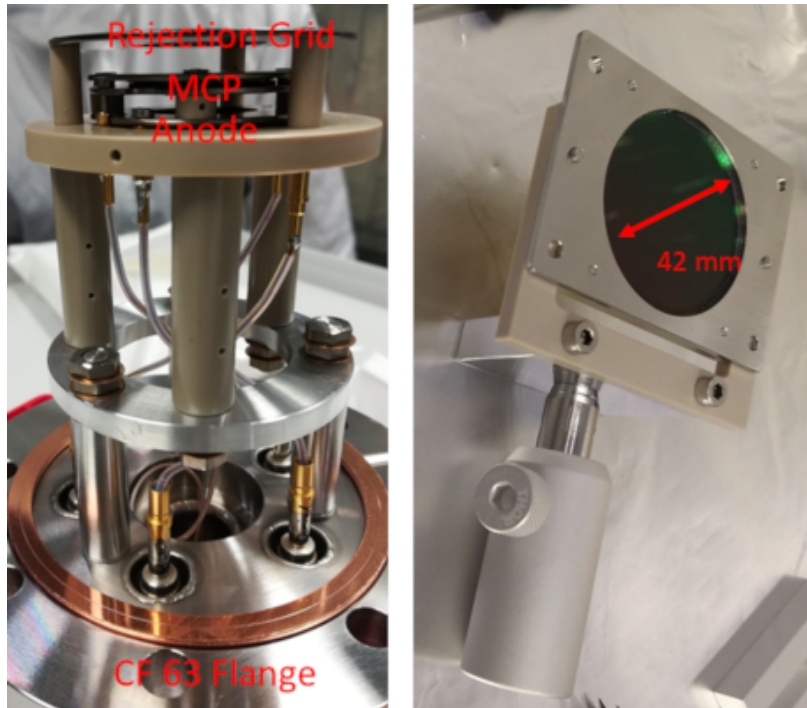
Figure 3.27: (left) Surface Concept flange-mounted MCP assembly.(Right) Large active area MCP from Hamamatsu including home-built mount.

3.6 Online and offline analysis

With such complex instrumentation and expensive beamtime, it is essential to quickly access the quality of the recorded data. The first stage is enabled by online analysis providing live views of raw and analyzed data. Here, there is often a trade-off between usability and flexibility.[16] On the flexibility side, we will find, for example, programmatic interface which allow a User to write its own analysis procedure. This of course requires some initial work by the Users in writing code and testing it but is completely flexible in terms of analysis. On the other hand, specific general purpose code can be combined with a graphical user interface (GUI) in a monolithic package which are then extremely easy to use, as no programming from the Users are required, at the cost of flexibility. Depending on the situation, different trade-off are desired and different options are available. The Karabo control system provides a GUI and scripting with macros which allows a first level of online data analysis. One
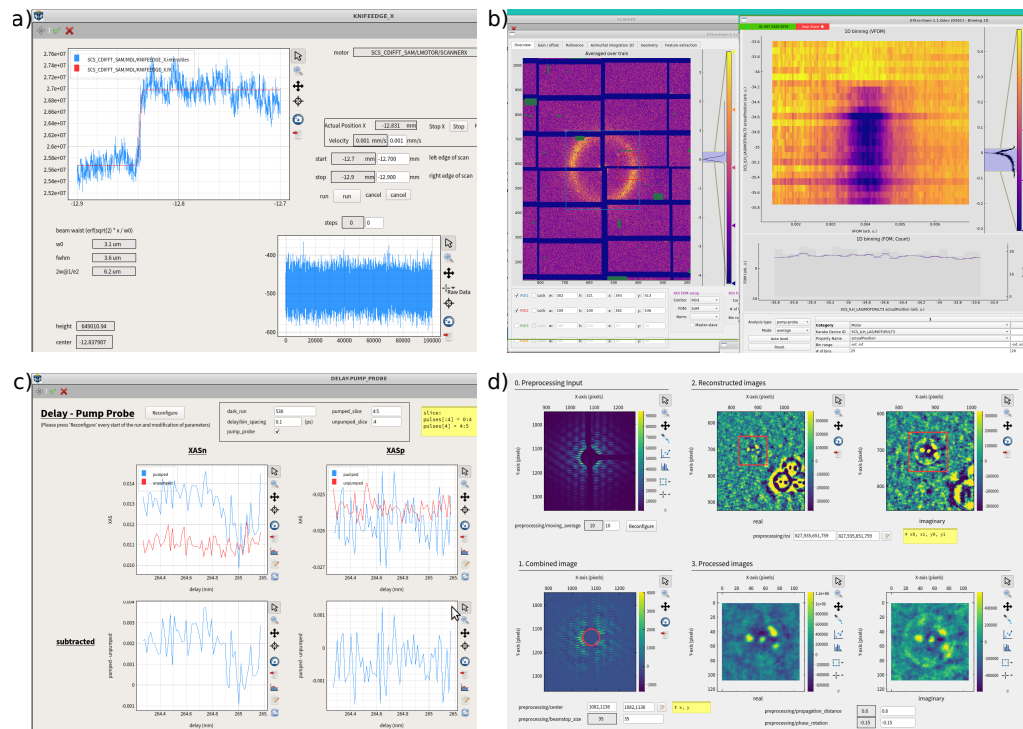
Figure 3.28: a) Online analysis with Karabo of a knife-edge scan. b) EXtra-foam online analysis of magnetic scattering. Azimuthal integration is performed and the difference between pumped and unpumped data are binned versus time delay, showing the decrease in magnetic scattering after optical pump. c) BOZ XAS analysis of time delay scan with extra-metro with the output embedded in a karabo scene. The XASn is for the beam sampling the excited sample, displaying a clear difference between pumped frame and unpumped frame as function of time delay. d) An example of live holography reconstruction performed with extra-metro on data recorded with the PI-MTE3 camera.

such example is shown in Fig. 3.28a) of a knife-edge scan recording and analysis performed with Karabo. This allows to check live the spot size of the pump laser at the sample position without having to transfer and analyze the data offline. One immediate limitation of Karabo as an online analysis tool is that it cannot handle the large amount of data generated by the DSSC detector for example. There a specific GUI centered tool, EXtra-foam [18], was developed by the Data Analysis group to provide some visualization and analysis capabilities for large pulse resolved detectors. An example of such analysis is shown in Fig. 3.28b) where EXtra-foam is used to perform an azimuthal integration of the magnetic scattering pattern recorded by the DSSC detector. In addition, the difference between pumped and unpumped azimuthal integration is binned as a function of time delay. This allows to confirm live the reduction of the scattering pattern when the sample is excited, giving a quick feedback on the stability of the spatial overlap between the optical pump and the X-ray probe and that the sample is not getting damaged by the pump pulses. One drawback of EXtra-foam however is that it cannot process all the data generated by the DSSC and is limited to 64 frames per train. In addition, other analysis may require more specific procedures, such as the BOZ XAS analysis which requires certain correction to be applied on the DSSC data. For this situation, EXtra-metro,[54] which can handle all data generated by DSSC thanks to its innate parallelization, was employed and the output integrated in a Karabo scene as shown in Fig. 3.28c). Another example is shown in Fig. 3.28d) where holography reconstruction with the PI-MTE3 camera is performed live with a custom EXtra-metro analysis which is then displayed in a Karabo scene. Finally, the option to stream the data to an external analysis tool provided by Users exists but was not yet used at the SCS Instrument.

For offline analysis, Users usually use jupyter notebooks on the Maxwell cluster.[20] Examples of data analysis and code specific to the SCS Instrument are provided in a python package called the SCS Toolbox [66] which is build on top of the more general purpose extra-data python package [17] provided by the Data Analysis group. For each beam time a new analysis environment is created within jupyter, which is essentially frozen once the beam time is over to enable reproducible data analysis in the future.

4   Future developments

4.1   Instrument upgrades

4.1.1   FFT

The FFT experiment station is in operation since the start of x-ray commissioning in 2018. In the meantime several smaller improvements around the sample environment took place. Coherent diffraction imaging has not reach it full potential to perform imaging of nanoscale magnetization dynamics. A major improvement step is expected with the advent of the helical afterburner Apple X in SASE3.

On the other hand the use of diffraction optics for BOZ-XAS demonstrates the potential for other applications such as mid-term development of X-ray microscopy and nano-probe CDI. Further, diffraction optics or the Apple X afterburner allow for generating orbital angular momentum beams which offer new tools to investigate for instance topological states in matter.

The sample environment of the FFT will need to accommodate high-field magnets to extend the range of sample systems for experiments at the SCS Instrument including the study of ultrafast antiferromagnet dynamics, and to a fully exploit the spectroscopy tools using circular and linear polarized X-rays.

4.1.2   THz-wave decoding of FEL pulses for pulse-arrival monitoring

The main limitation for pulse arrival monitors (PAM) based on transient reflectivity/transmissivity detection [8] is that they require high X-ray fluence ($>20\,\mathrm{mJ\,cm^{-2}}$) to induce measurable changes. This is near the damage threshold of SiN membranes or any other materials within the soft X-ray range and excludes parasitic operation because essentially the whole pulse energy is required for the PAM measurement [23; 11]. In addition, the penetration depth of soft X-rays is around 100 nm which further limits the measurement of the relative arrival time downstream to the solid-sample used for actual experiments. Picking off a side portion of FEL beam for the PAM upstream of the sample will negatively affect X-ray experiments requiring wavefront stability, and is still limited by available pulse energy. To measure the single-shot relative arrival time between the X-ray and optical pulses, the PAM
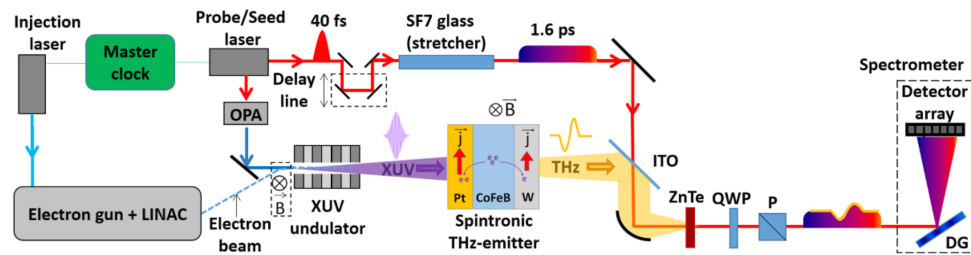
Figure 4.1: Experimental setup for single-shot spectral-encoding-based detection of THz pulses. A synchronized optical pulse is stretched using glass for spectral-encoding-based electro-optic sampling (in ZnTe) of THz pulses generated by a spintronic THz emitter (Pt (2 nm) /CoFeB (1.8 nm) /W (2 nm), 10 mm × 10 mm size, grown on 500 μm z-cut sapphire substrate) using XUV/FEL pulses (with 20 nm and 20 nm wavelength, 30 fs and 30 fs pulse duration, 25 Hz repetition rate, 8 mm beam size, up to 42 μJ energy). The THz-modulated stretched optical pulse spectrum is measured with spectrometer. [34]

must operate upstream to the sample position in parallel to the experiments and in a non-invasive manner.

Therefore, a novel timing jitter measurement scheme based on single-shot electro-optic sampling by spectral encoding of THz emission [40] induced by FEL pulses has been developed for the potential application at the SCS Instrument in a collaboration with scientists from Helmholtz center Dresden-Rossendorf and Technical University of Berlin. The method development and the results are summarized in the PhD thesis of Naman Agarwal [1] and published in Optica (2022)[34]. The approach requires very small fluence ($<100\,\mu J\,cm^{-2}$), a sample thickness of less than 100 nm (with a responsive layer thickness of just 6 nm), and does not affect wavefront as it uses full beam in transmission geometry. An experiment, demonstrating the potential sensitivity of such a scheme, was performed at EIS-TIMEX beamline of the seeded free-electron laser, FERMI at Trieste, Italy.

Figure 4.1 illustrates the setup implemented for single-shot spectral-encoding-based detection of THz pulses. XUV-FEL pulses were used to excite a in-plane magnetized spintronic emitter placed inside an UHV chamber. The XUV pulses were incident at the normal to the sample, generating a spin current inside the magnetic layer (CoFeB). The induced spin current is converted to radiative charge current or THz emission at the interfaces (Pt/CoFeB and W/CoFeB) due to the inverse spin Hall effect [67]. The emitted THz pulses were coupled out of the vacuum chamber and analysed in ambient conditions by electro-optic sampling with 800 nm chirped optical pulses of 1.6 ps duration at 50 Hz repetition frequecncy. A 2 mm-thick ZnTe crystal was used for electro-optic sampling, limiting the bandwidth to 1 THz due to the mismatch between the phase velocities of the THz and optical pulses over the 2 mm path length.
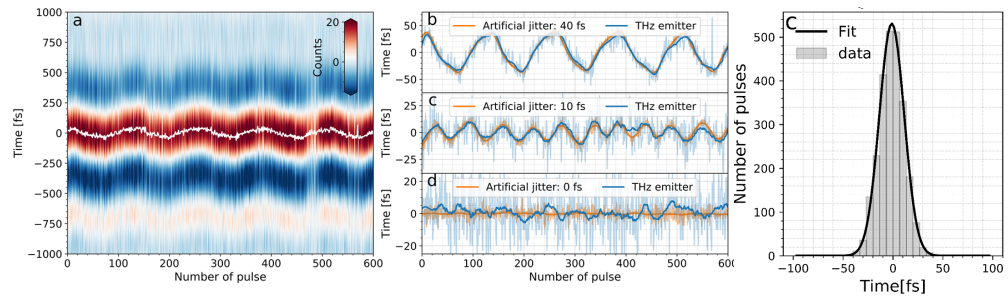
Figure 4.2: THz-detection-based FEL pulse arrival monitor. a) Single shot THz pulses for 600 consecutive XUV pulses with an artificial jitter of 40 fs. Color coding represents THz field strength. The white line shows the estimated jitter. b), c) and d) Artificial jitter (from delay stage) and THz-detection-based estimated jitter for 40 fs., 110 fs. and 0 fs. (intrinsic) amplitude. e) Histogram of intrinsic jitter for 2500 XUV pusles

Taking advantage of a seeded-FEL source, correlation measurements were performed where artificial saw-tooth type timing jitter was introduced in optical laser path to determine the robustness and reliability of the measurement setup. The timing jitter from THz pulses was correlated with delay stage values. Figs. 4.2 b) and c) show that 40 fs artificial jitter can be detected with very high degree of correlation, whereas 10 fs artificial jitter (not including intrinsic jitter) shows a lower degree of correlation with measurement sensitivity between 0 and 10 fs. A histogram of around 2500 pulses, Fig. 4.2 e), shows the timing jitter of the THz pulses with $\sigma = 12.4$ fs, including the intrinsic jitter of the XUV pulses and our instrumentation. This determines the sensitivity of this measurement scheme.

This proof-of-principle experiment demonstrates that pulse-resolved relative arrival-time information between FEL and optical pulses can be obtained with better than 10 fs accuracy with very low FEL fluence. The timing accuracy observed in the experiment compares well with other methods [23; 8; 11; 22; 60]. In addition, it can be used as single shot relative intensity monitor for FEL pulses [1; 34]. The next step will be to test this approach in the soft x-ray regime at SCS. If successful, we anticipate including THz emission (potentially with other techniques) in a dedicated PAM upstream of the KB mirrors to parasitically monitor the relative FEL and laser pulse arrival times during all experiments.

Since the bandwidth and shape of the THz pulse depends on the excitation pulse, this scheme should also be able to provide a measure of the pulse shape and pulse duration of FEL pulses, which normally require complicated techniques [22; 32; 35]. While it remains to be experimentally investigated, simulations [34] show that it is possible to differentiate between THz pulses generated by XUV pulses of different pulse durations or wavelengths. Different electro-optic crystals should be explored in

terms of measurement sensitivity and THz detection bandwidth.

Interestingly, from the fact that the electric field of the THz pulse is directly proportional to XUV pulse intensity, it is speculated the THz emission process from XUV pulse excitation of the spintronic emitter should be similar to that in the optical regime based on hot electron pulse generation. In this experiment, there was no noticeable difference in THz generation from 20 nm and 29 nm XUV pulses compared to 800 nm optical pulses. This suggests that the THz intensity from a spintronic emitter depends only on the absorbed energy density, which is similar for the optical and XUV excitation. This hypothesis needs further investigation for different X-ray wavelengths. Since the penetration depth in the soft X-ray region becomes significantly larger, it can lead to a reduction in THz pulse energy using spintronic emitters. Thus, other materials like photoconductive antennas (InGaAs etc.), photo dember samples (InAs) and organic crystals (DSTMS), which have shown high THz generation efficiency in the optical regime, should be explored in the soft X-ray regime for their efficiency and working principles. More transparent materials with high THz emission efficiency are required for non-invasive measurements of the arrival time. It should also be noted that this technique, in principle, can also be extended to study the magnetization dynamics of the materials itself at the same time [4].

With ultrafast, FEL-based experiments moving towards the attosecond regime, arrival time measurement techniques also need to be pushed for better sensitivity. Ultra-Broadband THz/far-infrared generation by attosecond pulses and single shot detection should be explored as one of the possibilities to achieve attosecond timing information and FEL pulse characteristics in the simplest way.

4.2 Extensions to the CHEM station

The first liquid jet experiments carried out during the user-assisted commissioning program in the Spring of 2022 demonstrated that the performance hRIXS spectrometer and the high brilliance provided by European XFEL enables unique scientific opportunities for solution-phase chemistry. The SCS team plans a number of extensions to the CHEM environment that will help best exploit the uniqueness of the facility and existing instrumentation. The planned technical developments are focused on two areas key areas: sample delivery and implementation of XAS for solution samples. Developments to the sample environment will be related to the implementation of new novel designs for liquid jets and the reduction of sample quantities required for experiments. The new liquid jets will include flat jets that enable transmission-mode XAS. The XAS implementations will port existing technology for the FFT and both zone plate XAS and TIM concepts will be implemented. Together these developments will enable experiments that combine RIXS and XAS.

4.2.1 Sample delivery: flat jets, nozzle exchanger, temperature controls, and sample recirculation

Beginning with the Spring 2022 call for proposals, the SCS Instrument offered in standard configuration to the users for liquid jet experiments. This standard configuration offers cylindrical liquid jet and cold trap for spent sample as described in
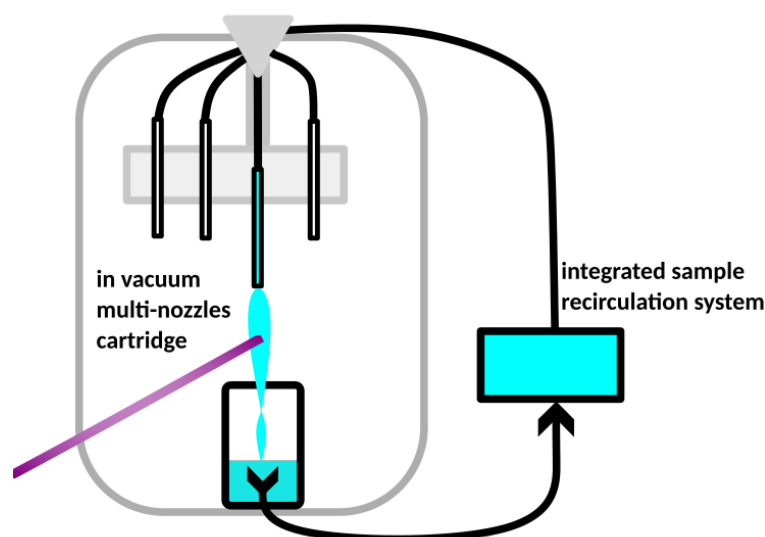

Figure 4.3: Schematic of liquid sample environment. Key developments are sample recirculation and a scheme for switching nozzles without breaking vacuum.

the operation section of this report. Extension of this standard configuration to a more reliable and flexible platform is envisioned in Figure 4.3.

The first key development is the introduction of a cartridge that holds multiple liquid jets allowing for nozzle exchange without breaking vacuum. Currently, if a liquid jet becomes clogged and replacement or cleaning of the nozzle is deemed necessary, this results in a 2 hr loss in measurement time because the chamber must be vented and the nozzle must be manually replaced. The new scheme will include a motorized stage than can position one of several nozzles at the interaction region. This will be combine with a switching device that selects which of the nozzles receives the liquid flow from the pump.

An important development for enabling studies on precious samples is the ability to recirculate the sample. The current CHEM liquid jet operates with flow rates of 1-3 ml/min, which leads to a typical sample consumption of ∼3 l per day. With the current setup utilizing a cold trap, large quantities of sample is required because the sample is not reused. This can mean that up to a kg of material is necessary for an experimental run. This limits the systems that can be studied to samples that are commercially available samples that can be purchased in large quantities. It can also be financially limiting for some systems such as metalloproteins where a gram of sample can easily cost >1,000 €, and 10's of grams could be required for a 1 l solution with a concentration of 1 mM. Consequently, a commercial recirculation system is being procured to enable experiments on samples that can only be synthesized in small quantities or have high costs. We estimate that sample volumes can be reduced to a resevoir of 100 ml or less. In cases of no X-ray or laser induced damage, experiments could run with a single 100 ml sample volume.
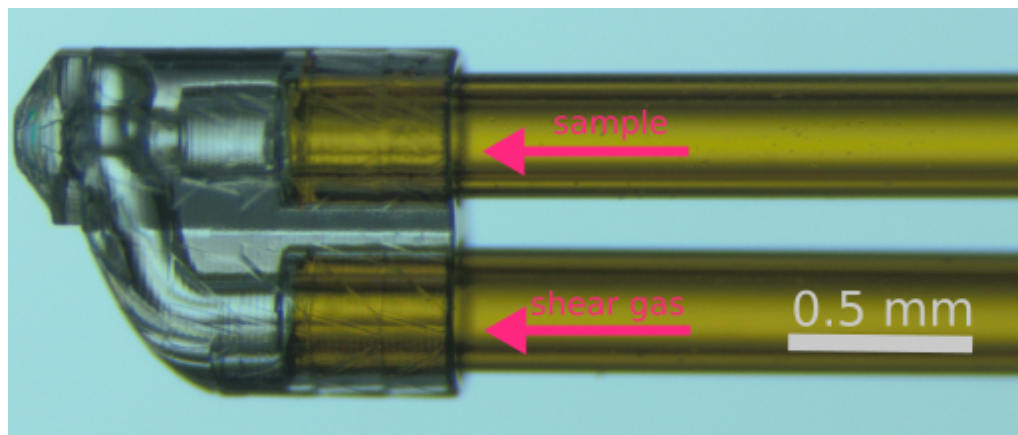

Figure 4.4: 3D printed micro nozzles: image of a device before to be completely assembled.

The range of experiments is also currently limited by the solvents that can be utilized. To date only water, ethanol, and isopropanol have been used. One issue is that many commonly used solvents in inorganic chemistry have low viscosity such as acetonitrile and methanol. Low-viscosity solutions lead to turbulent flow that prevents the formation of a stable liquid jet. In order to counteract this effect, sample cooling will be implemented. By cooling both the sample reservoir and the tubing delivering the sample, the viscosity can be increased and laminar flow of the jet established.

The final critical component for the CHEM sample environment is the development of new liquid flat jets. In particular, they must run under vacuum stably for hours providing generating sub-micrometer liquid sheets. Current liquid micro-jet technology has demonstrated the capability of providing micrometer thick sheets jets with different approaches[14], such as a lithographically etched microfluidic chip[39] and a 3D printed slit nozzle[24]. Our goal is to deliver a load-lock system containing the nozzle holder and catcher that allows integrating additional components with ease, e.g. a differential pumping section to achieve the ultrahigh vacuum required for the spectroscopy and scattering experiments at the soft x-ray instruments. The jets we are developing utilize 3D printed microfluidics that generate gas dynamic virtual nozzles (GDVNs) as shown in Figures 4.4 and 4.5. The capability of rapid prototyping using in-house equipment and expertise in the Sample Environment and Characterization (SEC) group at XFEL allows the possibility of studying new microfluidic devices.[38] These efforts will create a library of accessible of designs for various liquid jet applications to service user experiments with different needs.
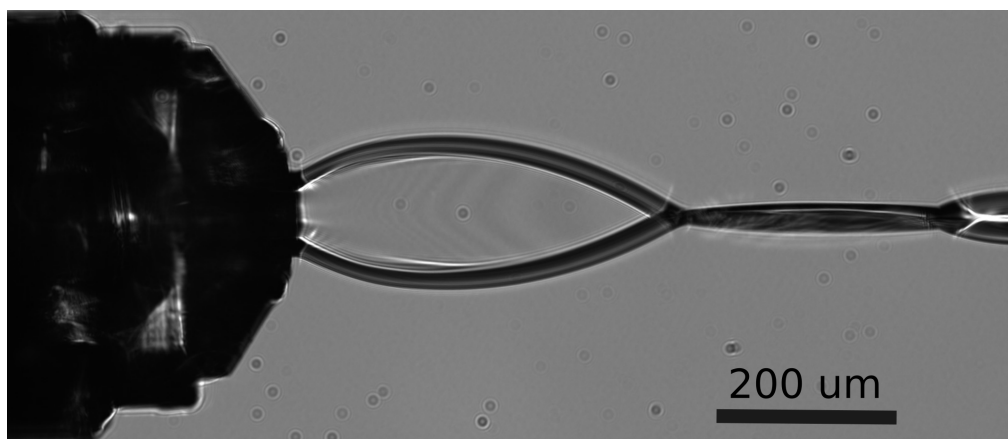

Figure 4.5: Example of water flat jet from a gas accelerated driven device, image acquired in a laboratory set up, water 0.5 ml/min, shearing gas Helium.

4.2.2   XAS of dilute systems and biomolecules in transmission

Molecules and materials containing 3d transition metals play a key role in many (photo)catalytic and biologically active systems where they participate in a wide range of processes including charge and electron transfer, small molecule activation, and atom transfer reactions. Understanding these processes in a way that enables one to rationally design new materials requires a detailed knowledge of the electronic structure of these sites. This goal necessitates probes of the transition metal's electronic structure that can track chemical changes on the ultrafast timescales in solution. Transient L$_{2,3}$-edge X-ray absorption spectroscopy (XAS) is in principle an ideal probe of transition metal electronic structure due to its site-selectivity and ability to probe the catalytically active 3d orbitals. The underlying 2p to 3d transitions have been shown to be sensitive to oxidation state, spin state, and the ligand field. Despite these advantages, the 3d L-edges fall within the soft X-ray range with energies between 400 to 1000 eV, which poses several technical challenges. Firstly, experiments must be carried out in helium or vacuum environments, and
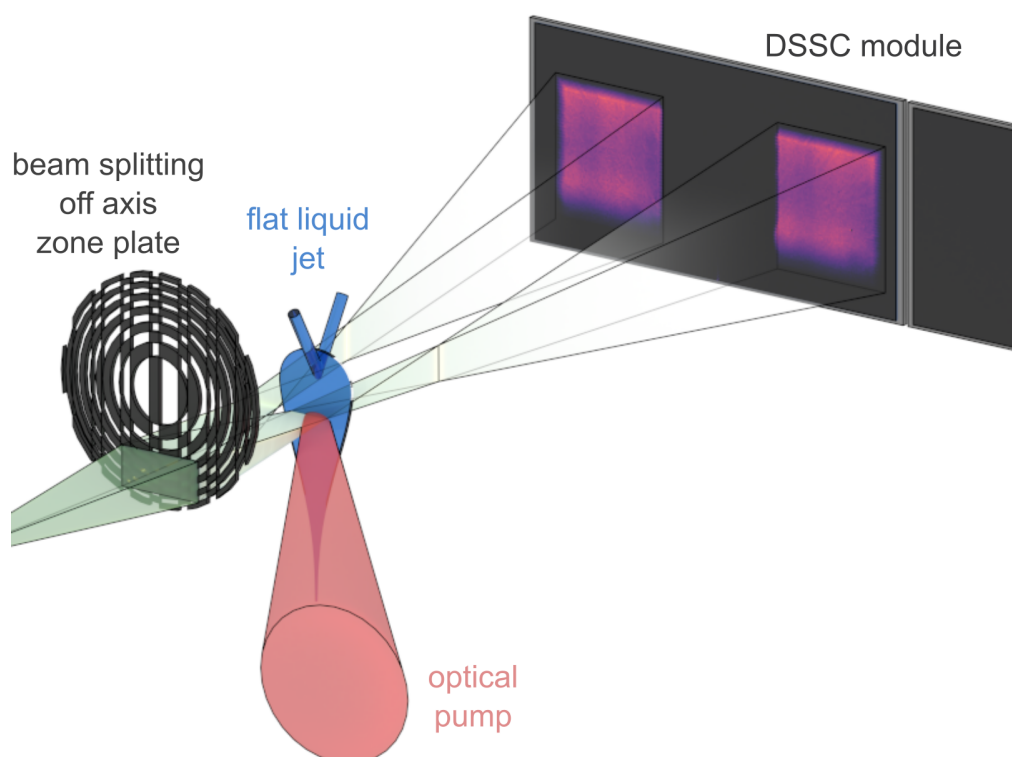

Figure 4.6: Beam-splitting off-axis zone plate (BOZ) diffractive optics, combined with a flat liquid jet. The optic is designed to provide a line focus at the flat liquid jet position. The optical pump is exciting only half of the line to provide a pumped and unpumped measurement simultaneously. A single DSSC module is used to detect the transmitted intensities.

solution phase experiments further require special methods for introducing liquid samples (cells or jets). Secondly, thin samples are required to obtain artifact free spectral intensities for XAS measurements. It has been shown that only transmission-mode measurements of soft X-ray XAS provide reliable cross sections because fluorescence measurements suffer from state-dependent Auger dynamics. Transmission mode measurements require thin highly concentrated samples due to small X-ray penetration depths of the solvent. Liquid flat jets fulfill this requirement as they achieve sample thicknesses on the order of few 100 nm. Previous transient experiments have focused on model complexes with concentrations of 10's of mM or greater [33; 21], and measuring the static XAS of metalloproteins has even proven to be a major challenge.[42]

The SCS Instrument is developing a transient XAS setup using a beam-splitting off-axis zone plate (BOZ) diffractive optic combined with a flat liquid jet in one setup, as depicted in Fig. 4.6. One beam bypasses the liquid jet while the other passes through the jet and both are detected on the same detector. It was shown with low-noise CCD detectors that the sensitivity can reach the shot noise limit, as discussed in sec. 2.1.2 A previous study combined this scheme with a flat liquid jet to demonstrate XAS measurements at 400 eV was essentially limited by the photon flux available at FLASH-1.[15] It is thus essential to develop this technique further for soft X-ray spectroscopy at XFELs. The Spectroscopy and Coherent Scattering (SCS) instrument at the European XFEL is the ideal place for such experiments for several reasons. First of all, up to 800 pulses at 10 Hz can be detected with the world's fastest soft X-ray DSSC detector for an effective repetition rate of 8 kHz.[58] Secondly, the CHEM chemistry end-station is commissioned and can be equipped with a flat liquid jet as disccued in sec. 4.2.1.

A second scheme for time-resolved XAS will use a second transmission intensity monitor. A differential pumping section will be added downstream of the chemistry chamber. This will re-establish UHV conditions and enable the use of a pulse-resolved TIM. The TIM will follow the design of the existing instrumentation described in 3.5.4.

4.3 Time-resolved RIXS and XRD studies

4.3.1 Far-IR/THz pump source

A key requirement for TR-RIXS studies of complex materials are suitable excitation sources. It is no longer sufficient to excite the electronic system non-resonantly and monitor the cascade of energy through the internal degrees of freedom.

In quantum materials with significant electronic and magnetic properties, manifesting themselves at temperatures of tens or hundreds of kelvins, the significant excitations are in the energy range from few meV to 0.1 eV. Those are mostly phonons and charge excitations, e.g., across superconducting gaps. Therefore, it is imperative to equip the hRIXS instrument with a tunable optical pump source in the 1 THz to 20 THz, (4 meV to 83 meV, 300 µm to 15 µm) range driven by the PP laser in SASE3.

To this end, the SCS group initated an EuXFEL R&D project to build and utilize a suitable source in collaboration with Polytecnico di Milano (Group of G. Ghiringhelli) and MPI-MPSD (group of A. Cavallari). A PhD student (Giacomo Merzoni) has been appointed to the project and will be support by SCS staff and the other collaborators. The scientific goal of the project is the study by RIXS of the metastable states induced by the coherent excitation of specific phonons in superconducting cuprates or titanates. The complex mechanisms behind the surprising "light induced superconductivity" are still unclear, involving indirect phonon excitations, transient structural distortions, change in the in plane hopping integrals and exchange interactions, and out-of-plane electronic reconstruction. TR-RIXS can probe directly those degrees of freedom by measuring modifications in the magnon and dd excitation energies, in optical phonon intensity and in the charge density wave correlation length. Both systems of interest have been extensively measured at synchrotrons, providing a solid interpretation framework for TR-RIXS.

On the laser side, the project's main objective is to design, test and employ an OPA based, probably, on potassium titanyle arsenate ($KTiOAsO_4$ or KTA) pumped by the 800 fs, 1030 nm pulses of the PP Laser. The group of A. Cavalleri (MPI-MPSD, CFEL) has developed a similar mid-IR table top source, with high pulse energy (1.9 µJ), tunable between 4 THz to 18 THz (16 meV to 75 meV), based on the difference frequency generation (DFG) of near-IR chirped pulses from a Ti:sapphire source [[44]]. Their expertise will be exploited for the development of a tunable THz-farIR source for hRIXS based on the existing infrastructure of the PP laser in SASE3. Optical design work has recently commenced.

To make progress on the complicated task of bringing mid-IR/THz radiation into the

XRD chamber while the OPA is developed, the project will start by making use the the existing, commercial OPA (Topas from Light Convesion) pumped by the 800 nm PP laser to produce 3 μm to 15 μm pulses at 113 kHz. Specifically, the (DFG) extension produces femtosocond pulses between 3 μm to 10 μm with pulse energies between 6 μJ to 0.6 μJ, respectively.

The R&D project complements and is complemented by two ongoing THz source developments within the PP Laser Group. The furthest advanced of them is based on THz generation in $LiNbO_3$ pumped by 800 fs, 1030 nm pulses from the PP laser. This scheme generates a single-cycle pulse centred around 0.3 THz. One apparatus has been tested at the FXE Instrument and construction of a second device for SCS is underway. The advantage of this approach is it's high pulse energy. The disadvantages are the low frequecy and lack of tunability.

The second Laser Group project for THz sources has a longer outlook. Here the idea is to use the second harmonic of the 800 fs, 1030 nm pulses, as is currently done for the 800 nm NOPA, to pump two tunable OPAs operating about at around 1 μm. DFG between these pulses will then produce tunable mid-IR/THz pulses at higher pulse energies than using the Topas.

Although the SCS R&D project is focused on the XRD endstation and RIXS experiments, it is anticipated that the sources will be a general tool available to SCS Users in combination with other endstations and experimental geometries.

4.3.2   Extending RIXS studies into tender x-ray regime

Instruments allowing studies in the tender x-ray regime are very rare. Tender x-rays are placed between soft and hard x-ray range and are facing technical challenges. In addition, most facilities are optimized either for the operation in the soft x-ray (below 2 keV) or in the hard x-ray (above 5 keV) regime. One instrument in operation for tender x-ray inelastic studies is IRIXS at Petra III [27; 6]. IRIXS is working in the energy range from 2,5 – 3,5 keV and was optimized for studies at Ru L3 edge [27; 6; 71; 26; 5; 72]. The large range of studies at other resonances is still unexplored.

While the SCS beamline allows studies from 250 eV in the soft x-ray range up to 3000 eV in the tender range, the current working range of the hRIXS spectrometer covers 250 eV – 1500 eV. The hRIXS user consortium has performed calculations to optimize parameters for a third, high-energy grating for the hRIXS spectrometer. The results look promising, showing that with a single grating we will cover the energy range from 1500 eV - 3000 eV (see Fig. 4.7). With this grating hRIXS will
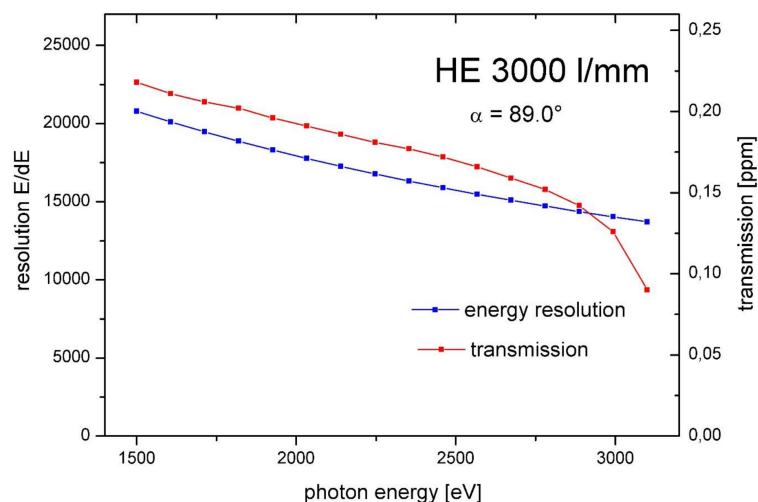
Figure 4.7: Expected resolving power and transmission for the high-energy grating (hRIXS internal report by F. Senf *et al.*). The calculations were done for 5 μm source size, 10 μm detector pixel size and 0.25 μm rms slope errors for the laminar 3000 l/mm grating.

become the first instrument offering RIXS in the tender regime at an XFEL and for the first time allow time-resolved inelastic x-ray scattering studies for a large family of compounds. In particular the K-edges of the common ligands P, S and Cl will be accessible and the L edges of several 4d transition metals, including Nb, Mo, Tc, Ru and Rh. These resonances are of large interest to the chemistry community, as well as to the solid-state community focusing on complex materials and strongly correlated electron systems.

The tunability of the European XFEL to different working points (up to now operating at 11.5, 14 and 16.3 GeV) provides high flux to the SCS Instrument in the soft x-ray and the tender x-ray regime, see Section 3.1.1 on page 37.

4.3.3   X-ray standing waves to study structural dynamics

Among the broad class of quantum materials, multiferroics represent promising candidates to significantly reduce microelectronics energy consumption. A multiferroic is a material possessing two or more ferroic order parameters, e.g. ferroelectricity (FE) and ferromagnetism (FM). Materials simultaneously ferroelectric and ferromagnetic offer the possibility of controlling magnetism by means of electric field [47]. A material with large, robust and strongly coupled magnetization and polarization at room temperature does not exist yet. To advance this search, a fundamental understanding of the relation between atomic structure and function is
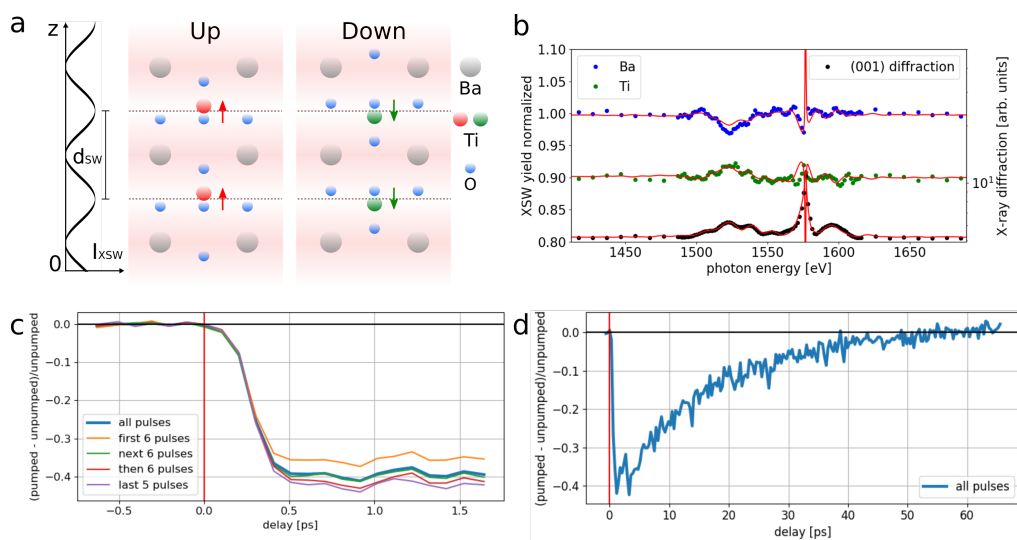
Figure 4.8: a: projection of $BaTiO_3$ unit cell with up and down polarization. b: (001) X-ray diffraction (black), Ba (blue) and Ti (green) photoelectron yield of $BaTiO_3/SrRuO_3/DyScO_3$, and corresponding fit curves (red) as function of the incoming X-ray photon energy. Ti yield is shifted by -0.1 for clarity. c and d: time-resolved SHG of $BaTiO_3/SrRuO_3/GdScO_3$ measured at different delay ranges. Each laser train consisted of 23 pulses. Panel c shows the slightly different dynamics induced by different pulses in the train.

essential [70]. Furthermore, one of the great scientific challenges in the next years will be understanding and controlling the dynamics of multiferroic switching, with the ultimate goal to achieve an all-optical-switching multiferroic device. To this end, the X-ray standing wave (XSW) technique can play a crucial role to correlate atomic positions of multiferroics with their function and thereby guide the pursuit of materials with the desired properties.

In a nutshell, the XSW is formed in the region of spatial overlap between two coherently coupled incoming and Bragg-diffracted x-ray plane waves [78; 75]. This results in a sinusoidal x-ray intensity modulation with period d_{SW} (Fig. 4.8a) perpendicular to the diffracting planes. In an XSW experiment the photon energy hv, of the incoming x-ray beam varies through the Bragg reflection, the standing wave shifts by $d_{SW}/2$. By monitoring simultaneously X-ray diffraction and the photoelectron (or fluorescence) yield of atoms as the XSW moves through the sample, the position of the emitting atoms can be retrieved with pm accuracy.

The goal of this R&D proposal is to establish the XSW technique in pump-probe experiments as a tool to probe the structural dynamics of multiferroics. To this end, the prototypical and extensively studied ferroelectric $BaTiO_3$ was chosen. $BaTiO_3$ films of thickness $20 - 40$ nm, with a 25 nm $SrRuO_3$ bottom electrode, were grown

by pulsed laser deposition on scandates crystals, imposing different compressive strains. Fig. 4.8b shows (001) X-ray diffraction peaks of 20 nm $BaTiO_3$ / 25 nm $SrRuO_3$ / $DyScO_3$ measured recently at the I09 beamline of Diamond Light Source. The corresponding photoelectron yield curves of Ba4d and Ti2p core levels provide the relative distance of Ba and Ti atoms from the Bragg planes, equal to 0 Å and 2.12 Å respectively (Fig. 4.8b). These preliminary results demonstrate the structural accuracy of the XSW technique in determining the atomic positions for this class of materials.

Theoretical studies predicted that above-bandgap excitation in $BaTiO_3$ induces a rearrangement of the atomic charge density leading to a decrease of ferroelectric order [43]. This was indeed experimentally demonstrated by time-resolved second harmonic generation (SHG) experiments performed at in the instrument laser hutch of SCS. The SHG technique is sensitive to lack of inversion symmetry [79], typical of ferroelectric materials. In particular, optical laser pump pulses at 266 nm with 0.5 mJ/cm^2 fluence induced a transient 40% reduction of the SHG signal within 500 fs (Fig. 4.8c), with a complete recovery after 60 ps (Fig. 4.8d).

We aim to investigate the structural dynamics of $BaTiO_3$ thin films, and more generally of other multiferroics, by tracking atomic positions in real time using the XSW technique. The experimental implementation at the SCS Instrument is particularly suited for XRD chamber, to measure X-ray diffraction, in combination with hRIXS spectrometer, to measure fluorescence yield of different atomic species.

4.4   Future detectors

The needs and requirements for future detectors have been collected in the Requirements for Detector Development report by the Detector group based on the inputs from the Scientific Instruments of the European XFEL and presented to the Detector Advisory Committee in June 2022. Here we present some essential points of this report as well as some other developments.

4.4.1   Pulse resolved detector for hRIXS

Currently the RIXS spectrometer is equipped with a PI-MTE3 commercial X-ray camera. The most stringent requirement regarding the detector for hRIXS is spatial resolution. For example, with the PI-MTE3 camera and its 15 μm pixel size, a 10000 resolving power was demonstrated. A camera with 30 μm pixel size giving a 5000 resolving power would also be sufficient for most experiments. The drawback of this commercial detector is the readout time which is not even sufficient to readout individual FEL trains.

A faster detector providing train resolved readout would open the possibility for train-to-train time jitter correction which are provided by the beam (BAM) and the future laser pulse arrival-time monitors (LAM), improving the time resolution of hRIXS experiments. An even faster detector capable of resolving pulses within the EuXFEL train would open the possibility for correcting jitter within the train as well, although the gain here is more moderate. More importantly, a pulse resolved detector would offer the possibility of alternating pumped and unpumped pulses during the train for better normalization of the collected data. Currently, such unpumped normalization data are collected minutes before or after pumped data. A detector able to distinguish single EuxFEL pulses would also provide valuable information on the liquid jet dynamics during pump-probe experiments at high repetition rate (MHz) in the CHEM chamber. Such information could be used for example to optimize the liquid jet flow rate. Finally, such detector would also open the way for pulsed magnetic field studies where the magnetic field varies over the FEL train.

The need for a pulse resolved detector for hRIXS was always clear. For this purpose, a first option based on a microchannel detector with multiple delay-line readout (MCP-DLD) was investigated. Unfortunately, differently to the specifications agreed with the provider, the system delivered to the European XFEL can only achieve a 200 μm resolution along the delay-line direction, which is by far not sufficient for hRIXS applications. Fortunately, a second option appeared very recently and based on proven technology. The Paul Scherrer Institut has been developing a Jungfrau

detector optimized for soft X-rays with RIXS one of the potential applications. With 25x250 μm rectangular pixels and up to 16 intra-train pulses readout, it offers promising specifications for this application. The possibility of testing and using it at the SCS instruments for hRIXS is presently under discussion between PSI and the EuXFEL.

4.4.2   Needs for future 2D detectors

Currently a miniaturized silicon drift detector (MiniSDD) based 1 megapixel DSSC camera with linear gain exists [58] and a DEPFET based 1 megapixel DSSC camera with non-linear gain for signal compression at the sensor level is being assembled.[57] The advantage of the DEPFET over the MiniSDD technology is on one hand the lower noise (a factor 3 lower with respect to miniSDD was measured) which improves the single photon detection capabilities. On the other hand, the gain compression extends the dynamic range of the detector. This comes at the price of a more complexe calibration procedure and a subsequent gain correction step needed to convert the detector readout into the number of detected photons.

For scattering experiments, low intensity high-q scattering and high intensity low-q scattering need to be detected simultaneously. Not only does the scattering intensity vary by several orders of magnitude over the image, but the overall image intensity largely fluctuates from shot to shot when a monochromatized SASE FEL beam is used. High pixel saturation values and low noise for single photon detection are thus needed to collect efficiently scattering images. These competing requirements make the DEPFET sensors, providing continuous signal compression and low noise, highly desirable. However, there are also classes of experiments where the spatial intensity variations are limited and precise counting of the detected photons as well as a linear response to the incident photon flux are most needed. This is the case, for example, for X-ray Absorption Spectroscopy with diffractive optics and possibly also for X-ray transmission microscopy. In these cases, the signal compression might be a disadvantage and a linear response detector such as provided by the miniSDD DSSC version could be preferable. A detailed strategy regarding the use of the DEPFET and MiniSDD cameras will emerge when the first experimental data from the DEPFET DSSC camera are recorded and analyzed.

In the longer term, new detectors will need to be developed to keep the SCS Instrument capabilities at the forefront of the technological and scientific progress. With improved semiconductor fabrication process, the size of a DSSC-like pixel which contains, among other things, the gain amplification chain, the analog to digital converters (ADCs) and SRAM data storage, all in a 229 by 204 μm area,[58] could be

significantly reduced. While for scattering experiments, the current DSSC pixel density is probably sufficient, holography and coherent diffractive imaging (CDI) call for higher pixel density. In holography, the ratio of the largest to the smallest real-space distance than can be sampled is N/4, where N is the number of pixels along one axis. For a small 5 μm field of view (FOV), the resolution with a 1 Mpixel detector is thus 20 nm. In applications, Users wants both larger FOV and better resolution to answer their scientific questions. Even more, when phase retrieval is employed in the reconstruction, a factor 2 to 4 oversampling is necessary, meaning an even further reduced spatial resolution in the final reconstructed image. For such applications, new detectors with 4 or even 8 Mpixels would be advantageous.

New detectors will also have to address the issue of the gaps between the sensors. Even in the case of scattering experiments, the way gaps are treated in the analysis had a significant impact on the results. For example, SCS Users Hagström and co-workers found out that for anisotropic magnetic scattering from oriented magnetic domains, the peak maximum extracted by conventional azimuthal integration would be affected by the presence of gaps in the detector. They propose instead to perform a two dimensional fitting procedure of the scattering data.[30] For holography and CDI, the situation is worse as each gap in the sensor translates into missing information, creating noise in the reconstruction. Such unknown information can in part be recovered with the help of mathematical methods, but the treatment is far from perfect and is time consuming. Gapless sensors are highly desired and SCS Users tend to prefer to use commercial CCD camera with continuous gapless sensor for holography imaging instead of the DSSC. However, from a manufacturing perspective, large monolithic sensor are difficult to manufacture. A possible solution would be to consider a shingled arrangement of the sensors, i.e. sensors sitting on slightly different planes. With a reasonable fabrication yield, a large >1 Mpixel camera could be assembled with functional and tested small sensor modules.

Finally, one of the main limitations of the current instrumentation at SCS when using solid state samples is the heat dissipation which effectively limits the usable repetition rate to about 10 pulses per train or 100 Hz. Pump-probe experiments on solid samples at rates between 10 and 100 kHz are feasible without being compromised by heat dissipation issues and would offer data rate increase of a hundred to a thousand. Therefore, a change of the EuXFEL operation from the current macro-bunch mode to a quasi-continuous mode at rates of some hundreds of kHz would be a major game changer and would open up large possibilities in terms of new science. Often, scattering experiments are limited by the small statistics of the data collected at high-q. This would largely improve with a three orders of magnitude increase in the data collection rate. For example, investigating how the magnetic domain structure changes during ultrafast demagnetization has been an elusive problem with many

contradicting results in high impact factor journals. The necessary data set to shed new light on this problem requires measuring at least the 1st, 3rd and 5th order magnetic scattering rings. This is currently at the limit of what can be done.[81] Similarly, imaging dynamical phenomena with holography or CDI techniques requires a large amount of data to be collected to even begin to see a reconstructed image. Time-resolved holography experiments will only benefit from a large increase in data rate, opening new possibilities for real space imaging of dynamical phenomena.

A change to quasi-continuous operation mode of the accelerator, of the pump laser system and of the detectors would also be beneficial for liquid jet experiments as the flow rate could be reduced. Of course, this increase in data rate also comes with a huge cost in data storage and processing. Strategies to reduce the amount of stored data will have to be integrated into these new detectors as well. A data policy and reduction working group has been created at the European XFEL to begin drafting such strategies.

4.4.3   Small DSSC modules

A fraction of the experiments performed with the 1 Mpixel DSSC detector use in fact only one ladder or even a single sensor of the detector. The main example is represented by all the BOZ-XAS based experiments described in sec. 2.1.2. This shows that the development of smaller form-factor detectors based on the DSSC technology, besides large megapixels cameras, would be beneficial. For example, another area of application for small DSSC modules would be Bragg peaks imaging with the XRD chamber. This would allow, for example, to follow the ultrafast dynamics of charge density waves (CDW) satellites around a Bragg reflection, or to monitor the phonon thermalization seen in the diffuse scattering around a Bragg reflection. These are examples of experiments that would interest the solid-state User community. The requirements for such an imaging detector are a fast pulse resolved readout, together with a high dynamic range covering both the intense Bragg reflection and the weak diffuse scattering. Such requirements are well suited for the DEPFET DSSC technology. A project is ongoing to equip with DSSC DEPFET sensors a small modular chamber, known as the "2D Rapide". This chamber was provided by a consortium of French Institutes lead by the Laboratoire de Chimie Physique-Matière et Rayonnement (LCPMR). Once completed, it would provide Bragg imaging capabilities with the XRD chamber at the SCS Instrument.

In addition, small compact DSSC modules could be used as replacement for MCP detectors that are used at the TIM as a fluorescence Io monitor replacement of the XGM. The advantage of DSSC modules in these application is the lower readout

noise. Electrical signals from MCPs are amplified, transported over long cables and only then digitized, and are therefore inherently noisier than DSSC module. The DET group is currently investigating how to provide this option, with the first step being developing a modular in-vacuum cooling block for small modules.
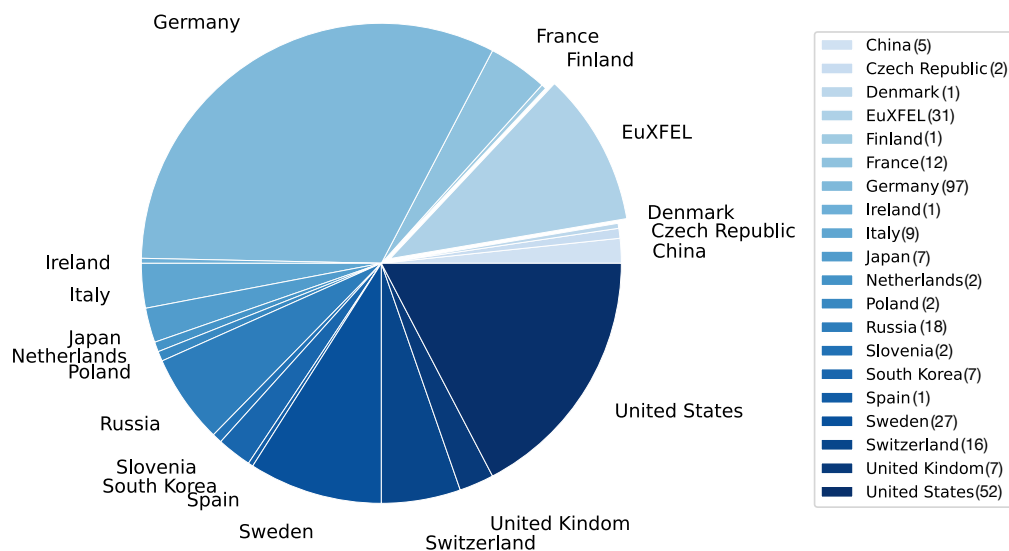
5   Metrics of SCS Instrument

Figure 5.1: International user community of the SCS Instrument. Users are listed according to the country of their head institute. Users participated in experiments from December 2018 till June 2022.

Figure 5.1 shows the international user community of the SCS Instrument with participation of nearly all European XFEL member countries. Note that the metric excludes to a large extend the new user communities who will perform experiments with just recently added instrument capabilities around the hRIXS spectrometer as well as XRD and CHEM experiment stations. First user experiments will start at the time of this report.
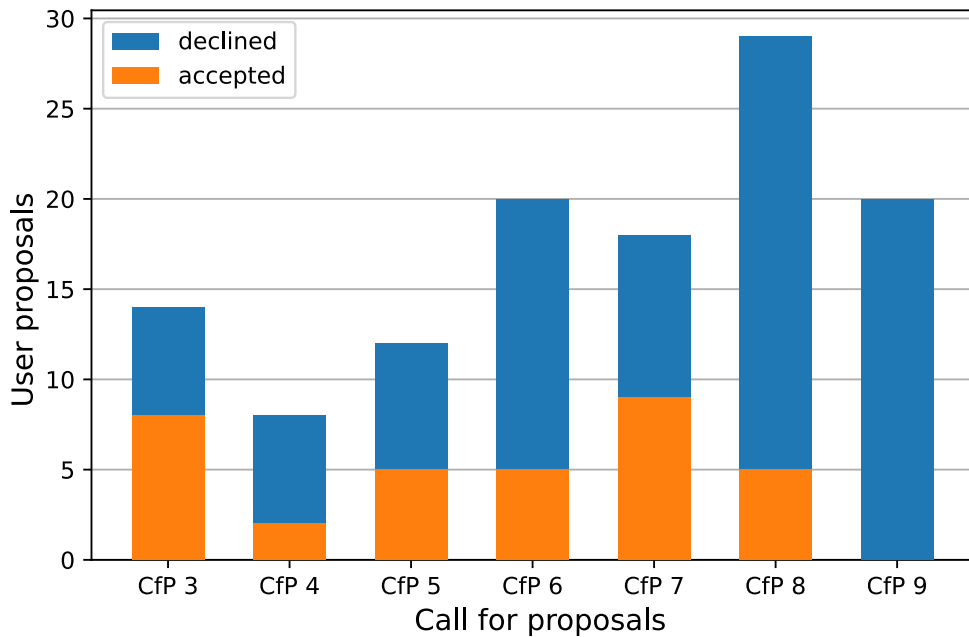
Figure 5.2: Number of proposals per call accepted (orange) and declined (blue) proposals

Figure 5.2 shows the number of submitted proposals increased after the start of user operation at the SCS Instrument where users initially organized and submitted "user community" proposals during the early operations. The first call for exclusively solid and liquid-phase RIXS proposals received 29 proposals which can be considered on top of the typical number of proposal submissions from previous calls. To mitigate a high over-subscription of the SCS Instrument, future calls shall limit the proposals to instrumentation around two experiment stations which will take turns each call, e.g. the 9th call for proposals addressed the FFT and CHEM experiment stations.

Note that 88,2 % of all user proposals submitted to the SCS Instrument demand the use of the PP optical laser. This shows that the optical and the X-ray laser delivery are of equal importance for the success of the user operations at the SCS Instrument.
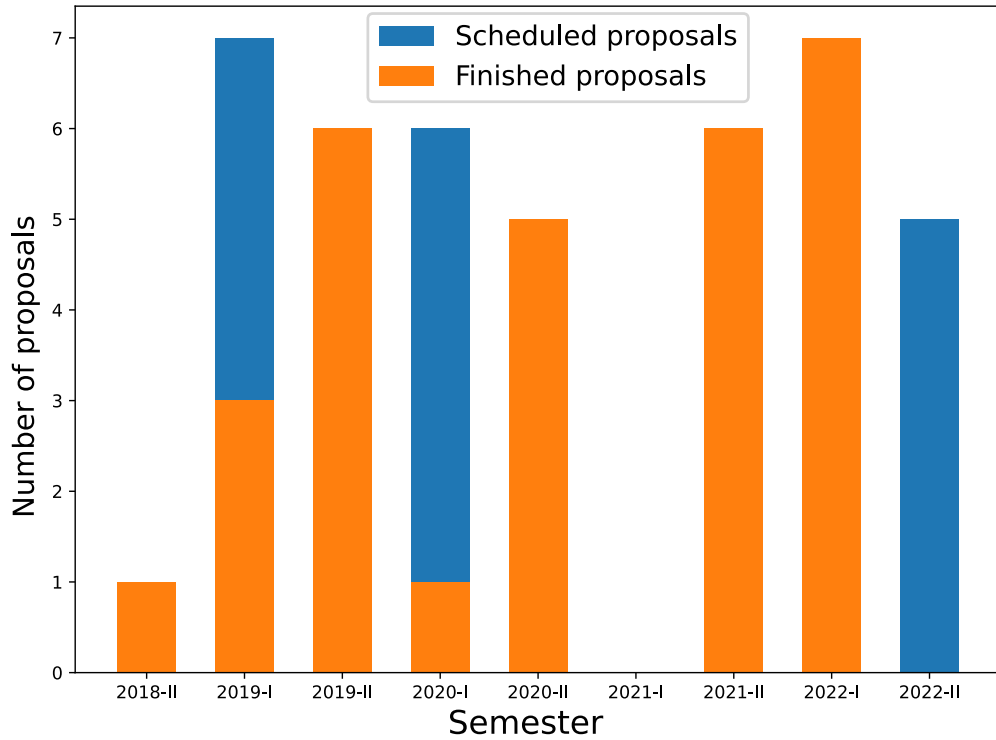
Figure 5.3: Number of finished or scheduled Proposals per semester

Six user proposals were scheduled on average and finished during one semester, see Figure 5.3. Exception have been during the startup phase of the SCS Instrument due to the stand-in laser system being unready for operation until May 2019. User proposals had to be rescheduled in 2019-II when the PP laser system became available to users in SASE3. Due to the Covid-19 pandemic, user operation was stopped in March 2020 and user proposals had been rescheduled. The slower ramp-up of the facility after winter shutdown in 2021-I due a continuous Covid-19 wave in Germany, reduced the X-ray delivery weeks for SASE3, accommodating only commissioning time for the hRIXS spectrometer and the additional high-resolution grating of the soft x-ray monochromator.
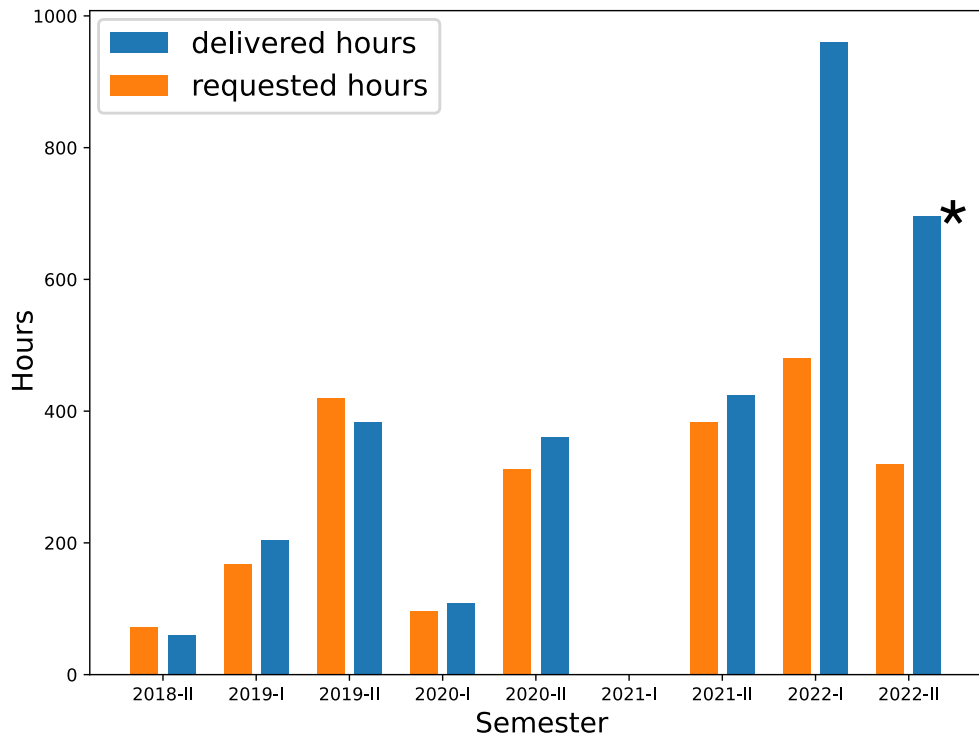
Figure 5.4: Number of hours requested by users in the proposal and delivered hours. (∗) estimated delivered hours according to the operation schedule in 2022-II

The user operation between two scientific instruments of a SASE port was in the early phase organized in a 12/12 hours operation mode, changing X-ray delivery between the two instruments once a day. This mode caps the delivery beam time per week and proposal. This is revealed in the overall agreement in the requested and delivered x-ray user hours over the past years in Figure 5.4. This mode has changed to 24hrs/6days operation with one instrument operating per week, leading to an overall increase of delivered hours to the users in 2022.

Distribution of operation modes per year

2019   **2020**   **2021**
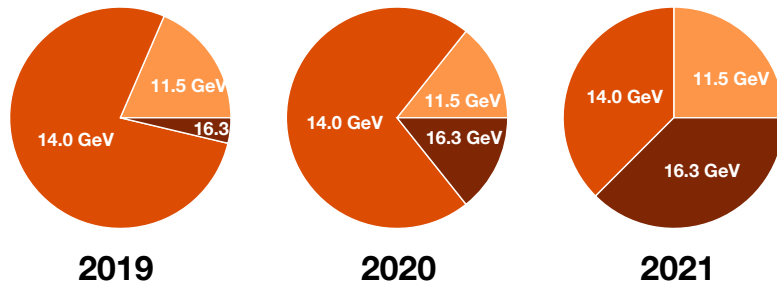
User proposals requirement
(all submitted proposals)

EuXFEL operation

- 8.5 GeV
- 11.5 GeV
- 14.0 GeV
- 16.3 GeV

Figure 5.5: Distribution electron-energy operation modes at European XFEL over the past years and user demanded operation modes given by the requested photon energy, see also Figure 3.3 on page 37
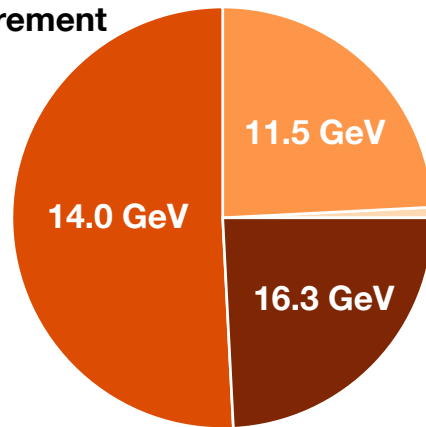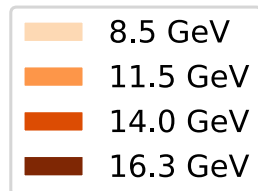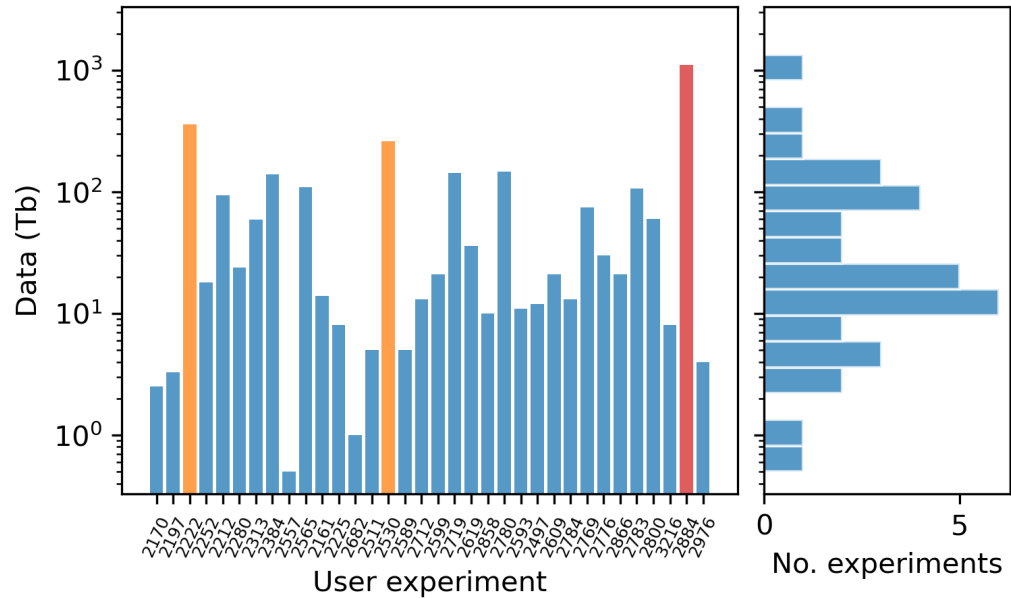
Figure 5.6: Data generated by each User experiments at the SCS Instrument. The proposal with most data generated at the SCS Instrument is UP 2884 Shen & al., with 1.10 Pb of data shown in red. The two next proposal by data generated are both holography experiments UP 2222 and UP 2530 Bonetti & al. with 358 and 260 Tb of data, shown in orange.

Figure 5.6 shows the amount of data generated by each User experiments that has so far been conducted at the SCS Instrument. Most of these experiments produced around 10 to 100 Tb of data, for a total of 2.93 Pb. However, three experiments together account for 40% of all the data generated at the SCS Instruments. The first one by data generated and shown in red in Figure 5.6 is the XPCS experiment, UP 2884 Shen & al., which generated 1.10 Pb of data alone. The two next experiments by amount of data generated are both holography experiments, UP 2222 and UP 2530 Bonetti & al., with 358 and 260 Tb of data. Each of these three experiments relied on the DSSC to record hundreds of frames per train. In particular, the XPCS experiment, UP 2884 Shen & al., used 800 frames per train which is the most the DSSC can acquire. Therefore, if the DSSC is employed more frequently in the future for experiments making use of the DSSC 800 frames, several Pb of data could be generated each semester.

5.1 List of publications based on user proposals or commissioning beamtimes at SCS Instrument

➲ The publications and preprints under review can be downloaded as a zip file for the review using this link: **SCS pubs & preprints**

- F. Büttner, B. Pfau, M. Böttcher, et al.: "Observation of fluctuation-mediated picosecond nucleation of a topological phase", Nature Materials (2020), doi:10.1038/s41563-020-00807-1

- D. Turenne, A. Yaroslavtsev, X. Wang, et al.: "Nonequilibrium sub 10 nm spin-wave soliton formation in FePt nanoparticles", Science Advances 8, eabn0523 (2022), doi:10.1126/sciadv.abn0523

- R. Khubbutdinov, N. Gerasimova, G. Mercurio, et al.: "High spatial coherence and short pulse duration revealed by the Hanbury Brown and Twiss interferometry at the European XFEL", Structural Dynamics 8, 044305 (2021), doi:10.1063/4.0000127

- G. Mercurio, J. Chalupskỳ, I.-T. Nistea, et al.: "Real-time spatial characterization of micrometer-sized X-ray free-electron laser beams focused by bendable mirrors", Opt. Express 30, 20980–20998 (2022) doi:10.1364/OE.455948

- N. Agarwal: "Ultrafast dynamics of electronic structure and domain nucleation during photo-induced phase transition in FeRh", dissertation (University of Hamburg 2021)

- N. Gerasimova, D. L. Civita, L. Samoylova, et al.: "Monochromatic operation of the SASE3 soft X-ray beamline at European XFEL" (2022), submitted, arXiv: 2206.08729

- N. Hagström, M. Schneider, N. Kerber, et al.: "Megahertz-rate Ultrafast X-ray Scattering and Holographic Imaging at the European XFEL", accepted to Journal of Synchrotron Radiation, arXiv: arXiv:2201.06350

- N. Thielemann-Kühn, T. Amrhein, W. Bronsch, et al.: "Optical control of 4f orbital state in rare-earth metals", submitted, arXiv: 2106.09999

- N. Hagström, R. Jangid, M. Madhavi, et al.: "Symmetry-dependent ultrafast manipulation of nanoscale magnetic domains", submitted, arXiv: 2112.09587

Table 5.1: List of proposals, PIs, techniques employed and present outcome. Acronyms: UP stands for User Proposal, IHR stands for In-House Research, UAC stands for User.Assisted Commissioning.

Semester	Proposal - PI	technique	outcome
2018-II	UP2170 - Beye	non-linear XAS	manuscript drafted
	UP2197 - Pfau	non-linear SAXS	data analysis
2019-I	UP2222 - Bonetti	holography	accepted
	UP2252 - Büttner	SAXS	published
	UP2212 - Jal	SAXS	accepted
	UP2280 - Dürr	SAXS	manuscript in preparation
	UP2313 - Pronin	SAXS	manuscript drafted
2019-II	UP2384 - Thielemann	XAS	submitted
	IHR2557 - Vartanyants	HBT	published
	IHR2565 - Scherz	SAXS	manuscript in preparation
	UP2161 - Eschenlohr	XAS	manuscript in preparation
	UP2225 - Carley	SAXS	PhD thesis
2020-I	UP2511 - Staub	reflectivity	manuscript drafted
	UP2530 - Bonetti	holography	accepted
	UP2589 - Eschenlohr	XAS	manuscript in preparation
2020-II	IHR2712 - Scherz	XAS	manuscript in preparation
	UP2599 - Dürr	SAXS	published
	UP2471 - Silva	SAXS	submitted
	UP2619 - Le Guyader	XAS	data analysis
	UP2858 - Büttner	holography	data analysis
	UP2780 - Ovchinikov	XAS	data analysis
2021-II	UP2593 - Mercadier	non-linear XAS	manuscript in preparation
	UP2497 - Cho	XAS	data analysis
	UP2609 - Menushenkov	XAS	data analysis
	UP2784 - van Kuiken	XAS	data analysis

Table 5.3: List of proposals, PIs, techniques employed and present outcome. Acronyms: UP stands for User Proposal, IHR stands for In-House Research, UAC stands for User.Assisted Commissioning.

Semester	Proposal - PI	technique	outcome
	UAC2769 - Schlappa	RIXS	data analysis
	UAC2776 - van Kuiken	RIXS	data analysis
	UAC2866 - van Kuiken	RIXS	data analysis
2022-I	UP2783 - Wende	XAS	data analysis
	UP2800 - Gruebel	SAXS	data analysis
	UP3216 - Cho	XAS	data analysis
	UP2884 - Turner	XPCS	data analysis

6   Conclusion and Outlook

Achievements

- Nearly the entire set of planned instrumentation is commissioned and operational at SCS. The final piece - the XRD endstation will be commissioned later this year.
- Together with the Detector Group and the User Consortium we have commissioned the MHz-capable DSSC detector at the SCS Instrument. With that we are able to make full use of the high repetition rate of the European XFEL.
- Along with the hRIXS UC, SCS has developed and commissioned a unique instrument for high-resolution RIXS experiments at XFELs.
- SCS have performed numerous successful user experiments using a variety of time-resolved x-ray spectroscopic techniques and employing a wide range of excitation wavelengths.
- With contributions from the Data Group and user groups SCS have developed a python toolbox that allows users to rapidly analyse their data. It is maintained in a Git repository as a central resource, which facilitates consistent, reproducible data evaluation.

Next steps / short-term improvements

- Work is underway to extend the available pump laser wavelengths into the far-IR and THz.
- The helical afterburner is of critical importance to the magnetism community. It will significantly extend the power of XAS and XMCD, as well as SAXS, CDI.
- Further work is urgently needed to improve automation and stable operation of the SCS Instrument. The objective is user-friendly high level controls for regular tasks and monitors to mitigate beam drift from SASE1/SASE3 interference.
- The current mode of fully supported user operation between 7-23 is certainly an improvement over 12 hour shifts per instrument because it allows uninterrupted 24 hour operation. It would be further improved if full support was provided throughout the night.
- A remaining challenge is how to more efficiently use the beam and increase the number of proposals. The existing six days of beamtime is typically too long for one proposal, but too short for two. Other cycles should be discussed and tested.
- Given the need to quickly exchange endstations during operation periods, each endstation should, as far as possible, remain fully equipped with its controls,

laser optics, and external diagnostics when removed from the beam line. To this end the CHEM and XRD endstations have local Beckhoff controls. This approach should be extended to all endstations and include other periferals such as cameras, microscopes, ethernet switches, as required.

Mid-term developments to extend capabilities

- A non-trivial but essential addition to SCS will be a non-invasive pulse arrival monitor to reduce further the timing jitter between trains and to reduce long term drifts.
- On the optical laser side, the use of liquid jets has highlighted the need for higher pulse energies in the UV. These will need to run at high-repetition rate to increase data efficiency at MHz repetition rates.
- We will continue to work to bring CDI to its full potential. The helical afterburners will certainly play an important role here, but other approaches, for example the use of machine learning for data classification in image reconstruction may also play a role.
- We foresee constant development of the sample delivery systems in terms of liquid jet technology and cryogenic conditions, as well as magnetic fields.
- There is a clear conflict in the accelerator electron energy needs of the hard and soft x-ray instruments. An equitable solution needs to be found to serve all instruments independent of accelerator operation mode.

Long-term vision

- It is clear that the number of x-ray spectroscopic techniques possible at SCS, and the different instrumentation it requires form a bottleneck in terms of scheduling that requires, ideally, dedicated beamlines to make more efficient use of the beam.

7   Bibliography

[1] N. Agarwal: "Ultrafast dynamics of electronic structure and domain nucleation during photo-induced phase transition in FeRh", dissertation (University of Hamburg 2021)

[2] R. Arpaia, S. Caprara, R. Fumagalli, et al.: "Dynamical charge density fluctuations pervading the phase diagram of a Cu-based high-T c superconductor", Science **365**, 906–910 (2019)

[3] I. Ascone, R. Strange: "Biological X-ray absorption spectroscopy and metalloproteomics", Journal of Synchrotron Radiation **16**, 413–421 (2009) doi:10.1107/s0909049509010425

[4] N. Awari, A. Semisalova, J. C. Deinert, et al.: "Monitoring laser-induced magnetization in FeRh by transient terahertz emission spectroscopy", Applied Physics Letters **117** (2020) doi:10.1063/5.0019663

[5] J. Bertinshaw, M. Krautloher, H. Suzuki, et al.: "Spin and charge excitations in the correlated multiband metal $Ca_3Ru_2O_7$", Phys. Rev. B **103**, 085108 (2021) doi:10.1103/PhysRevB.103.085108

[6] J. Bertinshaw, S. Mayer, F.-U. Dill, et al.: "IRIXS Spectrograph: an ultra high-resolution spectrometer for tender RIXS", Journal of Synchrotron Radiation **28**, 1184–1192 (2021) doi:10.1107/S1600577521003805

[7] D. Betto, R. Fumagalli, L. Martinelli, et al.: "Multiple-magnon excitations shape the spin spectrum of cuprate parent compounds", Phys. Rev. B **103**, L140409 (2021) doi:10.1103/PhysRevB.103.L140409

[8] M. R. Bionta, N. Hartmann, M. Weaver, et al.: "Spectral encoding method for measuring the relative arrival time between x-ray/optical pulses", Review of Scientific Instruments **85** (2014) doi:10.1063/1.4893657

[9] L. Braicovich, J. van den Brink, V. Bisogni, et al.: "Magnetic Excitations and Phase Separation in the Underdoped $La_{2-x}Sr_xCuO_4$ Superconductor Measured by Resonant Inelastic X-Ray Scattering", Phys. Rev. Lett. **104**, 077002 (2010) doi:10.1103/PhysRevLett.104.077002

[10] F. Büttner, B. Pfau, M. Böttcher, et al.: "Observation of fluctuation-mediated picosecond nucleation of a topological phase", Nature Materials (2020) doi:10.1038/s41563-020-00807-1

[11] R. N. Coffee, J. P. Cryan, J. Duris, et al.: "Development of ultrafast capabilities for X-ray free-electron lasers at the linac coherent light source", Philosophical Transactions of the Royal Society A: Mathematical, Physical and Engineering Sciences **377** (2019) doi:10.1098/rsta.2018.0386

[12] L. Condat, D. V. D. Ville, B. Forster-Heinlein: "Reversible, Fast, and High-Quality Grid Conversions", IEEE Transactions on Image Processing **17**, 679–693 (2008) doi:10.1109/TIP.2008.919361

[13] M. Dommach, M. Di Felice, B. Dickert, et al.: "The photon beamline vacuum system of the European XFEL", Journal of Synchrotron Radiation **28**, 1229–1236 (2021) doi:10.1107/S1600577521005154

[14] M. Ekimova, W. Quevedo, M. Faubel, et al.: "A liquid flatjet system for solution phase soft-x-ray spectroscopy", Structural Dynamics **2**, 054301 (2015) doi:10.1063/1.4928715 eprint: https://doi.org/10.1063/1.4928715

[15] R. Y. Engel, M. Ekimova, P. S. Miedema, et al.: "Shot noise limited soft x-ray absorption spectroscopy in solution at a SASE-FEL using a transmission grating beam splitter", Structural Dynamics **8**, 014303 (2021) doi:10.1063/4.0000049

[16] European XFEL: *Data analysis at European XFEL*, 2022 https://rtd.xfel.eu/docs/data-analysis-user-documentation/en/latest/index.html (visited on August 18, 2022)

[17] European XFEL: *EXtra-data*, 2022 https://extra-data.readthedocs.io/en/latest/ (visited on August 18, 2022)

[18] European XFEL: *EXtra-foam*, 2022 https://extra-foam.readthedocs.io/ (visited on August 18, 2022)

[19] European XFEL: *EXtra-geom*, 2022 https://extra-geom.readthedocs.io/en/latest/ (visited on August 18, 2022)

[20] H. Fangohr, M. Beg, M. Bergemann, et al.: "Data Exploration and Analysis with Jupyter Notebooks", Proceedings of the 17th International Conference on Accelerator and Large Experimental Physics Control Systems **ICALEPCS2019**, USA (2020) doi:10.18429/JACOW-ICALEPCS2019-TUCPR02

[21] M. Fondell, S. Eckert, R. M. Jay, et al.: "Time-resolved soft X-ray absorption spectroscopy in transmission mode on liquids at MHz repetition rates", Structural Dynamics **4**, 054902 (2017) doi:10.1063/1.4993755 eprint: https://doi.org/10.1063/1.4993755

[22] U. Frühling, M. Wieland, M. Gensch, et al.: "Single-shot terahertz-field-driven X-ray streak camera", Nature Photonics **3**, 523–528 (2009) doi:10.1038/nphoton.2009.160

[23] C. Gahl, A. Azima, M. Beye, et al.: "A femtosecond X-ray/optical cross-correlator", Nat. Photonics **2**, 165–169 (2008) doi:10.1038/nphoton.2007.298

[24] G. Galinis, J. Strucka, J. C. T. Barnard, et al.: "Micrometer-thickness liquid sheet jets flowing in vacuum", Review of Scientific Instruments **88**, 083117 (2017) doi:10.1063/1.4990130 eprint: https://doi.org/10.1063/1.4990130

[25] N. Gerasimova, D. L. Civita, L. Samoylova, et al.: "Monochromatic operation of the SASE3 soft X-ray beamline at European XFEL" (2022)

[26] H. Gretarsson, H. Suzuki, H. Kim, et al.: "Observation of spin-orbit excitations and Hund's multiplets in Ca_2RuO_4", Phys. Rev. B **100**, 045123 (2019) doi:10.1103/PhysRevB.100.045123

[27] H. Gretarsson, D. Ketenoglu, M. Harder, et al.: "IRIXS: a resonant inelastic X-ray scattering instrument dedicated to X-rays in the intermediate energy range", Journal of Synchrotron Radiation **27**, 538–544 (2020) doi:10.1107/S1600577519017119

[28] J. Grünert, M. P. Carbonell, F. Dietrich, et al.: "X-ray photon diagnostics at the European XFEL", J. Synchrotron Rad. **26**, 1422–1431 (2019) doi:https://doi.org/10.1107/S1600577519006611

[29] L. L. Guyader, A. Eschenlohr, M. Beye, et al.: "Photon shot-noise limited transient absorption soft X-ray spectroscopy at the European XFEL" (2022) arXiv: 2211.04265 [physics.ins-det]

[30] N. Z. Hagström, R. Jangid, Meera, et al.: "Symmetry-dependent ultrafast manipulation of nanoscale magnetic domains" (2021) arXiv: 2112.09587 [cond-mat.mes-hall]

[31] N. Z. Hagström, M. Schneider, N. Kerber, et al.: "Megahertz-rate Ultrafast X-ray Scattering and Holographic Imaging at the European XFEL" (2022) arXiv: 2201.06350 [cond-mat.mes-hall]

[32] R. Heider, M. S. Wagner, N. Hartmann, et al.: "Megahertz-compatible angular streaking with few-femtosecond resolution at x-ray free-electron lasers", Phys. Rev. A. Physical Review A (2019) doi:10.1103/PhysRevA.100.053420

[33] N. Huse, T. K. Kim, L. Jamula, et al.: "Photo-Induced Spin-State Conversion in Solvated Transition Metal Complexes Probed via Time-Resolved Soft X-ray Spectroscopy", Journal of the American Chemical Society **132**, 6809–6816 (2010) doi:10.1021/ja101381a eprint: https://doi.org/10.1021/ja101381a

[34] I. Ilyakov, N. Agarwal, J.-C. Deinert, et al.: "Terahertz-wave decoding of femtosecond extreme-ultraviolet light pulses", Optica **9**, 545 (2022) doi:10.1364/OPTICA.453130

[35] R. Ivanov, I. J. B. Maclas, J. Liu, et al.: "Single-shot temporal characterization of XUV pulses with duration from 10 fs to 350 fs at FLASH", Journal of Physics B: Atomic, Molecular and Optical Physics **53** (2020) doi:10.1088/1361-6455/ab9c38

[36] J. Jensen, A. Mackintosh: *Rare earth magnetism: Structures and excitations* (Oxford University Press, United Kingdom 1991)

[37] V. Kimberg, A. Sanchez-Gonzalez, L. Mercadier, et al.: "Stimulated X-ray Raman scattering – a critical assessment of the building block of nonlinear X-ray spectroscopy", Faraday Discuss. **194**, 305–324 (2016) doi:10.1039/C6FD00103C

[38] J. Knoška, L. Adriano, S. Awel, et al.: "Ultracompact 3D microfluidics for time-resolved structural biology", Nature Communications **11**, 657 (2020) doi:10.1038/s41467-020-14434-6

[39] J. D. Koralek, J. B. Kim, P. Brůža, et al.: "Generation and characterization of ultrathin free-flowing liquid sheets", Nature Communications **9**, 1353 (2018) doi:10.1038/s41467-018-03696-w

[40] S. Kovalev, B. Green, T. Golz, et al.: "Probing ultra-fast processes with high dynamic range at 4th-generation light sources: Arrival time and intensity binning at unprecedented repetition rates", Structural Dynamics **4** (2017) doi:10.1063/1.4978042

[41] T. Kroll, C. Weninger, R. Alonso-Mori, et al.: "Stimulated X-Ray Emission Spectroscopy in Transition Metal Complexes", Phys. Rev. Lett. **120**, 133203 (2018) doi:10.1103/PhysRevLett.120.133203

[42] M. Kubin, J. Kern, S. Gul, et al.: "Soft x-ray absorption spectroscopy of metalloproteins and high-valent metal-complexes at room temperature using free-electron lasers", Structural Dynamics **4**, 054307 (2017) doi:10.1063/1.4986627 eprint: https://doi.org/10.1063/1.4986627

[43] C. Lian, Z. A. Ali, H. Kwon, et al.: "Indirect but Efficient: Laser-Excited Electrons Can Drive Ultrafast Polarization Switching in Ferroelectric Materials", J. Phys. Chem. Lett. **10**, 3402–3407 (2019) doi:10.1021/acs.jpclett.9b01046

[44] B. Liu, H. Bromberger, A. Cartella, et al.: "Generation of narrowband, high-intensity, carrier-envelope phase-stable pulses tunable between 4 and 18 THz", Opt. Lett. **42**, 129–131 (2017) doi:10.1364/OL.42.000129

[45] S. Liu, F. Brinker, W. Decking, et al.: "Parallel operation of SaSE1 and SaSE3 at the European XFEL", 25–28 (JACoW Publishing 2019) doi:10.18429/JACoW-FEL2019-TUA01

[46] T. Maltezopoulos, F. Dietrich, W. Freund, et al.: "Operation of X-ray gas monitors at the European XFEL", J. Synchrotron Rad. **26**, 1045–1051 (2019) doi:https://doi.org/10.1107/S1600577519003795

[47] S. Manipatruni, D. E. Nikonov, C.-C. Lin, et al.: "Scalable energy-efficient magnetoelectric spin–orbit logic", Nature **565**, 35–42 (2019) doi:10.1038/s41586-018-0770-2

[48] L. Mercadier, A. Benediktovitch, C. Weninger, et al.: "Evidence of Extreme Ultraviolet Superfluorescence in Xenon", Phys. Rev. Lett. **123**, 023201 (2019) doi:10.1103/PhysRevLett.123.023201

[49] L. Mercadier, A. Benediktovitch, Š. Krušič, et al.: "Transient Absorption of Warm Dense Matter Created by an X-Ray Free-Electron Laser" (2022) doi:10.21203/rs.3.rs-2396961/v1

[50] G. Mercurio, J. Chalupský, I.-T. Nistea, et al.: "Real-time spatial characterization of micrometer-sized X-ray free-electron laser beams focused by bendable mirrors", Opt. Express **30**, 20980–20998 (2022) doi:10.1364/OE.455948

[51] B. Nagler, U. Zastrau, R. R. Fäustlin, et al.: "Turning solid aluminium transparent by intense soft X-ray photoionization", Nature Physics **5**, 693–696 (2009) doi:10.1038/nphys1341

[52] M. Pergament, M. Kellert, K. Kruse, et al.: "High power burst-mode optical parametric amplifier with arbitrary pulse selection", Opt. Express **22**, 22202–22210 (2014) doi:10.1364/OE.22.022202

[53] M. Pergament, G. Palmer, M. Kellert, et al.: "Versatile optical laser system for experiments at the European X-ray free-electron laser facility", Opt. Express **24**, 29349–29359 (2016) doi:10.1364/OE.24.029349

[54] Philipp Schmidt: *EXtra-metro*, 2022 https://desy.de/~schmidtp/metropc-docs/ (visited on August 18, 2022)

[55] A. Pietzsch, F. Hennies, P. S. Miedema, et al.: "Snapshots of the Fluctuating Hydrogen Bond Network in Liquid Water on the Sub-Femtosecond Timescale with Vibrational Resonant Inelastic x-ray Scattering", Phys. Rev. Lett. **114**, 088302 (2015) doi:10.1103/PhysRevLett.114.088302

[56] A. Pietzsch, J. Niskanen, V. V. da Cruz, et al.: "Cuts through the manifold of molecular H_2O potential energy surfaces in liquid water at ambient conditions", Proceedings of the National Academy of Sciences **119**, e2118101119 (2022) doi:10.1073/pnas.2118101119 eprint: https://www.pnas.org/doi/pdf/10.1073/pnas.2118101119

[57] M. Porro, L. Andricek, S. Aschauer, et al.: "Development of the DEPFET Sensor With Signal Compression: A Large Format X-Ray Imager With Mega-Frame Readout Capability for the European XFEL", IEEE Transactions on Nuclear Science **59**, 3339–3351 (2012) doi:10.1109/tns.2012.2217755

[58] M. Porro, L. Andricek, S. Aschauer, et al.: "The MiniSDD-Based 1-Mpixel Camera of the DSSC Project for the European XFEL", IEEE Transactions on Nuclear Science **68**, 1334–1350 (2021) doi:10.1109/TNS.2021.3076602

[59] M. Rossi, R. Arpaia, R. Fumagalli, et al.: "Experimental determination of momentum-resolved electron-phonon coupling", Physical review letters **123**, 027001 (2019)

[60] T. Sato, R. Letrun, H. J. Kirkwood, et al.: "Femtosecond timing synchronization at megahertz repetition rates for an x-ray free-electron laser", Optica **7**, 716 (2020) doi:10.1364/optica.396728

[61] E. Savelyev, R. Boll, C. Bomme, et al.: "Jitter-correction for IR/UV-XUV pump-probe experiments at the FLASH free-electron laser", New J. Phys. **19**, 043009 (2017) doi:10.1088/1367-2630/aa652d

[62] W. F. Schlotter, M. Beye, S. Zohar, et al.: "Balanced Detection in Femtosecond X-ray Absorption Spectroscopy to Reach the Ultimate Sensitivity Limit" (2020) arXiv: 2006.13968v1 [physics.ins-det]

[63]   M. Schneider, C. M. Günther, B. Pfau, et al.: "In situ single-shot diffractive fluence mapping for X-ray free-electron laser pulses", Nature Communications **9**, 214 (2018) doi:10.1038/s41467-017-02567-0

[64]   M. Schneider, C. M. Günther, B. Pfau, et al.: "In situ single-shot diffractive fluence mapping for X-ray free-electron laser pulses", Nature Communications **9** (2018) doi:10.1038/s41467-017-02567-0

[65]   M. Schneider, C. M. Günther, C. von Korff Schmising, et al.: "Curved gratings as an integrated photon fluence monitor in x-ray transmission scattering experiments", Optics Express **24**, 13091 (2016) doi:10.1364/OE.24.013091

[66]   SCS team: *SCS Toolbox documentation*, 2022 https://rtd.xfel.eu/docs/scs-toolbox/en/latest/index.html (visited on June 21, 2022)

[67]   T. Seifert, S. Jaiswal, U. Martens, et al.: "Efficient metallic spintronic emitters of ultrabroadband terahertz radiation", Nature Photonics **10**, 483–488 (2016) doi:10.1038/nphoton.2016.91

[68]   H. Sinn, J. Gaudin, L. Samoylova, et al.: "Conceptual Design Report: X-Ray Optics and Beam Transport", en (2011), p. 132 doi:10.3204/XFEL.EU/TR-2011-002

[69]   A. A. Sorokin, Y. Bican, S. Bonfigt, et al.: "An X-ray gas monitor for free-electron lasers", J. Synchrotron Rad. **26**, 1092–1100 (2019) doi:https://doi.org/10.1107/S1600577519005174

[70]   N. A. Spaldin: "Multiferroics beyond electric-field control of magnetism", Proc. R. Soc. A. **476**, 20190542 (2020) doi:10.1098/rspa.2019.0542

[71]   H. Suzuki, H. Gretarsson, H. Ishikawa, et al.: "Spin waves and spin-state transitions in a ruthenate high-temperature antiferromagnet", Nature Materials **18**, 563–567 (2019) doi:10.1038/s41563-019-0327-2

[72]   H. Suzuki, H. Liu, J. Bertinshaw, et al.: "Proximate ferromagnetic state in the Kitaev model material α-RuCl3", Nature Communications **12**, 4512 (2021) doi:10.1038/s41467-021-24722-4

[73]   N. Thielemann-Kühn, T. Amrhein, W. Bronsch, et al.: "Optical control of 4f orbital state in rare-earth metals" (2021) arXiv: 2106.09999 [cond-mat.mtrl-sci]

[74]   D. Turenne, A. Yaroslavtsev, X. Wang, et al.: "Nonequilibrium sub 10 nm spin-wave soliton formation in FePt nanoparticles", Science Advances **8**, eabn0523 (2022) doi:10.1126/sciadv.abn0523 eprint: https://www.science.org/doi/pdf/10.1126/sciadv.abn0523

[75]   I. A. Vartanyants, M. V. Kovalchuk: "Theory and applications of x-ray standing waves in real crystals", Rep. Prog. Phys. **64**, 1009–1084 (2001) doi:10.1088/0034-4885/64/9/201

[76]   C. Weninger, M. Purvis, D. Ryan, et al.: "Stimulated Electronic X-Ray Raman Scattering", Phys. Rev. Lett. **111**, 233902 (2013) doi:10.1103/PhysRevLett.111.233902

[77] B. Wu, T. Wang, C. E. Graves, et al.: "Elimination of X-Ray Diffraction through Stimulated X-Ray Transmission", Phys. Rev. Lett. **117**, 027401 (2016) doi:10.1103/PhysRevLett.117.027401

[78] J. Zegenhagen: "Surface structure determination with X-ray standing waves", Surface Science Reports **18**, 202–271 (1993) doi:10.1016/0167-5729(93)90025-K

[79] Y. Zhang, Y. Zhang, Q. Guo, et al.: "Characterization of domain distributions by second harmonic generation in ferroelectrics", npj Comput Mater **4**, 39 (2018) doi:10.1038/s41524-018-0095-6

[80] D. Zhu, M. Guizar-Sicairos, B. Wu, et al.: "High-resolution X-ray lensless imaging by differential holographic encoding", Physical Review Letters **105**, 043901 (2010) doi:10.1103/PhysRevLett.105.043901

[81] D. Zusin, E. Iacocca, L. L. Guyader, et al.: "Ultrafast perturbation of magnetic domains by optical pumping in a ferromagnetic multilayer" (2020) arXiv: 2001.11719 [cond-mat.mes-hall]

A   SCS instrument fact sheet

SCS Instrument Parameters for User Experiments – 2023-I / 9th CfP

Page 1/3, 10 June 2022 – revised. Changes highlighted

European XFEL

Photon beam parameters		
Photon energy SASE3	0.5 – 3.0 keV	
X-ray pulse energy	5 mJ (0.5 – 1.5 keV) 1.5 – 2.5 keV > 2.5 keV	expected performance. Pulse energy depends on bunch charge, electron energy and photon energy
X-ray pulse duration	10-25 fs (fwhm), short bunches (<10fs)*	*) short bunches requires coordinated scheduling as other instruments and available number of bunches might be affected; time-diagnostics only partially available.
Mono resolving power	LR grating 1st order: 3,000 (3 permille transmission) HR grating 1st order: 10,000	High resolution compromises short pulse durations, see pulse stretching
X-ray pulse stretching	30 – 50 fs (mono LR) 80 – 150 fs (mono HR)	expected durations based on monochromator
X-ray pulse energy after mono	1 – 30µJ	Mono 1st order
Number of pulses per train	350	X-ray pulses per instrument assuming equal distribution at 2.25 MHz (higher/smaller pulse numbers for higher/smaller intra-train frequencies or interleaved mode). Maximum 2250 electron bunches within 500 µs are available for distribution to the instruments (4.5 MHz).
Repetition rate in pulse train	Up to 4.5 MHz	1.1MHz for the use of liquid jet
Train repetition rate	10 Hz SCS train picker	SCS train picker to convert e.g. 5Hz, or single train
Polarization	Linear (horizontal) Circular polarizer (approx. 50% circ. Pol. and few % transmission)	Circular polarizer are available for Fe, Co and Ni L edges. They operate in vicinity of respective absorption resonances. Inquire for details and possibilities for other absorption resonances
Focal spot size at sample, tunable	1 µm (hor & ver) tunable up to 500µm	Independent tuning of horizontal and vertical focus. line focus is used for RIXS.

ENLIGHTENING SCIENCE

SCS Instrument Parameters for User Experiments – 2023-I / 9th CfP

Page 2/3, 10 June 2022 – revised. Changes highlighted

FFT experiment station - solid sample environment, Forward–scattering geometries		
Fixed target sample holder	Frame with 50 mm x 50 mm active area. limited fast "single-shot" scanning, room temperature, forward scattering geometry	
Sample Frame	Standard frames are provided by the instrument. A drawing of the frame to produce own sample frames is available on request	
DC electromagnet	≤ 0.35 T	
Cryostat sample holder	15 – 300K, top-inserted LHe flow cryostat, inquire for details	
DSSC detector	**SAXS, CDI, BOZ-XAS, XPCS**	
Number of pixels	1024 x 1024	
Pixel coordinates	Hexagonal	Detector quadrants in windmill configuration
Pixel size	204 µm x 236 µm	
Max frame rate	4.5 MHz	
Beam hole size	Default: 4.75 mm (windmill)	The diameter of the central dead area is 8mm.
Standard detector-to-sample distance	Min: 1.24 m Max: 5.40 m Travel range: 1.5 m (under vacuum)	
Femto-XAS	**XAS, BOZ-XAS**	
Transmission Monitor (cw diamond / MCP)	Pulse resolved detection, parallel operation to DSSC	operates up to 4.5 MHz, sensitivity: ten nJ
Beam-splitting off-axis zone plate (BOZ) for MHz transient XAS	BOZ exist for various photon energy ranges, for photon energies above 1.5keV inquire	BOZ X-ray Absorption Spectroscopy is recorded with DSSC. Inquire for details of the method and its possibilities.
PI-MTE3 Detector		
Number Pixels / Size	2048 x 2048, 15µm x15µm	Cartesian coordinates, 30.7 x 30.7 mm imaging area
Frame rate	up to 1Hz	4 port readout, inquire for details
detector-sample distance	55 - 820 mm	

ENLIGHTENING SCIENCE

SCS Instrument Parameters for User Experiments – 2023-I / 9th CfP

Page 3/3, 10 June 2022 – revised. Changes highlighted

European XFEL

CHEM / Liquid sample environment		
Sample delivery	Liquid jet, single cylinder, 20-50µm	Standard configuration
RIXS scattering angle	125 deg, 90 deg	Standard configuration: 125 deg
Solvents	Water, Ethanol, Isopropanol*	Standard configuration. *) Inquire for alternative solvents
hRIXS Spectrometer for CHEM / Liquid sample environment		
Photon energy range	0.5 – 1.4 keV	commissioned up to 1keV, nominal up to 1.4keV
Combined resolving power (Monochromator & hRIXS)	Up to 10,000 (High resolution) Up to 3,000 (Low resolution)	Commissioned in the range of O K edge and Cu L edge Inquire for details of spectrometer transmission.
Optical laser system	**SASE3 PP laser**	
Centre wavelength	800 nm	
Wavelength tunability	Conversions from 800 nm / 50 fs: SHG (400 nm) , THG (266 nm), OPA: wavelength between 350 nm and 2.5 microns Please inquire for details on pulse energies	
Pulse duration	Default: 35fs (800nm), 800 nm: 15 –50 fs	
Repetition rate and Pulse energy	800 nm: 0.2 - 2 mJ (1 MHz – 113 kHz)	Default: 113kHz in burst (depending on rep rate)
Operation	Burst mode synchronized to FEL with jitter <50 fs	

Please discuss your experiment plans with the SCS team as soon as possible and **before** submitting your proposal. We can help you with any details that may have updated, assist with evaluating experiment feasibility, and much more.

This call is open for

1) experiments using the forward-scattering geometries and solid sample environment of FFT, i.e. XAS/XMCD, SAXS, CDI, XPCS

2) experiments using the liquid sample environment of the CHEM station for XAS/RIXS in back-scattering geometries. (see also standard configuration CHEM-RIXS)

Contacts:
scs@xfel.eu
useroffice@xfel.eu

ENLIGHTENING SCIENCE

SCS CHEM-RIXS standard configuration – 2023-I / 9th Call for Proposals

Page 1/1, 10 June 2022 – revised. Changes highlighted

European XFEL

CHEM-RIXS Standard Configuration		
Photon energy	0.5 – 1.5 keV	
X-ray pulse energy SASE3	5 mJ	expected performance. Pulse energy depends on bunch charge, electron energy and photon energy
Repetition rate in pulse train	Up to 1.1 MHz	1.1MHz for the use of liquid jet
Combined resolving power (Mono + hRIXS Spectrometer)	up to 3,000	
X-ray pulse stretching	30 – 50 fs (mono LR)	expected durations based on monochromator
X-ray pulse energy after mono	1 – 30μJ	Mono 1st order
Number of pulses per train	350 pulses (assuming equal distribution of pulses per instrument)	1.1MHz using SASE1 / SASE3 interleaved mode
Polarization	Linear (horizontal)	
Focal spot size at sample, tunable	10-30 μm x 10 μm hor. & ver. tunable	10μm vertical is used for RIXS
Sample delivery	20 – 50 μm liquid jet, single cylinder	
Solvents	Water, Ethanol, Isopropanol	
RIXS scattering angle	125 deg	
Optical laser	800nm: 0.2mJ (1.1MHz) – 2mJ (0.113kHz), 400nm (SHG), 266nm (THG) via conversion from 800nm; spot size ~100μm; Linear, circular polarization	

Please discuss your experiment plans with the SCS team to see if it meets the criteria of CHEM-RIXS standard configuration as soon as possible and **before** submitting your proposal. Other configurations are possible, and parameters need to be stated in the proposal. We can help you with any details and assist with evaluating experiment feasibility, and much more.

Contacts:
scs@xfel.eu
useroffice@xfel.eu

ENLIGHTENING SCIENCE

European **XFEL**

FEL parameters		
Photon energy	0.5 keV – 3.0 keV	
X-ray pulse energy SASE3	5 mJ ± 20% (0.5-1.5keV) 2 mJ ± 20% (>1.5keV)	Pulse energy depends on bunch charge, electron energy and photon energy
X-ray pulse energy after mono	1 - 30µJ (Mono 1st order)	
X-ray pulse duration SASE3	10-25 fs	fwhm
X-ray pulse stretching	80-150 fs (mono HR) 30-50 fs (mono LR)	Expected durations based on monochromator
X-ray polarization	Linear horizontal (π-polarization)	linear vertical and circular polarizations may become available during 2022 but cannot be guaranteed.
Number of x-ray pulses per train	400	400 pulses delivered assuming equal distribution at 2.25 MHz operation (Higher/smaller pulse numbers for higher/smaller intra-train frequencies). Maximum 2250 electron bunches within 500 µs are available for distribution to the instruments (4.5 MHz)
Repetition rate in pulse train	Up to 4.5 MHz	1.1 MHz maximum for the use of liquid jet.
Train repetition rate	10 Hz, or SCS train picker	SCS train picker to convert e.g. 5Hz, or single train
Mono resolving power	10.000 (HR) 3.000 (LR)	High resolution compromises short pulse durations, see pulse stretching.
X-ray focal spot size at sample	5 µm (hor & ver) tunable up to 500 µm	Independent tuning of horizontal and vertical focus. For hRIXS line focus recommended
hRIXS parameters		
Photon energy hRIXS	0.5 keV – 1.4 keV*	Commissioned up to 1.0 keV, Spectrometer operates up to 1.4 keV. Please inquire for details.
Combined resolving power (Monochromator & hRIXS)	Up to 10.000*	value reached during commissioning in May at O K edge. At Cu L3 edge a value around 8.000 was obtained.

ENLIGHTENING SCIENCE

XRD / Solid sample environment		
Samples	Solid samples	Samples have to be UHV compatible
Pressure	10^{-9} mbar	
Temperature	20 K* - room temperature	Specified for 20 K, however cannot be guaranteed. Commissioning in April 2022.
Sample stage	6 degrees of motion	Translation x, y, z: +/- 5 mm Theta: > 180 deg, Chi: +/- 30 deg Azimuth: +/- 90 deg
RIXS scattering angle	65 – 145 deg*	The hRIXS spectrometer is currently commissioned for 125 deg. In case the experiment cannot be done at this scattering angle, please contact us. Changing angle require more setup time
CHEM / Liquid sample environment		
Sample delivery	Liquid jet	Single cylinder, 20-50 microns
RIXS scattering angle	125 deg, 90 deg*	Standard configuration 125 deg. Inquire for details.
Solvents	Water, Ethanol, Isopropanol*	Discuss alternative solvents with the scientists
Optical laser system	**SASE3 PP laser**	
Center wavelength	800 nm	
Pulse duration	800 nm: 15 fs or 50 fs	
Repetition rate and Pulse energy, 800 nm	113 kH 1.1 MHz	2 mJ 0.2 mJ
Wavelength tunability	Conversions from 800nm / 50 fs via SHG (400nm), THG (266nm), OPA OPA: Wavelength between 350 nm and 2.5 microns. Please inquire for pulse energies.	
Spot size	Around 100 microns	
Polarization	Linear, circular	
Operation	Burst mode synchronized to FEL with jitter <50 fs	

ENLIGHTENING SCIENCE